Permeability of water through polymer membranes and porous electrodes

by

Yang Wu

M.Sc., University of Victoria, 2016

B.Eng., Central South University, 2014

Thesis Submitted in Partial Fulfillment of the
Requirements for the Degree of
Doctor of Philosophy

in the
Department of Chemistry
Faculty of Science

SIMON FRASER UNIVERSITY

Spring 2021

Declaration of Committee

Name:	**Yang Wu**
Degree:	**Doctor of Philosophy**
Thesis title:	**Permeability of water through polymer membranes and porous electrodes**
Committee:	**Chair:** **Hua-Zhong Yu** Professor, Chemistry
	Steven Holdcroft Supervisor Professor, Chemistry
	Paul C. H. Li Committee Member Professor, Chemistry
	Gary Leach Committee Member Associate Professor, Chemistry
	Zuo-Guang Ye Examiner Professor, Chemistry
	Brant A. Peppley External Examiner Professor, Chemical Engineering Queen's University

Abstract

Water sorption and transport through hydrocarbon (HC)-based polymer electrolyte membranes (PEMs) and porous electrodes are vital for water management and performance improvements of fuel cells. This thesis is the culmination of three research projects conducted into an extensive water sorption and transport study, including steady-state permeation, transient diffusion, and sorption isotherm on a series of novel HC-based PEMs. Numerical models, such as the Park model for sorption isotherm and the resistance model for steady-state permeation, were chosen and applied to interpret the membranes' chemical and structural features. Conductive atomic force microscope (AFM) and surface roughness measurement were applied to examine the membranes' physical properties. Collectively, transport measurements, numerical models, and characterizations were integrated to generate an insightful structure-transport correlation. The first project studies sulfonated phenylated poly(phenylene) biphenyl (SPPB) and compares it to a HC-based reference, sulfonated phenylated poly(arylene ether), and the commercial benchmark, Nafion. At thickness > ~30 μm, SPPB is the most permeable due to its lowest internal resistance coefficient. The second research involves four structurally controlled, one-element-variant, pyridyl-bearing sulfonated phenylated polyphenylenes. An increase in the number of pyridyl groups increases the fraction of neutralized protons in $–SO_3H$ groups, and decreases polymer's ion exchange capacity, proton conductivity, liquid and vaporous water sorption, dimensional swelling, steady-state water permeability, and transient diffusivity. The third investigation expands the research focus to the catalyst layers incorporated with the novel HC-based ionomers. A lower ionomer content of SPPB in the catalyst layer favors a larger water vapor uptake and faster transient diffusion rate. Specifically, the catalyst layer of 15 wt% ionomer SPPB is found possessing the best electrochemical performance with the most hydrophilic and the roughest surface. Insights obtained in this thesis can direct further tuning of the HC-based polymer's structure for desirable mass transport through both the membrane and the catalyst layers, which subsequently lead to electrochemical performance improvements of the fuel cell.

Keywords: hydrocarbon-based polymer; steady-state permeation; transient diffusion; catalyst layer; vapor sorption isotherm; fuel cells, electrolysers

Dedication

To my family, for their unconditional love and support. Especially to my dad, for everything he does for the family and being a role model of endurance.

Acknowledgments

Firstly, this thesis work would not be possible without the support and guidance from my senior supervisor, Prof. Steven Holdcroft. Also, I am grateful to my supervisory committee, Prof. Paul C. H. Li and Prof. Gary Leach, for their supervision of this thesis project. I would like to thank my internal and external examiners, Prof. Zuo-Guang Ye and Prof. Brant Peppley for their valuable time and suggestions.

I would like to thank Dr. Hsu-Feng Lee, Dr. Michael Adamski, and Dr. Shaoyi Xu for providing hydrocarbon-based polymers. Thank Mr. Emmanuel Balogun for undertaking catalyst layer preparation and carrying out fuel cell analysis. Thank Dr. Xiaoyan Luo for her guidance in my first year.

The following are acknowledged in no particular order.

Jonathan Ward, Wei Li, Patrick Fortin, Thomas Holmes, and Amelia Hohenadel, for soothing my social life in my first year at SFU.

Thomas Doerksen for inspiring me to continue my enthusiasm in chemistry. Adrian Robson for his hospitality, making my years in Canada an incredible journey.

Peter for his rides, trips, and free meals and drinks throughout the last four years, ups and downs, in Vancouver. Jared for his accompany, countless beer, and good restaurant hunts during the hard times. Ruolan and Xiaotong for their patience and listening, no matter late it is. Jane (Haoxuan) for working on my presentation and many other work suggestions.

Thanks Chu, Peter, Kathlyn, and many others for their kindness proofreading my thesis.

Table of Contents

List of Tables

List of Figures

List of Acronyms

AC	Alternating current
AFCs	Alkaline fuel cells
AFM	Atomic force microscope
BET	Brunauer-Emmett- Teller
BPBPy	Biphenylated bipyridyl
CAD	Canadian dollar
CCM	Catalyst coated membrane
CL	Catalyst layer
DFT	Density function theory
DS	Dimensional swelling
DVS	Dynamic vapor sorption
ECSA	Electrochemical surface area
EW	Equivalent weight
FH	Flory-Huggins
FTIR-ATR	Fourier transform infrared-attenuated total reflectance
GDL	Gas diffusion layer
GE	General Electric
HC	Hydrocarbon
HOR	Hydrogen oxidation reaction
IEC	Ion exchange capacity
LLP	Liquid-liquid permeation
LVP	Liquid-vapor permeation
MCFCs	Molten carbonate fuel cells

MEA	Membrane electrode assembly
NASA	National Aeronautics and Space Administration
NMR	nuclear magnetic resonance
NSERC	National Sciences and Engineering Research Council
OCV	Open circuit voltage
ORR	Oxygen reduction reaction
PAFCs	Phosphoric acid fuel cells
PE	Polyethylene
PEI	Proton exchange ionomer
PEM	Proton exchange membrane / Polymer electrolyte membrane
PEMFC	Proton exchange membrane fuel cell
PFSA	Perfluorosulfonic acid
PGSE	pulsed-field gradient spin-echo
PTFE	Poly(tetrafluoroethylene)
PTPy	Phenylated tripridyl
QENS	quasi-elastic neutron scattering
RD&D	Research, development and demonstration
RH	Relative humidity
SANS	small-angle neutron scattering
SAXS	Small-angle X-ray scattering
sBPBPyPP	Sulfonated biphenylated bipyridyl polyphenylenes
slpm	standard liters per minute
SOFCs	Solid oxide fuel cells
SPAE	Sulfonated poly(arylene ether)
sPEEK	sulfonated poly(ether ether ketone)

sPP	Sulfonated phenylated polyphenylenes
SPPB	Sulfonated phenylated poly(phenylene) biphenyl
sPTPyPP	Sulfonated phenylated tripridyl polyphenylenes
SS	Steady-state
sTPPPP	Sulfonated triphenylated phenyl polyphenylenes
sTPPyPP	Sulfonated triphenylated pyridyl polyphenylenes
sTPyPP	Sulfonated tetrapyridyl polyphenylenes
TPP	Triphenylated phenyl
TPPy	Triphenylated pyridyl
TPy	Tetrapyridyl
USD	United States dollar
WS	Water sorption
WU	Water uptake

List of Symbols

σ	Ionic conductivity
(1+0)N-H^+	Sulfonated triphenylated pyridyl polyphenylenes
(1+1)N-H^+	Sulfonated biphenylated bipyridyl polyphenylenes
(3+0)N-H^+	Sulfonated phenylated tripridyl polyphenylenes
(3+1)N-H^+	Sulfonated tetrapyridyl polyphenylenes
X_V	Water volume fraction
$\Delta\mu_w$	Chemical potential difference/gradient
A_{Pt}	Effective electrochemical surface area in 0-D equation
J_w	Molar water flux
K_A	Aggregation equilibrium constant in Park model
K_H	Henry' law coefficient in Park model
K_L	Affinity constant in Park model
L_{Pt}	Platinum loading in 0-D equation
M_0	Initial mass
M_∞	Final or equilibrated mass
M_t	Instantaneous mass
R^{dc}	Internal ionic resistance in 0-D equation
a_L	Specific site capacity in Park model
j_0	Catalyst area-normalized exchange current density
k_{sorp}	Effective rate constant of diffusion
p_{H_2O}	Partial pressure of water vapor
p_{sat}	Water saturation pressure
γ_{liq}	Temperature coefficients for the chemical potential of liquid water

γ_{vap}	Temperature coefficients for the chemical potential of water vapor
μ'	Effective proton mobility
$\mu^{\circ}{}_{liq\_STD}$	Standard chemical potentials of liquid water
$\mu^{\circ}{}_{vap\_STD}$	Standard chemical potentials of water vapor
$[-SO_3H]$	Acid concentration
μm	Micrometer
0N-H^+	Sulfonated triphenylated phenyl polyphenylenes
A	Visco-elastic coefficient in Weibull model
F	Faraday's constant
N211	Nafion® 211
pKa	Acid dissociation constant
R_q	Mean square roughness
λ	Hydration number
μg	Microgram
ρ	Density
D	Transient diffusivity
L	Membrane wet thickness
P	Water permeability
R	Water permeation resistance
a	Water activity
b	Tafel slope in 0-D equation
n	Aggregate number in Park model
p	Water permeance
r	Internal resistance coefficient

δ	Pressure coefficient of chemical potential of liquid water
τ	Characteristic time constant in transient diffusion

Chapter 1. Introduction

Human activities generate some 50 gigatons of carbon dioxide annually.[1] Much of the emitted carbon dioxide results from the use of fossil fuels, which currently satisfy over 85% of global energy demand.[2] As a result of this dependency, current models predict an average temperature increase of 3.3-3.9 °C by the end of the century [3], and the depletion of fossil fuel reserves in two centuries.[1,4] In response to these challenges, Mission Innovation, an international initiative founded in 2015, is working on expediting clean energy development.[5] From 2014-15 to 2019-20, Canadian federal departments, organizations, and agencies have doubled annual clean energy research, development and demonstration (RD&D) investments from 387 million Canadian dollars (CAD) to 775 million CAD.[6] Within this economic, political, and social context, interest in using fuel cells, especially the proton exchange membrane fuel cells (PEMFC), as clean energy conversion devices has been rapidly increasing.

1.1. Proton exchange membrane fuel cell (PEMFC)

1.1.1. Fuel cell

The hydrogen economy best represents green fuel production and application with the participation of hydrogen gas instead of fossil fuel. Two electrochemical technologies are founded on the idea of the hydrogen economy, the water electrolyzer and the fuel cell. The water electrolyzer converts electrical energy into chemical energy, producing hydrogen and oxygen gas from water.[7] The fuel cell yields electricity from the H_2-O_2 catalytic reaction without heat-to-work conversion, or without the reliance of bulky moving parts as the traditional internal combustion engine.[7] Compared to the internal combustion engine, fuel cells are not restricted to the Carnot principle, and are therefore capable of a theoretical fuel efficiency up to 83%.[8,9] Fuel cells are classified by their electrolytes, and include alkaline fuel cells (AFCs), solid oxide fuel cells (SOFCs), molten carbonate fuel cells (MCFCs), phosphoric acid fuel cells (PAFCs) and proton exchange membrane fuel cells (PEMFCs).[10] Among these, proton exchange membrane fuel cells have the greatest potential to power commercial vehicles due to its premier power density and relatively low operating temperature.[11]

Figure 1-1 is an exploded view of an operating proton exchange membrane fuel cell. In the center is the hydrated proton exchange membrane, which is sandwiched between two catalyst layers (CLs) and two gas diffusion layers (GDLs).[8] On the anode side, H_2 gas is introduced from the flow field plate, which is evenly distributed through the engraved channels. After transport through the gas diffusion layer, H_2 is dissociated into two protons (H^+) and two electrons (e^-) on the surface of the catalyst (platinum, Pt) in the anodic catalyst layer (Equation 1-1). Electrons and protons are transported from the anode to the cathode through the electrical circuit and proton exchange membrane, respectively. Oxygen is reduced in the cathodic catalyst layer, generating water (Equation 1-2) and completing the electrochemical reaction (see Equation 1-3). The equilibrium potential of the overall reaction is 1.23 V under standard conditions (1 atm, 298K).[8]

$H_2 \rightarrow 2H^+ + 2e^-$ [8]	anodic half-reaction	**Equation 1-1**
$2H^+ + 2e^- + \frac{1}{2}O_2 \rightarrow H_2O$ [8]	cathodic half-reaction	**Equation 1-2**
$H_2 + \frac{1}{2}O_2 \rightarrow H_2O \qquad E^0 = 1.23\ V$ [8]	overall reaction	**Equation 1-3**

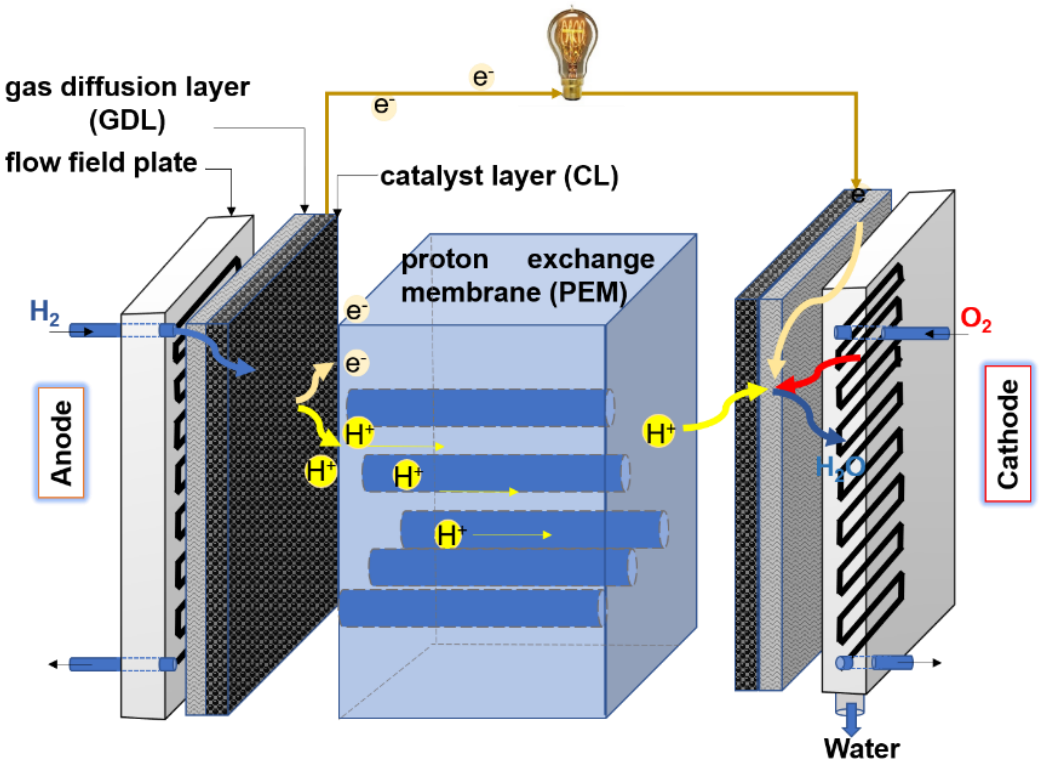

Figure 1-1. Exploded view of the proton exchange membrane fuel cell.

The application of PEMFCs in commercial automobiles is promising. To date (August 2020), PEMFCs from Ballard Power Systems, a Vancouver-based fuel cell company, have powered electric vehicles in predominately medium- and heavy-duty commercial applications. Vehicles powered by Ballard Power Systems have operated cumulatively for more than 50 million kilometers to date.[12] This is a quintuple increase from 2017 and is enough to circle the globe 1250 times.[12] However, larger-scale commercialization of PEMFC is still in its infancy and faces many obstacles.

First and foremost, the mass-production (>500,000 systems) of PEMFCs is estimated to cost about 70 USD/kW, higher than 30 USD/kW for current internal combustion engines.[13,14] 49% of PEMFC cost originates from the catalyst (21%) and the PEM (28%).[15] Expected cost improvements, from the catalyst application, involves reduction/replacement of the precious metals, and improving the catalyst's lifetime and catalytic activity.[16,17] Additional challenges for mass production and commercialization are related to the water management within PEMFCs. The presence and transport of water is crucial and affects proton conductivity, electrochemical performance, and the

durability of the fuel cell.[18] Detailed discussions on water sorption and water transport will be presented in sections 1.3 and 1.4, respectively.

1.1.2. Electrochemical interpretation: polarization curve

To evaluate the electrochemical performance of a fuel cell, the polarization curve (Figure 1-2) is ubiquitously used. The polarization curve depicts cell potential against current density. Overpotential/polarization (also known as voltage loss in electrical engineering) is the difference between the cell potential and the open-circuit voltage (OCV). Overpotential is mainly caused by 1) kinetics of the electrochemical reactions (activation overpotential); 2) internal electrical and ionic resistance (Ohmic overpotential); 3) slow mass-transport of reactants to reaction sites (mass-transport/concentration overpotential).[19]

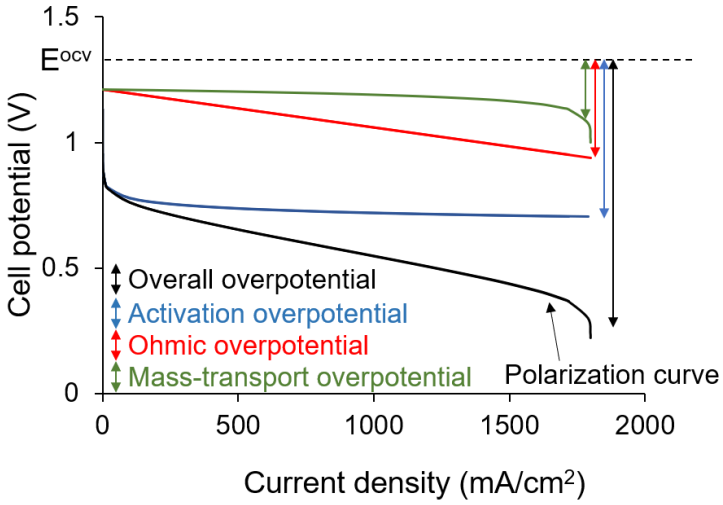

Figure 1-2. Polarization curve (black) depicts cell potential against current density. The curve is segmented into three overpotential curves: the activation overpotential (blue), the Ohmic overpotential (red), and mass-transport overpotential (green).

- Activation overpotential is predominantly due to the activation energy of both anodic and cathodic electrochemical reactions. The activation energy of the oxygen reduction reaction (ORR) at the cathode is greater than that of the hydrogen oxidation reaction (HOR), thus, creates a much larger activation overpotential at the cathode.[20] Activation overpotential is responsible for the

principal voltage loss at the low current density regime, as seen in Figure 1-2. [20]

- Ohmic overpotential is caused by the resistance to the flow of protons in the proton exchange membrane (ionic resistance) and resistance to the flow of electrons through the copper wire (electrical resistance). The electrical resistance is negligible when compared to the ionic resistance of the proton exchange membrane. Ohmic overpotential is the significant voltage loss at the medium current density regime, as shown in Figure 1-2.[21]

- Mass-transport overpotential monopolizes when reactants are rapidly consumed in the catalyst layer, and the reaction rate is limited by the mass-transport of reactants to the reaction sites. Namely, there is a concentration difference of reactants between the surface of the catalyst and gas outlet. O_2 mass-transport overpotential is dominant because of the much slower diffusion rate of O_2 than H_2. In Figure 1-2, mass-transport overpotential dominates at the large current density regime.[22]

1.2. Proton exchange membrane

The key component of the PEMFC (Figure 1-1) is the proton exchange membrane. The PEM functions as an electron insulator, proton and water conductor, and reactants separator.[23] Ideally, PEM would be mechanically robust, highly proton conductive, chemically/thermally stable, durable (> 5,000 h operating hours[24]), and low-cost.[10] In 1959, the application of a polymer electrolyte membrane in the fuel cell was first proposed by Grubb.[25] Initial attempts used hydrocarbon(HC)-based polymers and were manufactured by General Electric (GE) for the National Aeronautics and Space Administration (NASA) in the 1960s.[26] Because of chemical instability, the HC-based polymers used in initial attempts were abandoned. To fortify the chemical strength of the PEM, perfluorosulfonic acid (PFSA) ionomers were developed.[26] In 1966, DuPont invented Nafion®, a PFSA membrane that remains as state-of-the-art today as when it was introduced.[27]

1.2.1. Nafion® membrane

The general chemical structure of Nafion® is provided in Figure 1-3. The resilient poly(tetrafluoroethylene) (PTFE) backbone renders the polymer exceptional mechanical and chemical strength, and is responsible for Nafion's market dominance.[28] The tethered sidechain with the pendant ionic group results in phase separation upon solvation and subsequent ion/solvent transport capacity.[29] Understanding Nafion's phase-separated morphology is therefore critical for the study on water sorption and transport of PEMs.

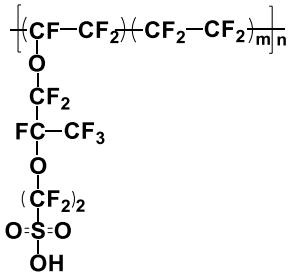

Figure 1-3. Chemical structure of Nafion®, m=6-10.

The morphology of Nafion® has been extensively studied and reviewed by Kusoglu and Weber.[29] The most commonly used techniques are small-/wide-angle scattering of X-rays and neutrons.[30–42] Gierke et al. first proposed the cluster-network model with a spherical diameter of 2 to 4 nanometers, based on water content within the membrane.[30] The cluster-network model builds on the variance of small-angle X-ray scattering (SAXS) signal with increasing hydration within Nafion®. [30] Gebel further developed this model and introduced morphological evolution,[37] which describes structural changes from spherical ionic domains to rod-like particles of the Nafion® polymer with higher hydration (Figure 1-4).[37] When the water volume fraction ($V_{water}/V_{wet\ membrane}$) is below 0.2, ionic domains remain as isolated spherical clusters.[30,36] Percolation occurs when the water volume fraction reaches over 0.2, leading the originally spherical clusters to grow and interconnect, as shown in Figure 1-4.[36,37] Beyond 0.5 water volume fraction, the presence of water dominates, and rod-like aggregates start to form in dispersion. This process is termed a structure inversion.[37] More models have since been proposed. These include the elongated rod-like model[36,42,43], the cylindrical model[39,44,45],

and the flat ribbon model.[46–49] These varying models generally agree on certain properties:

- There is ionic (hydrophilic) and perfluorinated (hydrophobic) phase separation.
- Ionic domains develop and start to interconnect (percolate) with further hydration.
- The presence of ionic/hydrophilic domains facilitates water and proton transport.

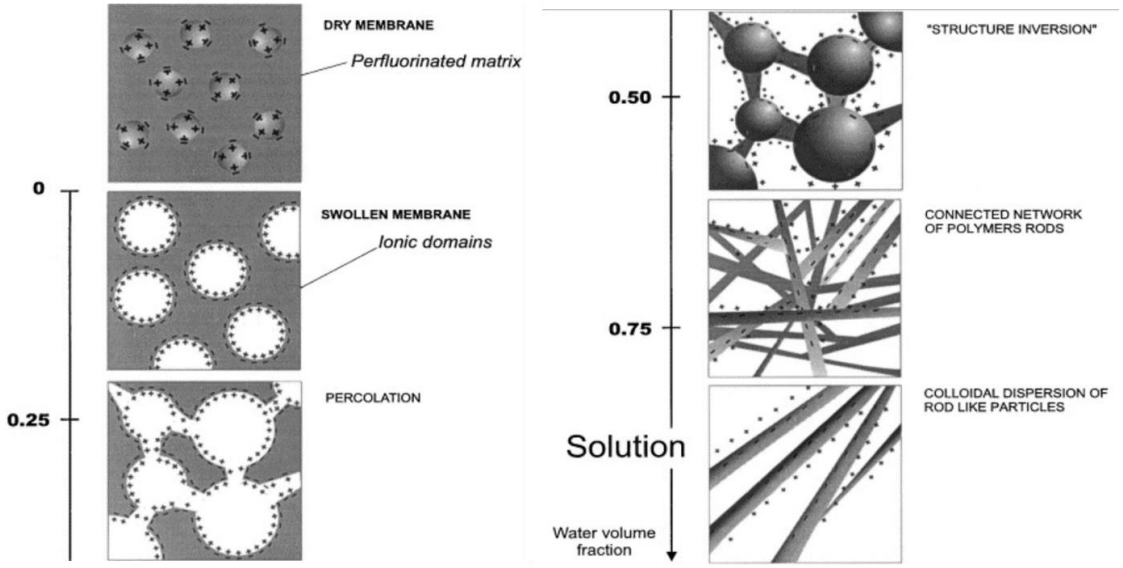

Figure 1-4. Morphological evolution of the perfluorosulfonic acid membrane with increasing water volume fraction.[37] Copyright (2000) with permission from Elsevier.

1.2.2. Novel proton exchange membranes

Despite the market dominance of Nafion®, the drawbacks of Nafion® as a perfluorosulfonic acid membrane do not go unnoticed. First and foremost is its prohibitive synthetic procedure cost.[7] Secondly, the presence of a perfluorinated backbone raises growing environmental concerns and complicates the recycling of catalysts.[50,51] High gas crossover of Nafion® decreases the yield efficiency and facilitates membrane degradation.[52,53] Therefore, there is demand for alternative PEMs, especially those that are fluorine-free and hydrocarbon-based.[50,54,55] Hydrocarbon-based polymers are

more versatile to functionalize with multiple developed synthesis pathways and are comparatively more proton-conductive than their perfluorosulfonic counterparts.[56] Structurally, HC-based PEMs are significantly different from Nafion®. In HC-based PEMs, ionic groups are directly affixed to the backbone, causing less phase separation.[31] Thermodynamically, the sulfonic acid group within HC-based ionomers is less acidic than that of the PFSA. The *pKa* of acid groups in hydrocarbon-based ionomers is -1/-2, less acidic than their counterpart in PFSAs, which is -6.[57] Both structural and thermodynamical attributes cause a higher water uptake and proton conductivity in HC-based PEMs.

Polyaromatic backbones, entirely comprised of sp^2 atoms, are thermochemically resilient and are an attractive option for incorporation in the HC-based PEMs.[31] Typical polyaromatic backbones investigated for HC-based PEMs include sulfonated poly(aryl ether sulfone)s,[58,59] sulfonated poly(benzimidazole)s,[60] sulfonated poly(phenylene)s,[61–64]and sulfonated poly(arylene ether ketone)s [65,66]. The application of these hydrocarbon-based polymers as proton exchange membranes have been reviewed extensively.[53,67,68] Representative polyaromatic backbones for proton exchange membranes are shown in Figure 1-5. The ionic, hydrophilic moieties in the PEMs are bestowed by the sulfonic acid groups introduced via either post-functionalization of the polymers' backbone, or by pre-functionalization of the monomer before polymerization. Sulfonic acid groups are employed because of their stability and high acidity.[31] The acid content governs the water sorption of the membrane—the greater content of sulfonic acid groups in the polymer, the greater the water sorption upon hydration. Unfortunately, hydrocarbon-based PEMs typically suffer from excessive swelling, given their high acid content. The other common deficiency of hydrocarbon-based PEMs is the chemical susceptibility to attacks by hydroxyl and hydroperoxyl radicals.[69] The radical attacks cause oxidative degradation and decrease life span of the membrane.[69] Electron rich heteroatoms (e.g., ether linkage) in the polymer backbone tend to increase the neighboring aromatic ring's electron density and reactivity to oxidative radicals.[70–72] Sulfonated phenylated poly(phenylene) (SPPP) comprises of a wholly aromatic backbone and displays exceptionally chemical stability (Figure 1-5).[73,74] Therefore, sulfonated phenylated poly(phenylene) has received particular attention as a potential future-generation PEM.

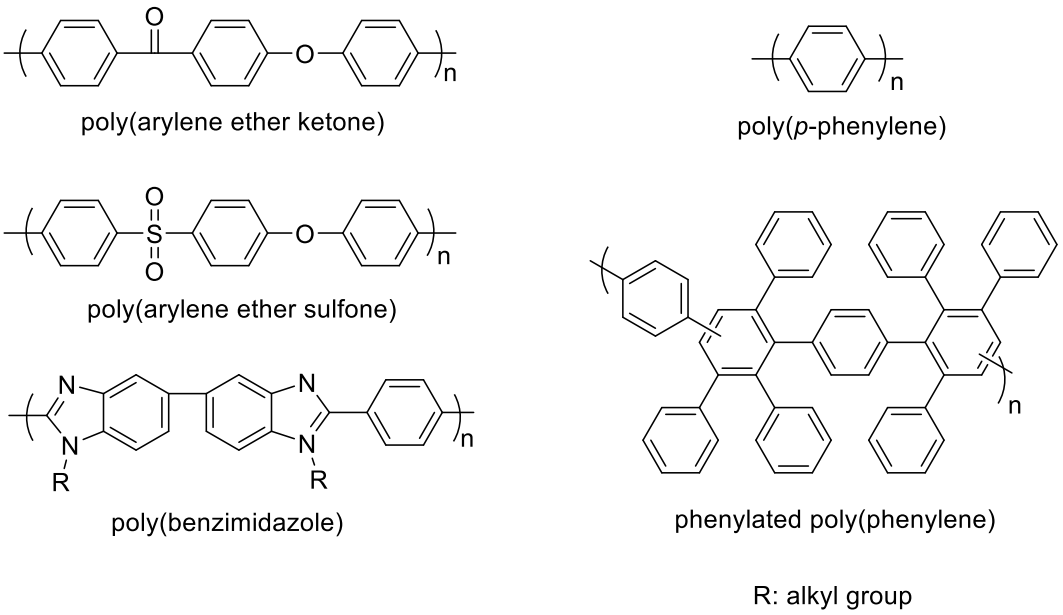

Figure 1-5. Typical polyaromatic backbones investigated for hydrocarbon-based proton exchange membranes.

Early developments of sulfonated phenylated poly(phenylene)s were restricted by limitations from the randomized post-functionalization, such as lack of repeatability, unknown placement of sulfonic acid groups on the polymer, and non-integer degrees of sulfonation per repeat unit.[54,75] In 2015, a precisely functionalized SPPP was synthesized by Skalski et al. via pre-functionalization as shown in Figure 1-6.[64] There are exactly four acidic moieties per repeat unit and their location was precisely assigned for the first time (Figure 1-6).[64] Membranes prepared from this SPPP polymer swell excessively at elevated temperature (80 °C), which downgrades their physical integrity and dimensional stability. Even though the excessive swelling issue limits the SPPP's application in fuel cells, this pre-functionalized SPPP provided a proof-of-concept for future modification in a precise molecular level to tackle with oxidative degradation and excessive swelling in hydrocarbon-based PEMs.

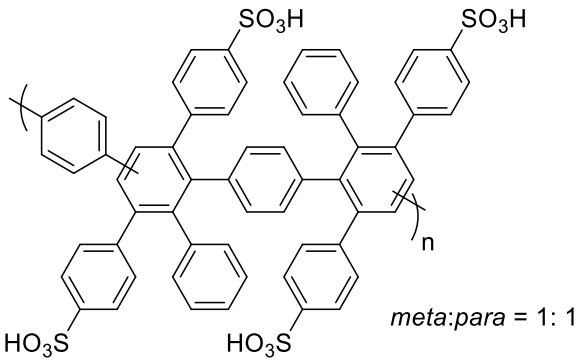

sulfonated phenylated poly(phenylene)

Figure 1-6. Chemical structure of the sulfonated phenylated poly(phenylene) synthesized via pre-functionalization. [64] The number and placement of sulfonic acid groups are precisely controlled.

1.2.3. Catalyst layer

The catalyst layer comprises agglomerates of carbon-supported platinum particles coated with proton exchange ionomers (PEI).[51,76,77] There exists an interface where three reactants of the oxygen reduction reaction meet. The interface is named the triple-phase boundary, and is illustrated in Figure 1-7.[78] The cathodic ORR occurs when protons from the hydrated ionomer, electrons from the carbon support, and O_2 from the gas diffusion layer meet at the surface of Pt particles.[78] The catalyst layer plays an essential role in the fuel cell. Both activation overpotential and mass-transport overpotential (see section 1.1.2) are associated with the sluggish electrochemical kinetics and hindered mass transport, respectively, within the catalyst layer. Each causes a sharp drop in cell voltage and power density in the low and high current density regions. The catalyst activity, affected by its surface morphology, particle size, and support structure, has a crucial influence on the electrochemical performance of the fuel cell.[79–81]

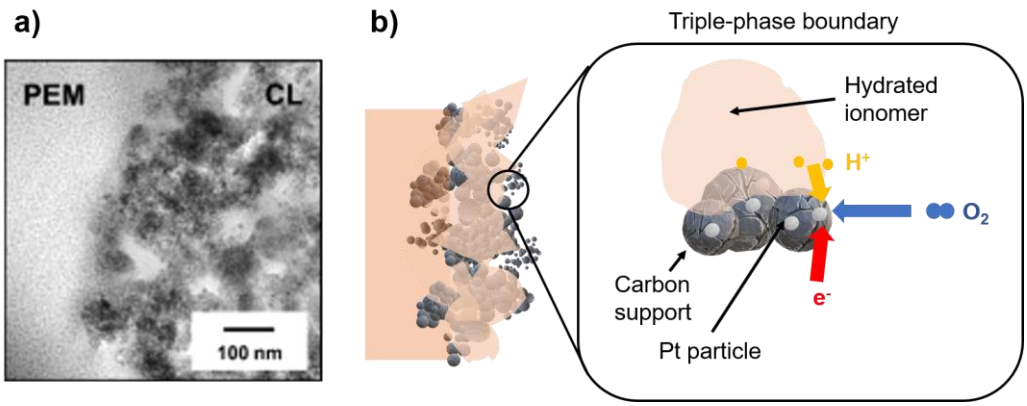

Figure 1-7. a) TEM image of the membrane/catalyst layer interface.[82] Copyright (2000) with permission from the Electrochemical Society. b) Schematic illustration of the cathodic membrane/catalyst layer interface and the triple-phase boundary.

The ionomer serves both as the proton pathway and the binder for the platinum agglomerates, influencing the pore structure and, correspondingly, the mass transport features and catalyst utilization with the CL.[83] To date, the canonical proton exchange ionomer is the PFSA ionomer, Nafion®, because of its high proton conductivity and robust chemical strength.[84–103] Significant amounts of studies have been focused on CL with Nafion® ionomer. The Nafion® ionomer content is found to affect the catalyst layer's pore structure and thickness.[88,104] Excessive presence of ionomer in the CL cripples O_2 transport and egress of H_2O, while deficiency of ionomer results in low proton conductivity and sluggish reaction rate because of the diminished area of the triple-phase boundary.[84–86] Variance in fabrication conditions alters the nature of CL.[105] The influence of various solvents on the dispersion state of Nafion® ionomer and morphology of the CL was also widely studied.[93–98,101–103]

1.3. Water sorption of PEMs

As noted above, the presence of water is crucial within the proton exchange membrane. Water sorption behavior is a fundamental phenomenon altering membranes' phase-separation morphology, and hence structural and mass-transport features.[29] There are many parameters to describe water content within the proton exchange membrane. These parameters are usually interrelated.[29] Hydration number, λ (mol H_2O

/ mol SO_3^-), is ubiquitously used in PEM research and was first brought up by Springer et al.[106] Given large volume of studies and detailed reviews available for the PFSA membranes, discussion in this section (section1.3) will be focused on the water sorption behavior of Nafion® membranes.

1.3.1. Liquid water sorption

The liquid water sorption of PFSA membranes generally decreases with higher equivalent weight (EW),[107,108] increasing heat-treatment temperature,[109,110] lower solvent temperature,[109] contamination, and aging.[111,112] The liquid water sorption process is governed by the solvation of ionic groups by water molecules. Liquid water sorption is determined by the acid concentration, and hence by the ion exchange capacity (IEC) of the membrane. IEC (mmol SO_3H / g dry membrane) represents the number of sulfonic acid groups (mmol) in every gram of dry membrane. Higher IEC of a PEM represents higher water sorption.

1.3.2. Water vapor sorption

Water vapor sorption is more complex than liquid water sorption and is a multiscale, multistep process involving an interplay among water molecules, hydrophilic acid groups, and the hydrophobic perfluorinated polymer backbone.[29] A non-linear, sigmoidal vapor sorption profile against water activity (a, $a = p_{H_2O}/p_{sat} = RH/100$ [113]) is expected. Water vapor sorption is more relevant to the actual running condition of the fuel cell than the liquid water sorption is. To interpret this vapor sorption behaviour, many models were invoked and reviewed in 2019 by Vetter et al..[114] The first type of model is the polynomial fit. It was initially used by Springer's[106] and Hinatsu's[115] research in the 1990s. This method is prevalent because of its simplicity and precision. The latest application of the polynomial fit for water vapor sorption was by Morin et al. in 2017.[116] The polynomial fit is heavily dependent on the polynomial order, and there is no conclusively general equation that can be adopted. Regardless of the precision, there is little physical significance behind the polynomial equation, which limits its further application to relate membranes' sorption behavior to structure features. Other developed models are built on the Flory-Huggins (FH) theory,[115,117,118] Brunauer-Emmett-Teller (BET) theory,[119–

121] or the elastic swelling model.[122,123] These models often lead to lengthy and implicit equations.

Recently, the Park model has been applied to study the sorption isotherms of proton exchange membranes.[124–130] In the Park model, as shown in Figure 1-8 and Equation 1-4, the water sorption (WS) is made of three independent types of sorption: Langmuir-type sorption, Henry-type sorption, and clustering-type sorption.[124,127–130] Individually, each is the major contributor to increase water content in the low, mid, and high relative humidity regimes.

$$\mathrm{WS} = \mathrm{WS}_{\mathrm{Langmuir}} + \mathrm{WS}_{\mathrm{Henry}} + \mathrm{WS}_{\mathrm{Clustering}} \text{ [124–130]} \qquad \textbf{Equation 1-4}$$

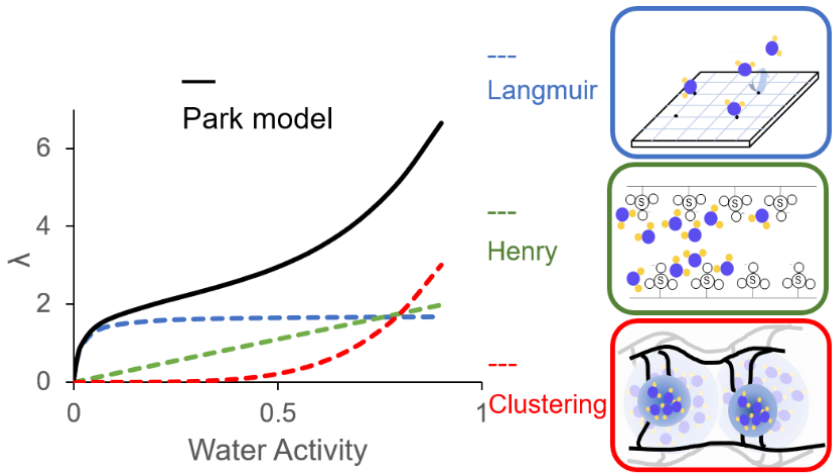

Figure 1-8. Schematic illustration of the Park model depicting the change in hydration number, λ, with water activity.[126]

Langmuir ($WS_{Langmuir}$), Henry (WS_{Henry}), and clustering-type sorption ($WS_{Clustering}$) individually can then be defined as shown in Equation 1-5 to Equation 1-7, respectively.

$$WS_{Langmuir} = \frac{a_L K_L a}{1 + K_L a} \text{ [124–130]} \qquad \textbf{Equation 1-5}$$

$$WS_{Henry} = K_H a \text{ [124–130]} \qquad \textbf{Equation 1-6}$$

$$WS_{Clustering} = n K_A a^n \text{ [124–130]} \qquad \textbf{Equation 1-7}$$

where a is the activity of water, a_L is the specific site capacity, K_L is the affinity constant, K_H is the Henry' law coefficient, n is the aggregate number, and K_A is the aggregation equilibrium constant. The Park model renders an explicit and simple equation, which well approximates the sorption isotherm of the PEM. Also, the Park model bestows insightful physical significance to the parameters in each type of sorptions to interpret and compare membranes' structural/chemical features.

Langmuir-type sorption describes hydration of the membrane surface by a monolayer of water molecules. As seen in Equation 1-5, Langmuir-type sorption is determined by the specific site capacity, a_L, and affinity constant, K_L. The specific site capacity shows the density of surficial, hydrophilic Langmuir sites fixing water molecules on the surface, and relates to the surficial concentration of ionic moieties of PEMs.[129,131] The other parameter, affinity constant (K_L), represents the relative strength of water molecules being secured by the surficial, hydrophilic groups of membranes,[29] and relies on the strength of H-bonds between sulfonic acid groups and water molecules, and therefore the acidity of the sulfonic groups.[124,131] The more acidic the surficial sulfonic group, the larger the K_L value. As shown in Figure 1-8, Henry-type sorption mainly contributes to the water content increase in the mid-relative humidity regime. Henry-type sorption illustrates water sorption as being proportional to the relative humidity during further hydration when water molecules penetrate and interact with the ionic groups within the bulk membrane. The linearity coefficient, K_H , represents the magnitude of water-sulfonic group interactions.[128] Clustering-type sorption is responsible for the sharp increase in water sorption in the high relative humidity regime, as seen in Figure 1-8. Clustering-type sorption approximates the process of water clusters' formation and relaxation of the polymer backbone when accommodating more incoming water molecules.[127–129,131] Indicated in Equation 1-7, clustering-type sorption is featured by both the aggregate number, n, and the aggregation equilibrium constant, K_A. The aggregate number reveals the average size of water clusters, which is reliant on the backbone's flexibility to accommodate water molecules. The aggregation equilibrium constant represents the extent of the water clustering process, and is affected by backbone's affinity with water molecules.[127–129,131]

The effect of temperature on the water vapor sorption isotherm of Nafion® is another area of considerable discussion. Because of the difficulty in acquiring accurate measurements under high temperature and RH, reports on sorption isotherms of PEMs

are sparse.[29] In the wide temperature range of 25 to 90 °C, under 70% RH, almost all literature reported a similar vapor sorption profile of the Nafion® membrane.[110,132–136] Under higher RH near saturation, a general trend of decreasing water content with the temperature was observed.[110,132–134,136] So far, there is no definite explanation for this diminished water vapor sorption at elevated temperatures under higher RH.[29] Studies tend to attribute the reduced water sorption to either the varying surface hydrophilicity of Nafion®[133,137,138] or polymer-water interactions.[118,132,133,139–141]

1.3.3. Schröeder's paradox

In the work of Schröeder, gelatins were found to swell more in liquid water than in saturated water vapor at identical temperature.[142] This observation is controversial from the thermodynamic perspective, as in both cases, liquid and saturated water vapor, the thermodynamic equilibrium should be identical (water activity=1). The term "Schröeder's paradox" is then adopted for similar phenomena observed for other materials. As for Nafion® membranes, Schröeder's paradox also exists. The hydration number for Nafion® membrane in liquid water, λ_{liquid} (22 ±1), is higher than that in saturated water vapor, λ_{vapour} (14 ±1).[109,133,138,139,143–145] Systematic investigations were conducted by Bass and Freger to elucidate the origin of the Schröeder's paradox in the Nafion® membranes.[146–148] They related the difference in water sorption between liquid and vaporous water to the variance of surficial morphology of the Nafion® membrane when in contact with liquid and water vapor.[147,148] As shown in Figure 1-9a, when subject to water vapor, the ionic clusters (micelles) tend to align parallel to the surface, causing a hydrophobic membrane surface to oppose water ingress.[148] However, Nafion® membrane surface is hydrophilic when exposed to liquid water as the hydrophilic micelles are arranged normal to the surface, which favors water transport, as shown in Figure 1-9b.[148] This change in surficial morphology with varying states of water is widely acknowledged by technologies including contact angle measurement,[147,149,150] X-ray,[46,151] atomic force microscope,[152–161] and electrochemical mass-transport measurement.[162] In the end, it must be stated that it is challenging to obtain water vapor saturation (water activity=1) without thermal fluctuation and condensation of liquid water on the membrane surface.

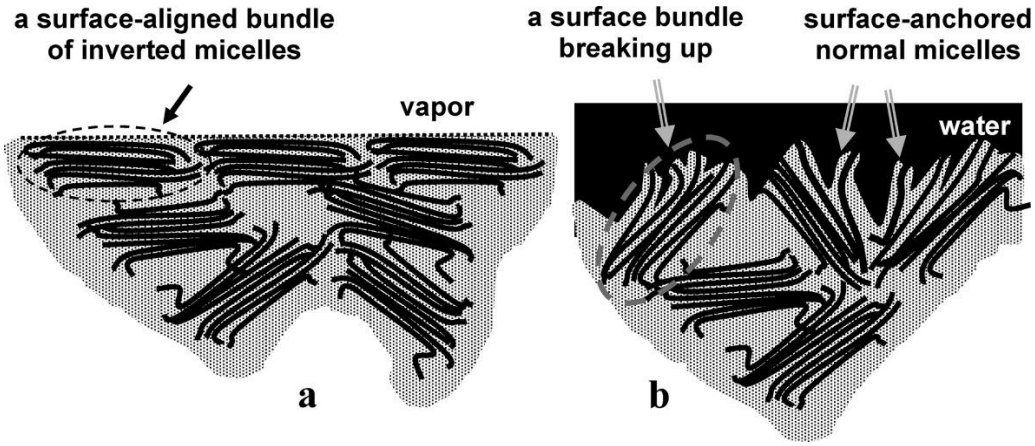

Figure 1-9. Schematic illustration of surficial morphology of Nafion membrane when in contact of (a) water vapor and (b) liquid water. Lines in black represent hydrophilic, ionic clusters (micelles) for water and proton transport pathways.[148] Copyright (2011) with permission from the American Chemical Society.

1.4. Water transport through proton exchange membranes

Besides water sorption, water transports through the proton exchange membrane and the membrane electrode assembly are fundamental for the fuel cell's efficient and stable operation. Water transport phenomena cover a broad scope of mechanisms at different time- and length-scales, accompanied with a wide range of diagnostic techniques. Common types of water transport through Nafion® membranes and examining techniques include[29]:

1. Steady-state (SS) permeation or diffusion[1] under a controlled chemical potential gradient as driving force[136,163,166–172]

2. Transient diffusion measured under a certain relative humidity bias by dynamic vapor sorption (DVS)[124,126,173–177]

3. Local diffusion or self-diffusion by pulsed-field gradient spin-echo (PGSE) nuclear

[1] The terms "steady-state permeation" and "steady-state diffusion" are used as interchangeable.[29] For consistency and legacy from former published papers in the group,[82,126,163–165] the term "permeation" or "permeability" will be used instead of "diffusion" and "diffusivity" for steady-state studies.

magnetic resonance (NMR)[107,110,138,166,178–182] or quasi-elastic neutron scattering (QENS)[49,183–185]

4. Other indirect probing measurements like time-resolved small-angle X-ray scattering (SAXS)/small-angle neutron scattering (SANS),[44,186–188] or Fourier transform infrared-attenuated total reflectance (FTIR-ATR)[189–192]

Due to the expanse of water transport topics and their relevance to this study, only the steady-state permeation and the transient diffusion of Nafion® membranes will be discussed in detail.

1.4.1. Steady-state permeation

Steady-state water permeation primarily measures the molar water flux (J_w) though the membrane under a controlled chemical potential difference of water ($\Delta\mu_w$) that can be achieved by regulating the water concentration on both sides of the membrane. Steady-state water permeation is a crucial phenomenon within the PEM to regain the even distribution of water when subject to a water concentration difference in the fuel cell. The water concentration difference usually occurs between the higher water concentration at the cathode and lower water concentration at the anode.

In an operating fuel cell (see Figure 1-10), water is produced from the oxygen reduction reaction at the cathode. Simultaneously, water within the proton exchange membrane moves with protons from the anode to the cathode due to electro-osmotic drag in a running fuel cell.[18] Electro-osmotic drag may dehydrate the anode side of the membrane while accumulating water at the cathode side. Excessive water at the cathode is likely to hinder the supply of oxygen to the reaction sites and deteriorate the performance of the fuel cell; this is the so-called “flooding phenomenon”. Within the proton exchange membrane, sufficiently high proton conductivity through the membrane is only achieved when it is well hydrated, since the transport of protons requires water. Ionic resistance of the proton exchange membrane increases when it dries out.[193,194] Dehydration within the proton exchange membrane not only increases ionic resistance, but it also generates heat in the membrane that further increases dehydration, reducing the performance of the fuel cell in a vicious cycle of self-destruction.[18] To avoid the flooding phenomenon at the cathode side and dehydration of the anode side, the proton

exchange membrane requires regaining a balanced water distribution. Thus, steady-state water permeance (p) is a fundamental character of a proton exchange membrane.

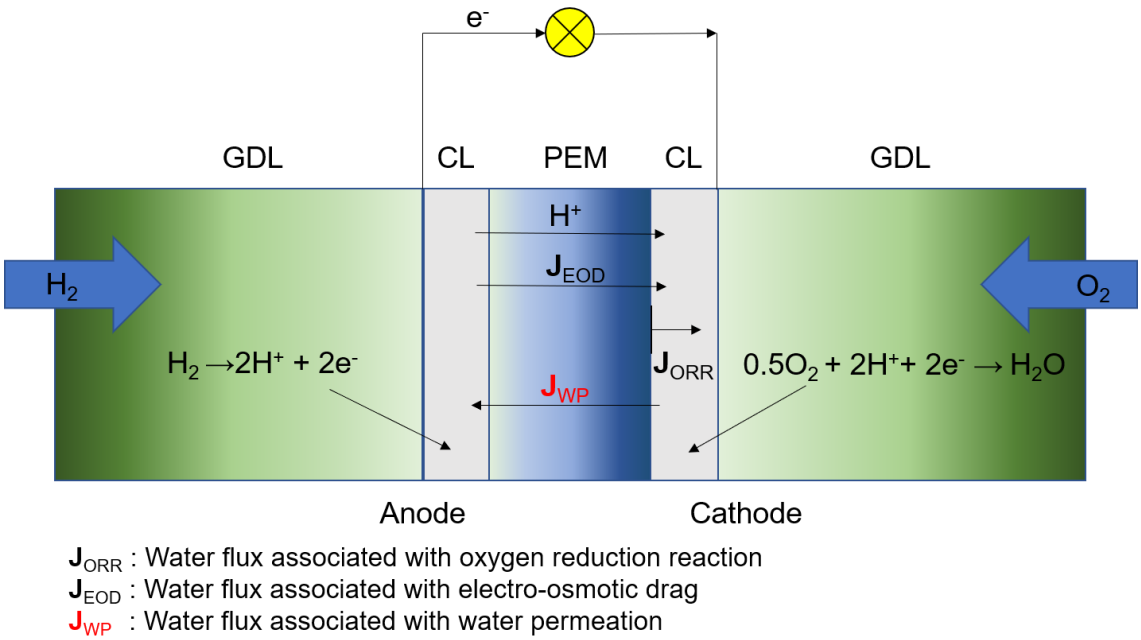

Figure 1-10. Schematic illustration of different water fluxes in an operating proton exchange membrane fuel cell.

Steady-state permeance (p), mathematically, can be expressed as shown in Equation 1-8, in which $\Delta\mu_w$ is the chemical potential gradient of water and J_w is the molar water flux.[29] Steady-state permeabilities reported for the Nafion® membranes vary but are in the same order of magnitude (~ 10^{-6} cm^2 s^{-1}).[29] Steady-state permeability of Nafion® membrane increases with water content. The rate of permeability-increase peaks at λ=3-5 and slows after further hydration.[106,136,176,190,195] This nonmonotonic rate of steady-state permeability with water content has been debated for decades. With low hydration (λ: 1-4), strong ionic interactions exist among initial water molecules and sulfonic groups, facilitating water permeation.[29] Sparsely connected water clusters start to form upon further incoming water and impede water transport when λ>5.[29]

$$p = J_w/\Delta\mu_w \qquad \textbf{Equation 1-8}$$

Steady-state permeation measurements are executed by exposing the membrane to the controlled chemical potential gradient of water and monitoring molar water flux through the membrane.[136,163,166–172] Depending on the physical states of water, there are two typical steady-state water permeation experimental set-ups. These are as follows:

1. Liquid-vapor permeation (LVP): One side of the membrane is in contact with liquid water while the other side is facing water vapor under regulated relative humidity.
2. Liquid-liquid permeation (LLP): While both sides of the membrane are exposed to liquid water, external hydraulic pressure is applied to one side as the driving force.

Detailed description of both LVP and LLP experimental set-up are provided in Chapter 2.

1.4.2. Interfacial water transport and resistance

The resistance to steady-state water permeation process (R) is equal to the chemical potential difference of water across the membrane ($\Delta\mu_w$) divided by the molar water flux (J_w), as shown in Equation 1-9.[29,163,172] The resistance is the sum of the interfacial resistances at both sides of the membrane, and the bulk internal resistance proportional to the membrane thickness (see Equation 1-10 and Equation 1-11). Therefore, a linear plot of steady-state permeation resistance against the membrane thickness provides a slope which renders the internal resistance coefficient and the non-zero intercept at the y-axis, if it exists, as the interfacial resistance. [29,163,172]

$R = \Delta\mu_w / J_w$ [29,163,172] **Equation 1-9**

$R = R_{interfacial,1} + R_{internal} + R_{interfacial,2}$ **Equation 1-10**

$R_{internal} = r \times L$ [29,196] **Equation 1-11**

Where r is the internal resistance coefficient, and L is the membrane wet thickness.

Previous studies revealed that the steady-state permeation can be divided into three separate steps: adsorption, internal water transport, and desorption, as shown in Figure 1-11.[29,196] The vapor/membrane interfacial resistance is considerable for PFSA membranes due to the micelle-parallel morphology at the membrane's surface, as discussed in section 1.3.3.[148,150] By contrast, the liquid/membrane interfacial

resistance is negligible given the high water activity.[82,163–165,172,197] The water vapor/membrane interfacial mass transport has been a popular subject of research. Vapor/membrane interfacial resistance decreases almost exponentially with increasing relative humidity.[157,168] This observation can be rationalized by invoking a humidity-dependent surficial morphology which adopts a less hydrophobic configurations with more ionic channels under higher RH. The humidity-dependent morphology rearrangement has been confirmed with many techniques, including SAXS,[187] Raman spectroscopy,[198] conductive AFM,[157], and X-ray tomography.[199]

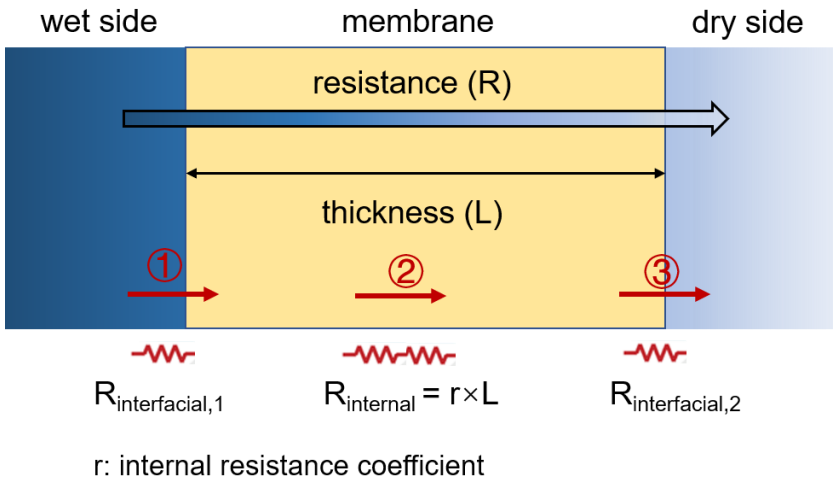

Figure 1-11. Illustration of three steps involved in water transport within the membrane. ① Absorption from liquid water into the membrane. ② Internal water transport. ③ Desorption from the membrane into the gaseous water. Here "wet" denotes liquid water. "Dry" describes water vapor.

1.4.3. Transient water diffusion

In the dynamic environment of an operating fuel cell, the membrane's ability to promptly adjust water content within itself is of paramount importance. Transient diffusion measures the rate of water diffusing into or out of the membrane under an RH bias. Different from the steady-state permeation, transient water diffusion is a more lengthy and complicated process, which involves the accommodation of water molecules, relaxation of the polymer backbone, and multi-level swelling.[18,29] Measurement of the transient

diffusion is accomplished with a dynamic vapor sorption apparatus, which monitors instantaneous changes in the mass of the membrane under a given RH interval and temperature with time. Transient diffusivity, D, is thickness-dependent as shown in Equation 1-12, where k_{sorp} is the effective rate constant of diffusion and L is the wet thickness of the membrane.

$D = k_{sorp}L^2$ [18,29] **Equation 1-12**

The determination of the transient diffusivity or the effective rate constant of diffusion can be strenuous. There are multiple mathematical modeling studies published:

1. Define the characteristic time constant (τ) to be the reciprocal of the effective rate constant of diffusion ($\tau = 1/k_{sorp}$) and to be the time when the mass gain of water reaches 63% (1-1/e, e is Euler's number) of its total mass gain. This method renders value of D relatively accurate within the same order of magnitude. [173]

2. By solving Fick's second law, the transient diffusivity can be determined in Equation 1-13, where M_t represents the instantaneous mass of membrane at t^{th} second, M_0 the initial mass, M_∞ the final mass after being equilibrated for an extended period, and L the membrane thickness.[130,174] This equation has been widely used, though it failed to recognize that the water sorption process within the membrane is accompanied by the relaxation of the polymer backbone.

3. The effective rate constant of diffusion was determined by plotting $ln\left(\frac{M_t-M_0}{M_\infty-M_0}\right)$ versus t, as shown in Equation 1-14. [124]

4. Weibull model incorporates a visco-elastic coefficient, *A*, to Equation 1-14 to emphasize the influence of the relaxation of the membrane's backbone, as shown in Equation 1-15. [200]

$D = \left(\frac{\pi L^2}{16t}\right)\left(\frac{M_t-M_0}{M_\infty-M_0}\right)^2$ [130,174] **Equation 1-13**

$\left(\frac{M_t-M_0}{M_\infty-M_0}\right) \cong exp\,[-(k_{sorp}t)]$ [124] **Equation 1-14**

$\left(\frac{M_t - M_0}{M_\infty - M_0}\right) \cong exp\,[-\left(k_{sorp}t\right)^A]$ [200] **Equation 1-15**

The transient diffusivity (D) of Nafion® decreases as relative humidity increases with a lowest value of ~10^{-9} cm^2 s^{-1} at saturation.[170,173–175,190] This observation of lower transient diffusivity under higher RH is not unexpected, and could be attributed to the following facts:

1. Under higher RH, a slower secondary mechanism pertaining to backbone relaxation becomes dominant. This speculation has been verified by findings of slower diffusivity in polymers with stiffer backbones.[173]

2. Under lower RH (0-20%), Nafion® membranes exhibit a faster, non-Fickian diffusion behavior.[190,192]

3. The chemical potential gradient is smaller at a higher RH regime despite the fixed RH interval.[29]

Transient diffusivity is commonly examined for the sorption process (increasing RH). However, transient diffusivity of the desorption process (decreasing RH) could also be determined and was found to be about one order of magnitude faster.[173,176,177,179,186,192,201,202] The difference in transient diffusivity can be attributed to interfacial effects.[176,200,203,204] From the thermodynamic perspective, the heat of condensation could also explain a lower transient diffusivity in the sorption process.[177] During the sorption process, the heat released from the condensation of water vapor results in a temperature increase at the membrane surface and subsequently lower water activity, both of which diminish the transient diffusivity in the sorption process.[177]

1.5. Water sorption and transport through catalyst layers

The existence of water is not only critical to the proton exchange membrane, but also the catalyst layer. Adequate water content hydrates the catalyst layer and promotes proton conductance. Alternatively, too much water causes flooding and stalls oxygen transport to the catalytic sites at the cathode. The slow oxygen transport is often responsible for decreasing cell voltage and power density of the fuel cell in the high current density

regime.[18,26,28,51,201] A stable and more efficient performance of the fuel cell requires better knowledge of both water sorption and transport through the catalyst layer, which is still scarce. The catalyst layer is composed of a nanometer-thick ionomer film coated on the agglomerates of Pt/C particles.[51,83,201] Therefore, ultrathin PFSA film has been sought after by researchers to investigate the interfacial effect and behavior of ionomer films in the catalyst layer. Kusoglu and Weber reviewed the ultrathin Nafion® film in detail.[29] Holdcroft also reviewed the catalyst layer from an ionomer perspective.[51] A large selection of factors could alter the structure and properties of the ultrathin Nafion® films, including variance in the solvent, substrate, ionomer concentration, post-treatment, and thickness.[29] There are contradicting reports on water sorption and transport through the catalyst layer, and no definite explanation for this contradiction's origin. In general, ultrathin films of Nafion® were reported to possess reduced water content and diffusivity.[29,51] When the thickness of the film decreases to the order of the catalyst layer (~20 nm), the cutback in water sorption and transport are exacerbated. [29,51] An increase of water content within the nanometer scale film of Nafion® was observed by Hickner et al.[205] They attributed this finding to the hypothetically lamellar morphology at the film surface discovered by Majkrzak et al.[206] The use of different substrates, upon which the ultrathin film is coated, was also recognized to increase the water content of the film in Hickner's study. [51] The variance in the carbon support of the catalyst layer could cause variations in water uptake, as reported by Holdcroft et al.[207] A larger fraction of mesopores (< 20nm) in the catalyst layer leads to a more substantial capillary effect and subsequently, a higher water uptake.[207] Electrospray coating, a novel technology for catalyst layer fabrication, was reported to increase the water content in the catalyst layer even when a superhydrophobic surface (contact angle >150°) was used.[208]

Due to the porous nature of the catalyst layer, the diffusivity of water vapor is predicted to be much higher in the catalyst layer than in the bulk membrane by computational studies. [174,209–213] However, only a few experimental examinations exist on water permeation through the membrane electrode assembly. An experimental permeation study reported no significant influence from the traditional catalyst layer, made from Nafion® ionomer, upon the liquid-vapor permeation through the Nafion® membrane.[82] This observation is unexpected, considering the Nafion® membrane/vapor interface limits the rate of water transport through the membrane.[82,165]

1.6. Thesis overview

The dominance of Nafion®, both as the proton exchange membrane and ionomer in the catalyst layer, has remained unchanged for the past five decades.[29,54,56] Many studies during this period have built a relatively mature and complete profile of the structure-property relationship for the Nafion® membranes. By contrast, research on water sorption/transport behavior of emerging hydrocarbon-based polymers is still in its infancy. Even scarcer is the effort to correlate water transport through those polymers to their chemical/structural features. Insights into this transport-structure relationship of emerging HC-based PEMs will shed light on the future synthesis of more desirable materials.

The objective of this thesis is to investigate water sorption and transport behaviors of novel hydrocarbon-based PEMs and to identify the structural features that would affect these behaviors. In the work leading up to this thesis, a comprehensive water sorption and transport research scheme was executed by the author (Figure 1-12). This included steady-state permeation, vapor sorption isotherm, and transient diffusion. Mathematical models were applied to interpret the water sorption and transport behavior and gain information such as the membrane/vapor interfacial resistance, the transient diffusivity, and the surficial site capacity of membranes. Surface characterizations, such as contact angle measurement, conductive AFM, and in situ fuel cell analyses, were also carried out to explore the physical properties of membranes. Collectively, transport measurements, numerical models, and characterizations were integrated to generate an insightful structure-transport correlation.

The membranes studied in this thesis are the second generation of the sulfonated phenylated poly(phenylene)s (Figure 1-6), with precise structure modifications as seen in Figure 1-13 and Figure 1-14. Figure 1-13 is the sulfonated phenylated poly(phenylene) biphenyl (SPPB), which exhibits exceptional chemical stability and electrochemical performance both as the membrane[63] and the ionomer[214] with the precise insertion of a biphenyl spacer. Figure 1-14 displays a series of sulfonated phenylated poly(phenylene)-based polymers containing an increasing number of strategically placed N-atoms to reduce acid concentration and swelling. These two modified sulfonated phenylated poly(phenylene)s, with precisely controlled structures, provide a precious opportunity for an extensive water sorption and transport research on novel hydrocarbon-based PEMs.

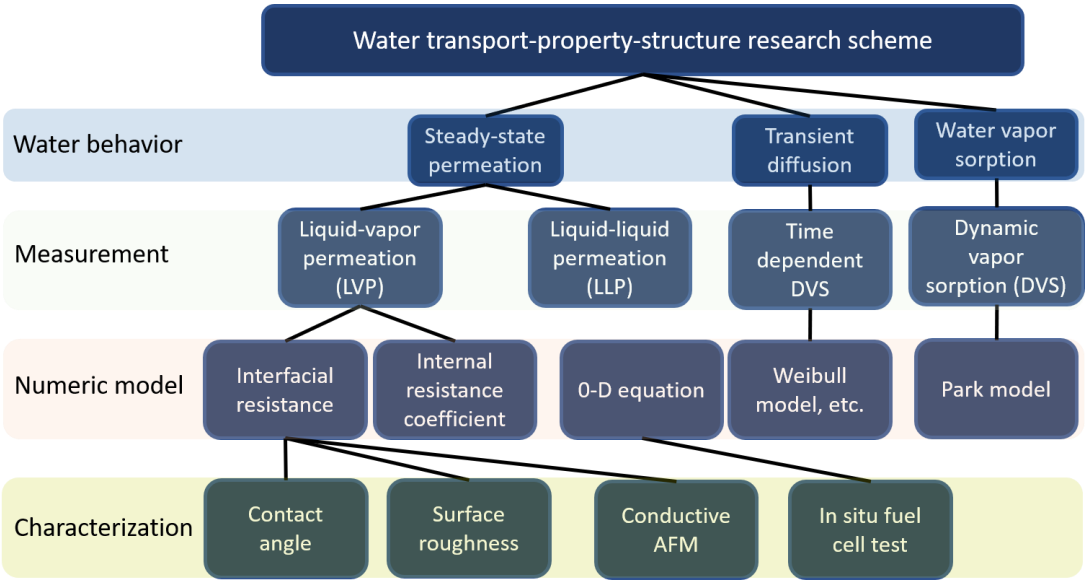

Figure 1-12. Research scheme for investigating water transport and structure-property relationships

Chapter 2 describes the experimental set-up, material preparation, and data processing.

Chapter 3 reports water sorption isotherms and steady-state permeation study of the sulfonated phenylated poly(phenylene) biphenyl (Figure 1-13), and compares it to a HC-based reference membrane, sulfonated poly(arylene ether) (SPAE), and a commercial reference membrane, N211. Sorption isotherms are investigated using a DVS analyzer, then fitted and interpreted using the Park model, which provides property information such as surficial hydrophilicity and relative acid content of the membranes. Vapor sorption isotherm profiles and membrane-vapor interfacial resistance are related to membranes' chemical/structural feature and confirmed with characterizations from conductive AFM and contact angle measurement. The motive of this chapter is to relate the difference in chemical structure of emerging HC-PEMs to their water sorption and transport features. Thus, the findings in this study can aid future structural design and synthesis of hydrocarbon-based polymers.

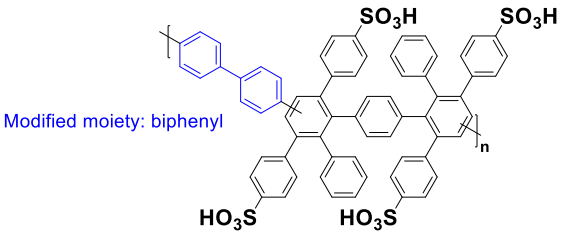

Figure 1-13. Chemical structure of the sulfonated phenylated poly(phenylene) biphenyl (SPPB). Highlighted in blue is the modified moiety as opposed to the original structure in Figure 1-6.

Chapter 4 then describes the water sorption and transport study on a series of sulfonated phenylated poly(phenylene)-based polymers containing identical structures but with an increasing number of strategically placed N-atoms, in the form of pyridyl units (Figure 1-14). Interactions between the basic pyridyl groups and the sulfonic acid groups with the polymer reduce the effective acid content, decrease dissociation of protons, and subsequently reduce water swelling at the cost of hindered mass transport. The motive behind this study is to examine the influence of regulated acid-base interactions within the polymer on water sorption, steady-state water permeability, transient diffusivity, and proton conductivity. Therefore, the ideal number and position of the incorporated pyridyl units in the SPPP would hopefully be assigned to restrict water swelling of the PEM without considerable loss of the proton conductivity.

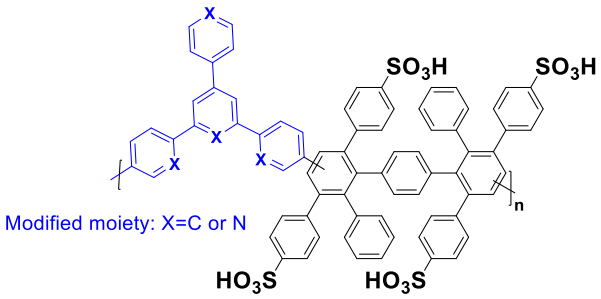

Figure 1-14. General chemical structure of the sulfonated phenylated poly(phenylene) containing precisely placed N-atoms (1-4). Highlighted in blue is the modified moiety as opposed to the original structure in Figure 1-6.

Chapter 5 describes studies of water vapor uptake, transient diffusion, and steady-state permeation through catalyst layers (CL) containing sulfonated phenylated

poly(phenylene) biphenyl (Figure 1-13) with different ionomer contents and compares them to the traditional CLs containing Nafion® ionomer. The motive is to understand how hydrocarbon-based ionomers affect water uptake and mass transport through the catalyst layer. In situ fuel cell analyses are performed on membrane electrode assemblies with these novel CLs. The polarization curves are approximated with mathematical models, and parameters such as the electrochemical surface area (ECSA) and internal protic resistance are extracted. Mass transport performance of these catalyst layers are also related to surficial characterizations such as surface roughness and contact angle measurements.

Chapter 6 summarizes and evaluates each of the three projects individually, and this thesis work collectively. It also proposes three possible directions for future work related to further investigating the structure-transport correlation of hydrocarbon-based proton exchange membranes, simplifying the units of steady-state permeability for broader applications and modeling purposes, and understanding interfacial transport phenomenon by studying ultrathin HC-based membranes.

Chapter 2. Materials, techniques, and methods

2.1. Overview

This chapter describes material preparation, experimental set-ups, water sorption and transport measurements, mathematical processing, and operating parameters applied in the research. Variations from the description in this chapter will be specified in the experimental section of the latter chapters.

2.2. Material and preparation

2.2.1. General materials

Milli-pore water (18 MΩ cm) was attained from Millipore Gradient Milli-Q. Compressed nitrogen gas (purity >90%) was from Praxair Inc. Commercial Nafion® D520 dispersion of 1000 g mol^{-1} equivalent weight (EW) (Ion Power Inc., lot SGA-12-02CS) was used as-received. Commercial carbon supported platinum particles (TEC10E50E, lot 109–0111, 46.4% Pt) were purchased from Tanaka Kikinzoku Kogyo (TKK).

2.2.2. Membranes

Commercial Nafion® membranes of 1100 g mol^{-1} equivalent weight with dry thickness of 25 μm (N211), 54 μm (N212), 131 μm (N115) and 181 μm (N117) were purchased from Sigma-Aldrich and used as-received.

Sulfonated phenylated poly(phenylene) biphenyl (SPPB) membranes and ionomers were obtained from procedures described in the literature,[63] and used as received from Dr. Michael Adamski of Simon Fraser University. SPPB membranes of 3.2 mmol g^{-1} ion-exchange capacity were provided with dry thickness of 22, 35, 49, and 60 μm. Thicknesses of membranes were measured using a micrometer (Mitutoyo Quickmike Series MDC-Lite, ± 0.1 μm).

Sulfonated poly(arylene ether) (SPAE) membranes and ionomers were received from Professor Wen -Yao Huang of National Sun Yat-Sen University (Taiwan) and used as

received. Sulfonated poly(arylene ether) membranes of 3.2 mmol g^{-1} ion-exchange capacity were provided with dry thickness of 22, 24, 36, and 50 μm. Thicknesses of membranes were measured using a micrometer (Mitutoyo Quickmike Series MDC-Lite, ± 0.1 μm).

2.2.3. Catalyst ink preparation

Catalyst inks (1% solids by weight in 1:3 v/v water/methanol) were prepared using carbon supported platinum particles and a dispersion of i) Nafion® (EW 1000, DuPont) and ii) SPPB ionomer with 5% and 3% w/v ionomer in MeOH, respectively. A third of the required water was added initially to the Pt/C solid, and the slurry was sonicated in a ultrasonic sonicator (Bransonic B1510R-MTH, 2 kHz, 70 W output power) for 10 min to ensure the Pt/C particles were wetted. The slurry was stirred on a stir plate in a fume hood, and a third of the required methanol was added dropwise and stirred for 15 min. To the resulting dispersion was then added the ionomer solution dropwise till the ionomer content in the ink reached 10, 15, 20, 25, and 30 wt%, and the resulting ink was stirred for 10 min. The remaining quantity of methanol and water were added dropwise. The resulting catalyst ink solution was sonicated for 2 hours. More detailed composition information of each catalyst ink is provided in Table C 1 and Table C 2, in Appendix C.

2.2.4. Preparation of samples for conductive atomic force microscopy

Carbon-supported Pt (46.4 wt % Pt) was dispersed into a methanol/water (50:50 vol%) solution, followed by 1 h of sonication. Then, 5 wt % of: a) SPAE, or b) SPPB ionomer solution was added dropwise to provide 20 wt % ionomer content of solids in the mixture (catalyst ink). After 1 h of sonication, the catalyst ink was deposited onto one side of the membrane a) SPAE, or b) SPPB by the automated spray coater (EFD, Nordson Co.) with catalyst loading set as 0.4 mg cm^{-2} (flow rate 0.25 ml/min, idle power 2 Watts, run power 0.5 Watt). The one-side-coated membranes were later stored in Milli-pore water with 1M H_2SO_4 for one week before test. Membranes' coated sides were then affixed to the carbon sheets with carbon tape, both of which had been soaked in catalyst ink for at least 24 h.

2.3. Liquid water sorption

Membranes were stored in Milli-pore water at 30 °C for 2 days. After being removed from water and surface dried with lint-free laboratory wipes, membranes were weighted right after to determine the wet weight (W_{wet}) and wet volume (V_{wet}). Then membranes were dehydrated in vacuum at 80 °C until the weight was constant. Once sample had cooled to room temperature under vacuum, dry weight (W_{dry}) was immediately determined after removal from the vacuum chamber. There was a minimum of 3 replicates for each measurement. The water uptake, water percentage, hydration number, and water volume fraction were calculated using Equation 2-1 to Equation 2-4, respectively. ρ_{water} and $IEC[mmolg^{-1}]$ are the density of water and ion exchange capacity of the membrane, respectively.

$$Liquid\ water\ uptake,\ WU = \frac{W_{wet}-W_{dry}}{W_{dry}} \times 100\%\ [163] \qquad \textbf{Equation 2-1}$$

$$Liquid\ water\ percentage, Wt.\% = \frac{W_{wet}-W_{dry}}{W_{wet}} \times 100\%\ [163] \qquad \textbf{Equation 2-2}$$

$$Hydration\ number,\ \lambda = \frac{Water\ uptake[\%]\times 10}{18[g\ mol^{-1}]\times IEC[mmol\ g^{-1}]}\ [163] \qquad \textbf{Equation 2-3}$$

$$Water\ volume\ fraction,\ X_V = \frac{\frac{W_{wet}-W_{dry}}{\rho_{water}}}{V_{wet}}\ [163] \qquad \textbf{Equation 2-4}$$

2.4. Steady-state permeation

2.4.1. Liquid-vapour permeation

Circular membranes (diameter: 6 cm) were sandwiched between 2 polyethylene (PE) laminating films. A round center (diameter: 4 cm) of the membrane was exposed. The sandwiched assembly was placed floating on the water in the stainless-steel container, as seen in the Figure 2-1. The container was wrapped around by an external heating band (Watlow electric Mfg. Co, 100W) to regulate temperature. Then, the container was placed in an environmental test chamber (SH-241, ESPEC North America Inc.) with temperature set at 70 °C and RH at certain values (30%, 50%, 70%, or 90%). Mass difference between the initial and final weight of the apparatus (container, water, and the membrane assembly)

after a certain period (3 to 18 hours) was determined as the water flux through the membrane. The time interval between the determination of initial and finial weight was chosen so that the weight difference was larger than 100 g to reduce errors. There were at least 3 replicates conducted for each sample. [82,126,163–165,172,197]

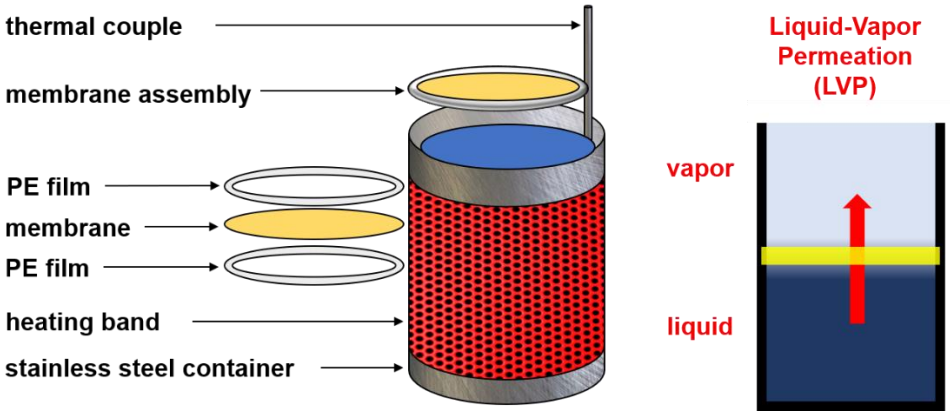

Figure 2-1. Schematic illustration of the custom-made set-up for liquid-vapor permeation measurement.[126]

2.4.2. Liquid-liquid permeation

Circular membranes (diameter: 2.5 cm) were secured between an O-ring and screen support in a flow cell. The flow cell was then connected to a syringe pump and flowmeter (see Figure 2-2). The water flux (flow rate) through the membrane was determined by the flowmeter (20 µL min^{-1}, µ-FLOW, Bronkhorst HI-TEC), while the applied hydraulic pressure (differential pressure) was recorded by the pressure transducer (PX302-100GV, Omega Engineering Inc.). There were at least 3 replicates conducted for each sample.[82,126,163–165,172,197]

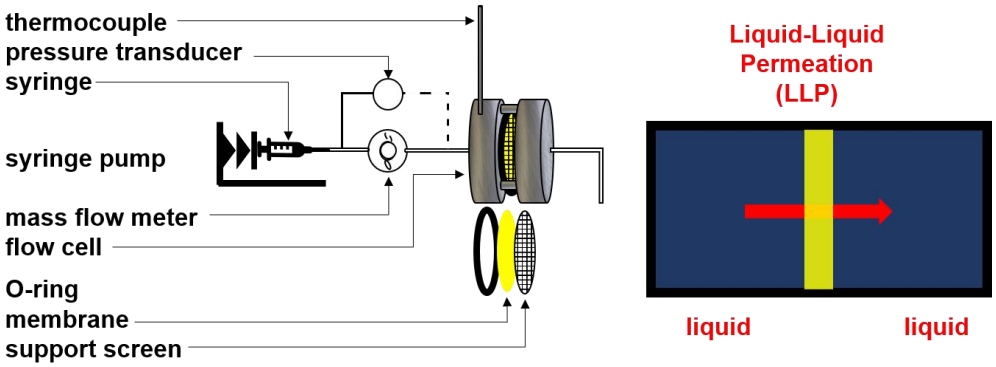

Figure 2-2. Schematic illustration of the custom-made set-up for liquid-liquid permeation measurement.[126]

2.4.3. Permeability and resistance

Chemical potential determination

At temperature (x), the chemical potentials of water in the liquid and vaporous state are defined in Equation 2-5 and Equation 2-6, respectively. $\mu^{\circ}{}_{liq\_STD}$ and $\mu^{\circ}{}_{vap\_STD}$ are the standard chemical potentials for liquid water and vapor at 298 K, 1 atm: -237.18 kJ mol^{-1} and -228.59 kJ mol^{-1}, respectively.[163] γ_{liq} and γ_{vap} are temperature coefficients for the chemical potential of liquid water and vapor: - 69.9 J mol^{-1} K^{-1} and -188.7 J mol^{-1} K^{-1}, respectively.[163] For example, at 70 °C or 343 K, μ_{liq_343K} and μ_{vap_343K} are -240.33 and -237.08 kJ mol^{-1}, respectively.[163]

$$\mu_{liq\_xK} = \mu^{\circ}{}_{liq\_STD} + \gamma_{liq}(T_{(x)} - T_{STD}) \text{ [163]} \qquad \textbf{Equation 2-5}$$

$$\mu_{vap\_xK} = \mu^{\circ}{}_{vap\_STD} + \gamma_{vap}(T_{(x)} - T_{STD}) \text{ [163]} \qquad \textbf{Equation 2-6}$$

At 343 K and relative humidity (y % RH), the chemical potential of water vapour can be determined by Equation 2-7 as shown below. R, T, $p_{sat-vap}$ and p_{tot} describe the universal gas constant, temperature in Kelvin, saturated water vapor pressure at assigned temperature and the total pressure of the ambient environment, respectively.[163]

$$\mu_{vap\_RH(y\%)} = \mu_{vap\_343K} + RTln\left[\frac{\left(\frac{y}{100}\right)p_{sat-vap}}{p_{tot}}\right] \text{ [163]} \qquad \textbf{Equation 2-7}$$

At 343 K and under external hydraulic pressure (z atm), the chemical potential of liquid water is defined as seen in Equation 2-8. Here, δ stands for pressure coefficient of chemical potential, 1.990 J mol^{-1} atm^{-1}.[163]

$$\mu_{liq\_p(z)} = \mu_{liq\_343K} + \delta[p(z) - p_{STD}] \text{ [163]} \quad \textbf{Equation 2-8}$$

Therefore, the chemical potential difference between liquid water and water vapour at 343 K and y % RH in liquid-vapor permeation is shown as in Equation 2-9.[163]

$$\Delta\mu_{LVP\_RH(y)} = \mu_{liq\_343K} - \mu_{vap\_RH(y)} \text{ [163]} \quad \textbf{Equation 2-9}$$

Also, the chemical potential difference in liquid-liquid permeation is shown at 343 K and z atm is calculated as in Equation 2-10.[163]

$$\Delta\mu_{LLP\_p(z)} = \mu_{liq\_p(z)} - \mu_{liq\_xK} \text{ [163]} \quad \textbf{Equation 2-10}$$

Water permeability (P)

Water permeability is defined as in Equation 2-11, the multiplication between the water permeance (p, the slope of water flux against chemical potential gradient) and wet thickness of the membrane (L).[163]

$$P = p \times L \text{ [163]} \quad \textbf{Equation 2-11}$$

Permeation resistance (R)

From Equation 2-12, permeation resistance, the molar-normalized energy need for water flux though the membrane (J, mol m^{-2} s^{-1}), is calculated.[163] $\Delta\mu$ is the chemical potential difference between the two sides of the membrane.

$$R = \frac{\Delta\mu}{J} \text{ [163]} \quad \textbf{Equation 2-12}$$

2.5. Dynamic vapour sorption

A dynamic vapour sorption analyzer (DVS-Adventure, Surface Measurement Systems, U.K.) was employed in this study, as shown in Figure 2-3. Basically, it is a precise microbalance system (Ultrabalance™, ± 0.1 μg), one sample and one reference

balance, in a temperature and RH regulated chamber. The relative humidity was regulated by purging a controlled mixture of water saturated and dry nitrogen gases (> 90%, Praxair, Inc.) into the chamber. The computer simultaneously monitors the changes in the mass of sample (from the microbalance) in response to the RH changes (from the humidity probe) against time. All membranes were equilibrated in the Milli-pore water at room temperature before measurement. Water vapor uptake measurements started with dehydrating the samples in the DVS analyzer under 0% RH and 80 °C for overnight. Then in the operation, relative humidity was firstly increased then decreased stepwise (10% RH each step) as programed. Sufficient time (> 100 min) was provided for samples to equilibrate in each RH stage before further hydration/dehydration. In the time-dependent mode, the instantaneous mass of the membrane and relative humidity were recorded every second.

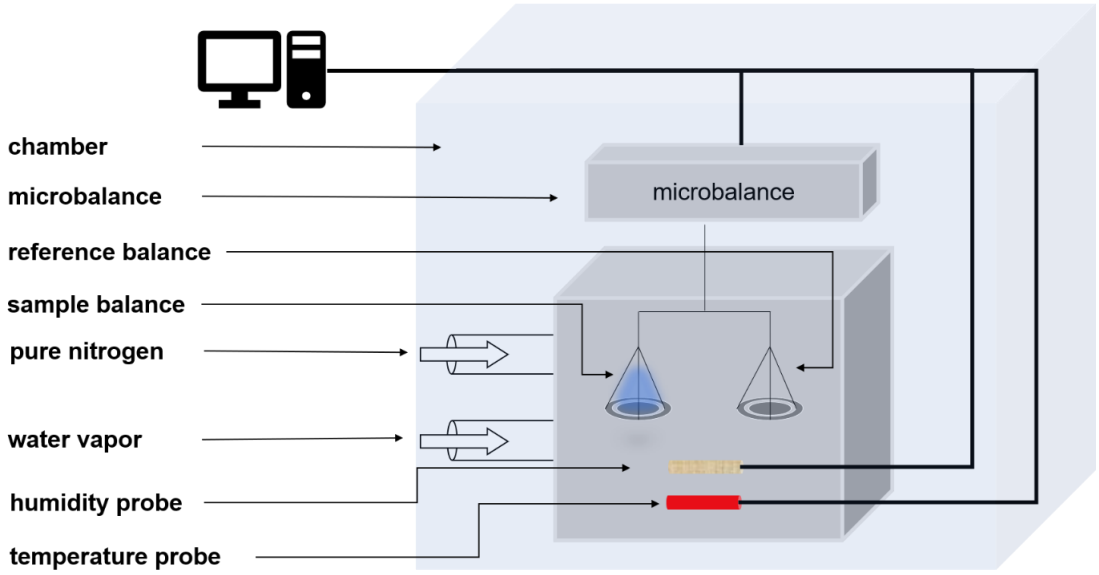

Figure 2-3. Schematic illustration of a dynamic vapor sorption analyzer.

2.6. Ion exchange capacity

Approximately 0.1 g of membrane was placed in 1 M HCl solution for more than 12 h. Membrane was then transferred and stored in Milli-pore water for 30 mins. The Milli-pore water was decanted and refilled every 30 mins, 3 times in total. After, the acidified membrane was equilibrated in 50.00 mL of 2.0 M NaCl solution for 2 h with occasional agitation. The solution was titrated with the standardized NaOH solution (0.025 M) to pH = 7.0. Then, the membrane was transferred into 0.1 M HCl solution for 1 h and rinsed with

Milli-pore water. The membrane was dried at 80 °C under vacuum overnight to determine its dry weight. Ion exchange capacity (IEC) was calculated as represented in Equation 2-13. $V_{(NaOH,mL)}$ and $C_{(NaOH,M)}$ are the volume and molarity of titrant used, respectively, and W_{dry} is the mass of a fully dried membrane sample.

$$\mathrm{IEC}(\mathrm{mmol}\, SO_3H/g) = \frac{V_{(NaOH,ml)} \times C_{(NaOH,M)}}{W_{dry}} \text{ [163]} \qquad \textbf{Equation 2-13}$$

2.7. Proton conductivity and mobility

Membranes of small strips (1.0 × 0.5 cm) were placed onto a conductivity cell in a two-probe configuration as shown in Figure 2-4. The cell was placed inside the environmental chamber (Espec model SH-241) and equilibrated to assigned temperature (30 or 80 °C) and relative humidities. Membrane resistance (R) was determined by the impedance analyzer (Solartron 1260 frequency response analyzer) with AC frequencies set 10 MHz to 100 Hz. With Equation 2-14, Ionic conductivity (σ) was determined. As shown in both Figure 2-4 and Equation 2-14, A is the cross-sectional area of membrane for the resistance measurement and L is the distance between the two electrodes.

$$\sigma = \frac{L}{R \times A} \text{ [194]} \qquad \textbf{Equation 2-14}$$

The effective proton mobility, μ', was calculated from Equation 2-15, where *F* is the Faraday's constant, and $[-SO_3H]$ is the acid concentration, which was determined as in Equation 2-16.[194]

$$\mu' = \frac{\sigma}{F \cdot [-SO_3H]} \text{ [194]} \qquad \textbf{Equation 2-15}$$

$$[-SO_3H] = \frac{n(-SO_3H)}{V_{wet}} \text{ [194]} \qquad \textbf{Equation 2-16}$$

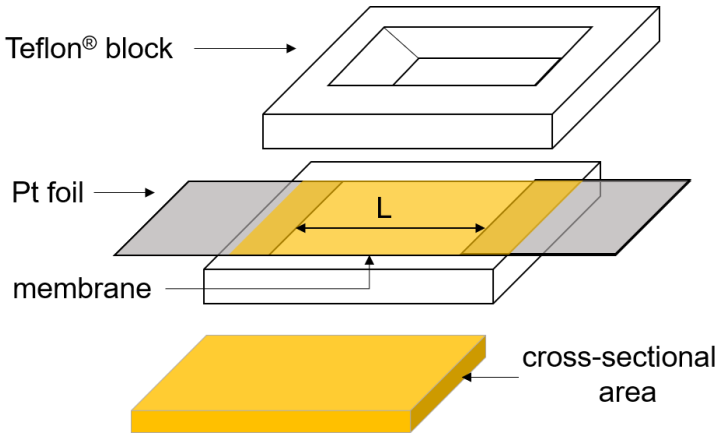

Figure 2-4. Schematic illustration of proton conductivity cell with the membrane dimensions.

2.8. Contact angle measurement

Before testing membranes were dried in vacuum and equilibrated in a desiccator. The OCA 15 Contact Angle Goniometer (FDS future digital scientific co.) was employed at room temperature (22 °C) in a dust-free, class 100 clean room with RH regulated at 40%. In the measurement, a sessile drop (7 µL) of Milli-pore water was dispensed on the membrane by an electronically controlled syringe. The integrated camera focus was adjusted to obtain a sharp drop image. The base line of the membrane substrate and outline of the droplet were manually determined by eye. Contact angle was then analyzed by the OCA 15 Surface Analysis software. There were 10 replicates for each sample for repeatability.

2.9. Conductive atomic force microscopy

The surficial conductivity examination was executed with the atomic force microscope (Dimension Icon, Bruker Corp.) in the “PeakForce-TUNA^{TM} mode”. The examination was carried out in an ambient environment (22 °C and 40 % to 50 % RH). Figure 2-5 is an operating conductive AFM with a Pt/Ir coated silicon tip as a nanoelectrode probe to detect regional ionic current on the surface of the membrane. During examination, direct current voltage bias is introduced to the sample between the sample holder and the conductive tip. Polarization is produced as a result. Subsequently, H_2 and O_2 evolution reactions occur at the AFM tip and sample holder, respectively. Proton produced at the sample holder

then transport through the ionic channels, if open, across membrane to form hydrogen at the other side. Consequently, the ionic current is sensed.[215]

Surficial roughness measurements were conducted by atomic force microscope (AFM) (Dimension Icon, Bruker Corp.) with tapping mode in area 2 by 2 μm. The examination was carried out in an ambient environment (22 °C and 40 % to 50 % RH).

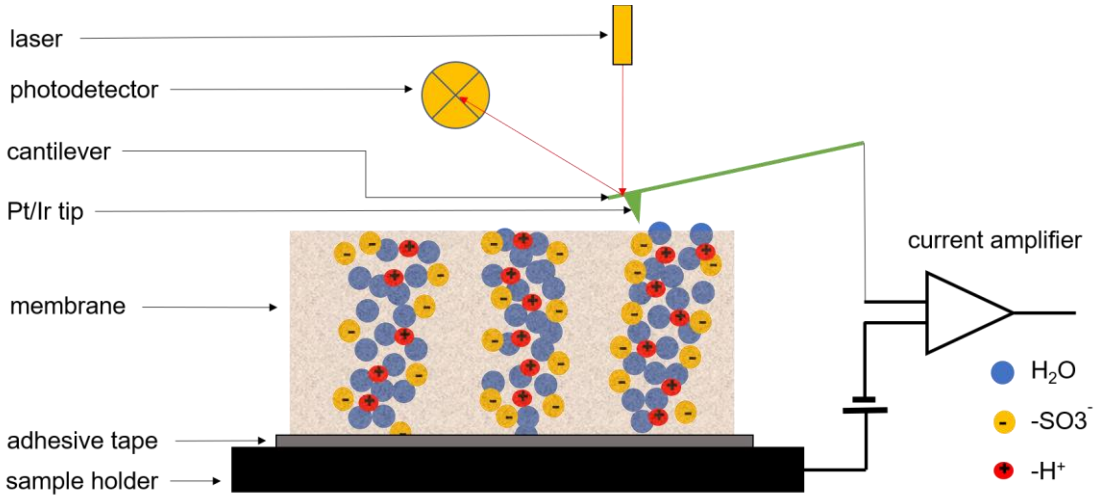

Figure 2-5. Schematic diagram of the conductive AFM.

2.10. Mechanical stress test

A standard ASTM D638-4 cutter was employed to cut the polymeric membranes into barbell-shape samples. Under ambient conditions (23 ^oC, 40% RH), mechanical stress tests were conducted using an Instron 3344 Series pull testing system (crosshead speed at 5 mm min^{-1}). Five membrane samples for each polymer were evaluated. Errors are reported as the standard deviation.

Chapter 3. Water transport through hydrocarbon-based proton exchange membranes

The work in this chapter has been published in: Y. Wu, M. Adamski, H.-F. Lee, S. Holdcroft, Water transport through hydrocarbon-based proton exchange membranes, J. Membr. Sci. (2020) 118276. https://doi.org/10.1016/j.memsci.2020.118276.

Yang Wu: Conceptualization, Investigation, Formal analysis, Writing - original draft. **Michael Adamski:** Investigation, Writing - review & editing. **Hsu-Feng Lee:** Investigation. **Steven Holdcroft:** Supervision, Conceptualization, Writing - original draft. Supporting information is provided in Appendix A.

The authors thank Professor Wen-Yao Huang of National Sun Yat-Sen University for providing SPAE materials.

3.1. Introduction

In the hydrogen economy era, the future of proton exchange membrane fuel cell is promising[11]; and the research on new materials as the proton exchange membrane has gained particular attention.[18,29,68] In general, hydrocarbon-based proton exchange membranes are less gas-permeable, usually more proton conductive in the hydrated state, more environmental friendly, and more versatile to synthesize with multiple developed synthetic routes than their perfluorosulfonic acid counterparts.[29,53,68] There is a large class of hydrocarbon-based PEMs, which incorporates the sulfonated aromatic groups onto the backbone.[21,53,214] Typical statistical copolymers include sulfonated poly(arylene ether ketone)s,[65,66] sulfonated poly(aryl ether sulfone)s,[58,59] sulfonated poly(phenylene)s,[61–64] and sulfonated poly(benzimidazole)s.[31–34]

Enormous interest has been focused on the synthesis and increasing proton conductance of new hydrocarbon-based PEMs. However, there are few water sorption and transport studies on hydrocarbon-based polymers. For instance, there are little reported on the water vapor sorption isotherm characters of hydrocarbon-based PEMs.[125,127,218] Several publications has focused on the hydrocarbon-based anion exchange membranes.[124,128,173,219,220] In the aforementioned studies, a phenomenological equation in the Park model, was employed to approximate the sigmoidal isotherm curve of water sorption against water activity.[124,127,128,173,219–221] The Park model, with its distinctive physiochemical coefficients, assists to reveal and compare the chemical and structural characters among the hydrocarbon-based PEMs. As for the experimental steady-state water permeation study, there is only one that is focused on the hydrocarbon-based PEM. In this research, the sulfonated poly(ether ether ketone) (SPEEK) is found to possess both a higher internal and interfacial resistance than that of the Nafion® membrane.[197] The authors attributed this finding to the less organized ionic channels and possibly poorer surficial hydrophilic domain connectivity of the SPEEK membrane.[197] Given the limited understanding of water sorption and transport through the hydrocarbon-based PEMs, a dedicated study concentrating on vapor sorption isotherms and steady-state water permeation is much needed for emerging HC-based membranes.

Recently, a highly stable, proton-conductive hydrocarbon-based membrane - sulfonated phenylated poly(phenylene) biphenyl (SPPB) - was reported (Figure 3-1).[63]

This SPPB polymer (IEC: 3.2 mmol g^{-1}) is the structure-modified second-generation of the sulfonated phenylated poly(phenylene) previously from the Holdcroft group,[64] with enhanced chemical stability and reduced water swelling by the precise incorporation of the biphenyl group (Figure 3-1). SPPB shows proton conductivity of 172 mS cm^{-1} at 95% RH and 80 °C, which is higher than N211 (113 mS cm^{-1}) in the identical environment.[63] Regardless of the SPPB's excellent performance in the in situ fuel cell test,[63] very little is known about its water sorption and transport characters. Hence, SPPB allows an opportunity for an extensive steady-state permeation and water vapor sorption isotherm study on novel hydrocarbon-based PEMs. For comparison, the sulfonated poly(arylene ether) (SPAE) with the identical IEC (3.2 mmol g^{-1}) is examined as the hydrocarbon-based reference (Figure 3-1), and the perfluorosulfonic acid membrane N211 examined as a commercial reference. SPPB, possessing a completely aromatic backbone, probably is more hydrophobic than SPAE, even though both membranes' backbones are densely functionalized with sulfonic acid groups.[57]

In this chapter, water vapor sorption isotherms of SPAE and SPPB were obtained by the DVS analyzer and interpreted using the Park model, and compared to Nafion® membranes. Moreover, steady-state water permeation measurements were executed and membrane/vapor interfacial resistances for both HC-based membranes were determined. The water sorption and transport behavior were later compared and correlated with other characterization techniques, contact angle measurement and conductive atomic force microscope (AFM). The underlying motivation behind this research is to relate the difference in chemical structure of emerging HC-PEMs to their water sorption and transport features. Therefore, the findings in this study is presumably beneficial to future structure design and synthesis of hydrocarbon-based polymers for uses in electrochemical devices.

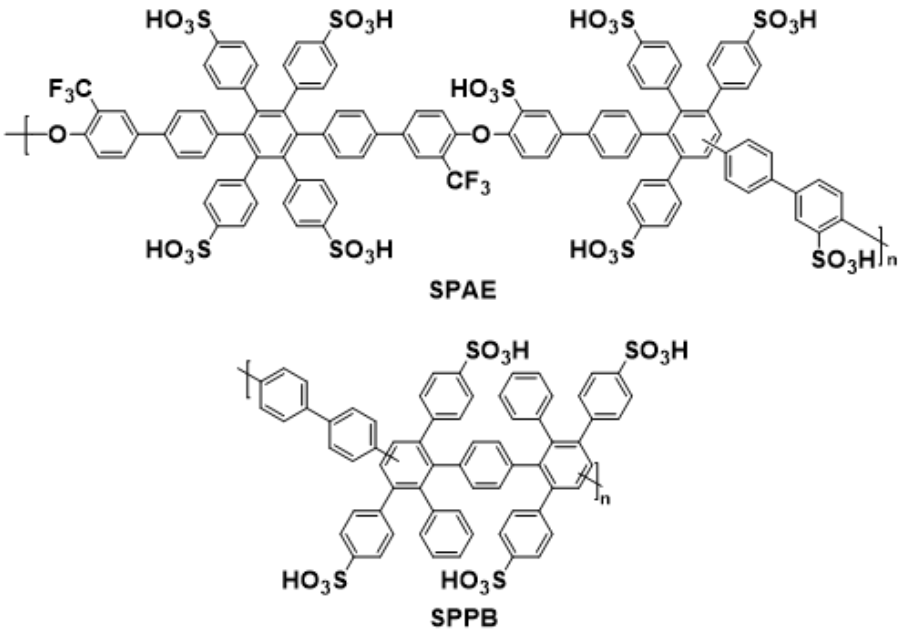

Figure 3-1. Chemical structures of sulfonated poly(arylene ether) (SPAE) and sulfonated phenylated poly(phenylene) biphenyl (SPPB).

3.2. Experimental

3.2.1. Materials

Detailed information on the deionized water (Milliipore water), commercial Nafion® membranes, SPAE membranes, and SPPB membranes are given in section 2.2, chapter 2.

3.2.2. Experimental techniques

Sorption isotherm, liquid-vapour permeation, liquid-liquid permeation, contact angle measurement, and conductive AFM are described in detail in chapter 2. Sorption isotherm, LVP, and LLP measurement were run at 70 °C. Also, detailed instruction on permeability, and resistance determination are provided in chapter 2.

3.3. Results and discussion

3.3.1. Liquid water sorption

Listed in Table 3-1 are liquid water sorption data for membranes immersed in liquid water at 70 °C. For the N211 membrane, the hydration number (19 ± 1) and liquid water uptake (31 ± 3) % in this study are consistent with previously reported values.[163–165] The liquid water contents in both hydrocarbon membranes SPAE and SPPB are higher than that of N211. For instance, water uptake in SPAE and SPPB is approximately 5 and 6 times greater than N211, respectively. This is not surprising, as both SPAE and SPPB membranes possess an obviously higher IEC (approx. 3.5 times greater) than Nafion 211. Due to the high IEC of the HC-based membranes, the acid-content normalized hydration number, λ, of SPAE (27b± 1) and SPPB (31 ± 1) are just 1.5 times greater than N211 (19 ± 1).

Table 3-1. Liquid water uptake, hydration number, and volume fraction of membranes at 70 °C

Membrane	IEC[a] (mmol g^{-1})	L[b] (μm)	ρ[c] (g ml^{-1})	Water Uptake (%)	λ[d]	X_V[e]
SPAE	3.2 ± 0.2	34	1.28	157 ± 5	27 ± 1	0.67 ± 0.03
SPPB	3.2 ± 0.1	33	1.29	180 ± 5	31 ± 1	0.70 ± 0.03
N211	0.91 ± 0.02	33	1.25	31 ± 3	19 ± 1	0.28 ±0.03

[a] ion-exchange capacity as determined in section 2.3.

[b] wet thickness of membranes, measured after being immersed in liquid water at 70 °C.

[c] dry membrane density.

[d] hydration number of membranes after being immersed in liquid water at 70 °C.

[e] volume fraction of water of membranes after being immersed in liquid water at 70 °C.

3.3.2. Mechanical properties

Table 3-2 reports mechanical properties of the membranes SPPB, SPAE, and N211 in an ambient environment (23 ^{o}C, 40% RH). Among the three, membrane N211 possesses the largest elongation at break (148 %), representing N211's most ductile polymer backbone bundles under stress test. Membrane SPPB otherwise shows the least elongation at break (17.5 %) possibly due to its wholly polyaromatic structure making the polymer backbone least ductile.

Table 3-2. Mechanical properties of membranes

Mechanical properties	**SPPB**[a]	**SPAE**[b]	**N211**[a]
Tensile strength (MPa)	59.6 ± 1.4	41.2 ± 1.0	17.3 ± 0.4
Elongation at break (%)	17.5 ± 1.3	57 ± 2	148 ± 4

[a] Values are reported in reference [63].

[b] Mechanical stress tests were conducted by Dr. Hsu-Feng Lee of National Sun Yat-Sen University, Taiwan.

3.3.3. Vapour sorption isotherm and Park model approximation

At 70 °C , changes in mass of membranes under different RH were monitored with DVS and are graphed as water uptake and hydration number against RH in Figure 3-2 and Figure 3-3, respectively. As seen in Figure 3-2, throughout the testing RH range (0-70 %), water uptake of membrane SPPB was the highest, while that of N211 was the lowest. This phenomenon is consistent with the order of liquid water sorption of the membranes at 70 °C, SPPB > SPAE > N211, as shown in Table 3-1.

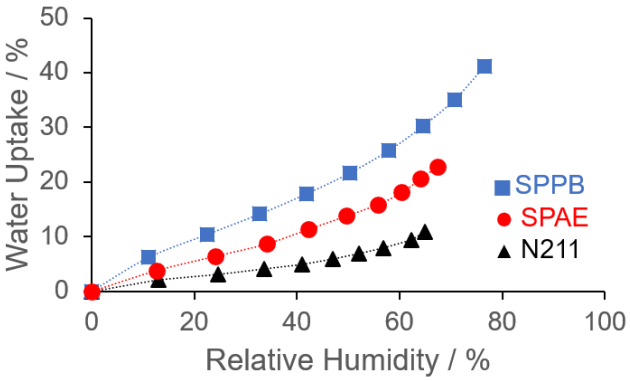

Figure 3-2. Sorption isotherm of sulfonated phenylated polyphenylene biphenyl (SPPB), sulfonated poly(arylene ether) (SPAE), and Nafion (N211) at 70 °C with y-axis expressed as water uptake (%).

The hydration number (λ), describing the average number of water molecules around each sulfonic group, is more extensively used than the mass-based parameters like water uptake to avoid limitations of the latter.[124,222] Figure 3-3 shows λ as a function of relative humidity for each polymer examined. Given the observation of typical sigmoidal isotherm sorption pattern for each membrane, the Park model was employed. Approximation values (± limits of 95% confidence) were determined by least-square-fitting analysis, as shown in Table 3-3. The homoscedasticity observed in the residual distribution in Appendix A and the relatively small error in Table 3-3 confirm the precision in the Park model approximation. Parameter sensitivity analysis was conducted on the Park model regression for membrane SPAE (see Table A 1 and Figure A 1). The least sum of squared residuals (SSR) is sensitive to the variance (±10% and 20%) in a_L, K_L, n, *and* K_A from the approximated values as listed in Table 3-3.

In Figure 3-3, Langmuir-type sorption is the major contributor of water sorption increase in the low RH regime, attributed to sorption of the first monolayer of water molecules at the surface of the membrane. Given the diameter of water molecule as 0.27 nm and surface area of the smooth membrane as 4 cm^2 (2 cm^2 each side), a monolayer of water molecules at the membrane surface would be 9.1×10^{-9} mol or 0.16 µg of water, which is not measurable with the DVS machine's precision at ±0.1 µg. However, the membrane surface is not smooth, especially at this microscopic scale. The actual surface area of the membrane to accommodate the monolayer of water would be much larger than 4 cm^2. Therefore, the mass of the monolayer of water at the membrane surface would be

much larger than 0.16 μg and is measurable by the DVS machine. Langmuir-type sorption depends on the specific site capacity (a_L) and affinity constant (K_L) according to Equation 1-5 in section 1.3.2.[124,129] The specific site capacity shows the concentration of surficial, active Langmuir sites interacting with and fastening water molecules onto the membrane surface. The value of a_L is related to the density of hydrophilic moieties on the membrane surface.[129,131] As shown in Table 3-3, the values of a_L for N211 and SPPB are 6.67 and 7.34, respectively, both lower than that of SPAE, 9.14. This observation implies a higher surficial density of hydrophilic moieties on the SPAE membrane.[128,129,131] Meanwhile, the affinity constant, K_L, for N211 (1.84) is higher than both hydrocarbon-based membranes SPPB (1.19) and SPAE (0.58). The affinity constant describes the extent of water molecules being anchored by ionic domains at the membrane surface.[29] The value of K_L heavily relies on the formation of H-bonds between sulfonic acid groups and water molecules, which successively is related to the acidity strength of the surficial sulfonic group.[124,131] The larger the value of K_L means the more acidic the surficial sulfonic group is. The highest value of K_L in membrane N211 (1.84) agrees with that membrane N211's the pendant perfluorosulfonic acid group is more acidic than both the SPAE's and SPPB's pendant aromatic sulfonic acid group.[57] Also in the low RH regime, no obvious difference in hydration number is seen between N211 and SPPB. This could be attributed to the slightly higher specific site capacity of SPPB (7.34) is trade off by its lower affinity constant (1.39) when compared to N211.

Henry-type sorption assumes a linear relationship between water sorption and relative humidity. Henry-type sorption describes water molecules penetrating through the membrane by interacting with sulfonic acid groups, as depicted in Figure 1-6. Henry's law coefficient, K_H, represents the degree of interactions between water and ionic groups within the bulk membrane,[128] and therefore relies on IEC, the concentration of ionic, sulfonic acid groups within the bulk membrane. As shown in Table 3-3, the K_H for N211, 6.39×10^{-4}, is lower than both SPAE and SPPB, 6.72×10^{-4} and 6.74×10^{-4}, respectively. This observation agrees with the noticeable differences in IEC between PFSA and the hydrocarbon membranes (see Table 3-1).

In Figure 3-3, clustering-type sorption boosts the water content within the membrane and leads to a sharp increase in water sorption in the high-RH regime. The clustering-type sorption envisions the formation of water aggregates that would plasticize the polymer.[127–129,131] Incoming water molecules enlarges the ionic domains, which

subsequently increases the mechanical stress of polymer backbone and results in multi-scale swelling.[124,127] Clustering-type sorption is featured by two coefficients, the aggregate number, n, and the aggregation equilibrium constant, K_A, as seen in Equation 1-7. The aggregate number represents the relative size of the water clusters and is determined by the backbone's flexibility to accommodate incoming water molecules, while the equilibrium constant shows the degree of water clustering formation, which is affected by the backbone's affinity for water molecules.[127–129,131] In the high-RH regime (after 50% RH), obviously higher hydration number is observed in N211 than SPPB. The concave curve of the membrane N211 is more substantial than in the hydrocarbon membranes, represented by higher values of both n (5) and K_A (5.32). This agrees with that N211 possesses a more flexible polymer backbone (also tested in section 3.3.2 by mechanical tests),[57] and its more strongly acidic sulfonic acid groups.[193]

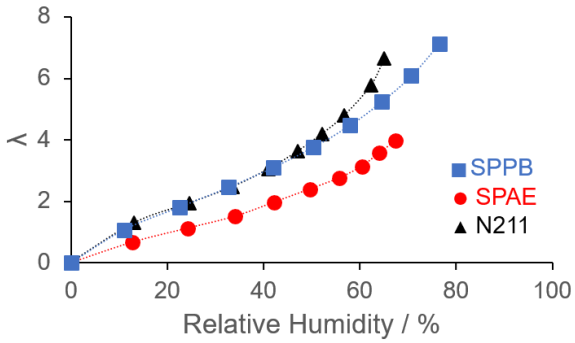

Figure 3-3. Vapor sorption isotherm of sulfonated polyphenylene (SPPB), sulfonated polyarylene ether (SPAE), and Nafion (N211) at 70 °C with y-axis expressed as hydration number (λ). Dotted lines were fitted to Park model.

Table 3-3. Values (± limits of 95% confidence) of parameters in Park model of vapor sorption as expressed in Figure 3-3. Residual distribution is provided in Appendix A.

parameters	N211	SPAE	SPPB
a_L	6.67±0.13	9.14±0.65	7.34±0.05

K_L	1.84±0.18	0.58±0.08	1.39±0.05
K_H (× 10^4)	6.39±0.15	6.72±0.21	6.74±0.05
n	5±0	5±1	4±0
K_A	5.32±0.22	1.98±0.21	2.34±0.04
R^2	0.99	0.99	0.99

3.3.4. Steady-state permeation

As seen in Figure 3-4a, molar water fluxes through each membrane (33 μm wet thickness) were plotted against RH of water vapor under 70 °C for liquid-vapor permeation measurement. LVP was conducted with one side of the membrane sample exposed to water vapor, while the other facing liquid water, as shown in Figure 3-4a. For all membranes, molar water fluxes decreased with the increasing RH of water vapor. This is expected as the driving force, chemical potential difference between the two sides of the membrane, decreased with the increasing RH of water vapor. Then, relative humidity in Figure 3-4a was converted to the driving force, chemical potential gradient, as the x-axis as seen in Figure 3-4b. Water permeance ($mol^2\ m^{-2}\ s^{-1}\ kJ^{-1}$), slope of the linear regression, of each membrane was derived and listed in Table 3-4. For membrane N211, the LVP permeance in this study, 0.048 $mol^2\ m^{-2}\ s^{-1}\ kJ^{-1}$, agrees well with the reported values.[82,172] As shown in Figure 3-4b, the LVP permeance of the three membranes with identical wet thickness are in the order: SPPB > SPAE > N211 (0.075 vs. 0.067 vs. 0.048 $mol^2\ m^{-2}\ s^{-1}\ kJ^{-1}$, respectively).

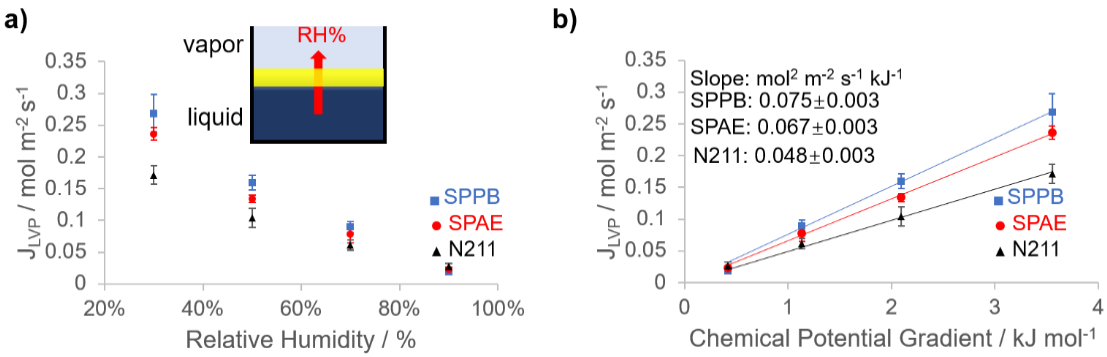

Figure 3-4. Liquid-vapor water permeation of SPAE and N211 with the same thickness (33 μm) as a function of: a) relative humidity of the water vapor side; b) chemical potential gradient at 70 °C for 3 replicates.

As shown in Figure 3-5a, molar water fluxes through each membrane (33 μm wet thickness) were plotted against applied hydraulic pressure for liquid-liquid permeation. For all membranes, LLP water fluxes increased with the increasing differential pressure between the two membrane faces. Again, this is due to the increase in driving force, the chemical potential difference of water between the two sides of the membrane, increased with the increasing pressure applied. Therefore, the external pressure was replaced with chemical potential gradient of water to unify the driving force parameter in both LVP and LLP, as well as to compare the permeances among the three membranes. LLP water permeance (mol^2 m^{-2} s^{-1} kJ^{-1}), slope of the linear regression, of each membrane was derived and listed in Table 3-4. For membrane N211, the LLP water permeance in this study (20.5 mol^2 m^{-2} s^{-2} kJ^{-1})is consistent with reported values.[82,172] As shown in Figure 3-5b, LLP water permeance of the three membranes with identical thickness are in the order SPPB > N211 > SPAE (23.2, 20.5, and 8.5 mol^2 m^{-2} s^{-1} kJ^{-1}, respectively). This order of LLP water permeance is different from the aforementioned order in LVP water permeance that membrane SPAE possesses a higher water permeance than N211 (see Table 3-4). Thus, further inspection was essential (see section 3.3.5) to explain the difference in the two orders of magnitude of water permeances in LVP and LLP experimental setups.

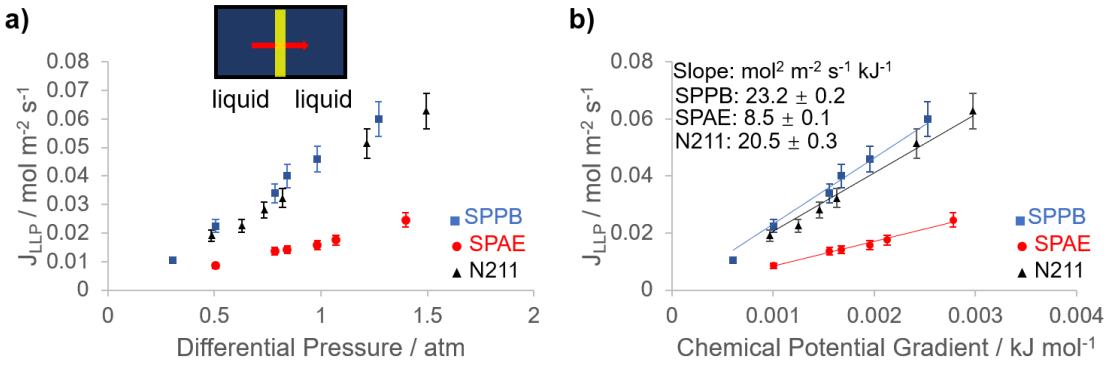

Figure 3-5. Liquid-liquid water permeation of SPAE and N211 with the same thickness (33 μm) as a function of a) differential pressure and b) chemical potential gradient at 70 °C.

Table 3-4. Summary of water permeance in liquid-vapor permeation and liquid-liquid permeation at 70 °C

membrane	LVP permeance (mol^2 m^{-2} s^{-1} kJ^{-1})	LLP permeance (mol^2 m^{-2} s^{-1} kJ^{-1})
SPAE	0.067 ± 0.003	8.5 ± 0.1
SPPB	0.075 ± 0.003	23.2 ± 0.2
N211	0.048 ± 0.003	20.5 ± 0.3

3.3.5. Membrane/vapour interfacial resistance

The obvious discrepancy that membrane SPAE possesses a higher LVP water permeance but a lower LLP water permeance versus membrane N211 with identical thickness can be attributed to SPAE's possibly lower gas/membrane interfacial resistance. Former studies have found that the LVP process can be divided into 3 separate steps: adsorption, internal water transport, and desorption.[29,196] The interfacial resistance of vapor/membrane is large for membrane N211, due to the parallel-micelle morphology at the Nafion® membrane surface.[148,150] The liquid/membrane interfacial resistance is,

however, negligible.[82,163–165,172,197] Therefore, in the case of LLP, internal water transport is rate determining while in the case of LVP, the vapor/membrane interfacial resistance becomes important.

To determine the vapor/membrane interfacial resistance, LVP measurements were executed for each membrane of different thicknesses, with one side facing water vapor at different relative humidities at 70 °C. Molar water flux through each membrane was monitored, subsequently resistance was calculated according to Equation 2-12 and plotted against corresponding wet thickness as shown in Figure 3-6. In Figure 3-6, the intercept at y-axis of the linear regression is the interfacial resistance while the slope is the thickness-independent internal resistance coefficient. [29,163,172] The interfacial resistance and internal resistance coefficient of SPAE and SPPB in liquid-vapor permeation under each relative humidity of water vapor are provided in Table 3-5. The LVP resistances of both membrane SPPB and SPAE under different relative humidity are plotted in Figure 3-6. The internal resistance coefficients, defined as the slope, for both membranes decrease as water vapor RH increases. The decrease is observed because of the increasing water content within the membrane that facilitates water transport.[163] Meanwhile, the interfacial resistance, for both membranes, decreases with water activity possibly due to the reorganization of the surface morphology that favors the ingress and egress of water under higher RH, as previously reported for Nafion.[157] When comparing membrane SPAE and SPPB, the internal resistance coefficient of SPAE was higher than SPPB, although the interfacial resistance of SPAE was smaller than that of SPPB throughout the relative humidity range (see Table 3-5). The larger internal resistance coefficient of membrane SPAE is the main factor responsible for the lower LLP water permeance of SPAE when compared to SPPB.

Table 3-5. Internal resistance coefficient and interfacial resistance of SPPB and SPAE membranes in liquid-vapor permeation at 70 °C.

Relative Humidity	SPPB		SPAE	
	Slope ($\times 10^{-6}$ kJ m s mol^{-2})	Y-intercept (kJ m^2 s mol^{-2})	Slope ($\times 10^{-6}$ kJ m s mol^{-2})	Y-intercept (kJ m^2 s mol^{-2})
30%	0.040 ± 0.001	11.5 ± 0.4	0.36 ± 0.01	2.0 ± 0.2
50%	0.036 ± 0.001	10.6 ± 0.6	0.32 ± 0.01	1.0 ± 0.1
70%	0.035 ± 0.001	9.5 ± 0.6	0.26 ± 0.01	0.56 ± 0.04
90%	0.032 ± 0.001	9.0 ± 0.7	0.19± 0.02	0.35 ± 0.05

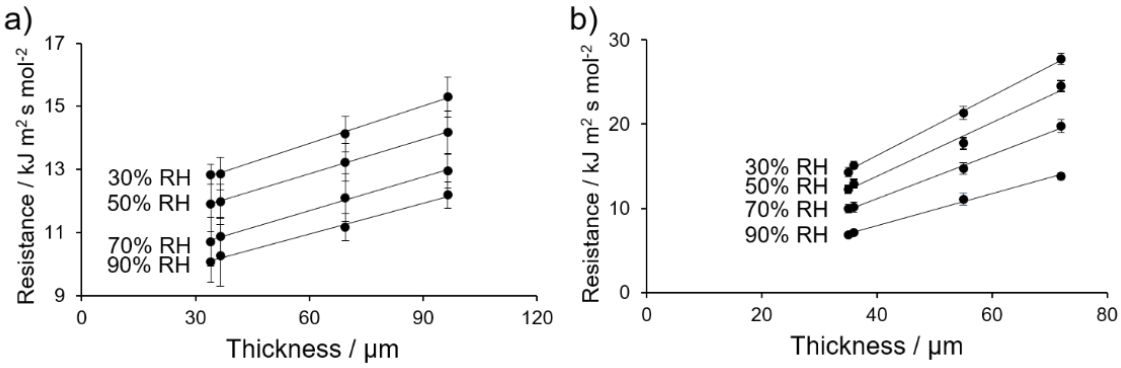

Figure 3-6. Resistance of liquid-vapor permeation through a) SPPB and b) SPAE membranes with one side exposed to water vapor of different relative humidities as a function of wet membrane thickness at 70 °C. For each membrane, of each different wet thickness, there were 3 replicates. The slope of the linear regression yields the internal resistance coefficient, while the intercept yields the interfacial resistance.

In Figure 3-7, a more detailed comparison of interfacial resistances among the three membranes in LVP with water vapor regulated at 30% RH is provided. The interfacial resistances of the three membranes are in the order: SPAE < SPPB ≈ N211 (2.03, 11.5, and 11.6 kJ m^2 s mol^{-2}, respectively), while the internal resistance coefficients of three membranes are in the order: SPPB < N211 < SPAE (0.040, 0.084, and 0.36 10^6 kJ m s mol^{-2}, respectively). Here, the interfacial resistance and internal resistance coefficient obtained for membrane N211 agree with the reported values, 11.2 to 12.0 kJ m^2 s mol^{-2} and 0.054 to 0.092 (10^6 kJ m s mol^{-2}) under 30 to 40% RH and 70 °C, respectively.[82,164,165,197] With 95% confidence interval, the interfacial resistance of SPAE (2.0 ± 0.7 kJ m^2 s mol^{-2}) is obviously lower than those of SPPB (11.5 ± 0.6 kJ m^2 s mol^{-2}) and Nafion (11.6 ± 1.2 kJ m^2 s mol^{-2}). The relatively minimal interfacial resistance of membrane SPAE results in the smallest overall resistance (most permeable) in liquid-vapor permeation when the thickness is below ~30 μm. With 95% confidence interval, the internal resistance coefficient of SPPB (0.040 ± 0.004 10^6 kJ m s mol^{-2}) is obviously lower than those of SPAE (0.36 ± 0.03 10^6 kJ m s mol^{-2}) and Nafion (0.084 ± 0.024 10^6 kJ m s mol^{-2}). When the thickness is greater than ~30 μm, membrane SPPB possesses the lowest overall water transport resistance (most permeable) because of its lowest internal resistance coefficient among the three membranes. This phenomenon could be attributed to its larger ion-exchange capacity versus membrane N211. However, IEC alone does not explain the lower internal transport resistance of SPPB compared to SPAE as both membranes share similar IECs (see Table 3-1). It is speculated that internal morphology of SPPB is more favorable for water transport because of the subtle effect of the ether linkage in SPAE that renders the polymer more flexible and which may result in enhanced polymer chain entanglement and potentially increased tortuosity of internal water channels. The stiffer backbone of membrane SPPB is also confirmed by the mechanical stress tests that SPPB possesses a smaller elongation at break (17.5%) than SPAE (57%) as seen in section 3.3.2.

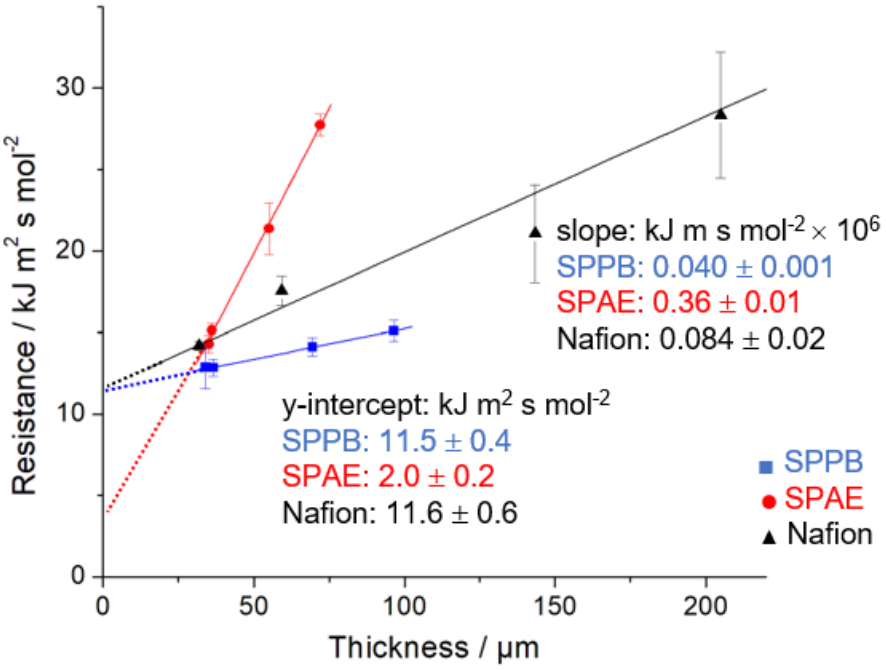

Figure 3-7. Water permeation resistance (average ± standard deviation) in LVP at 70 °C with relative humidity of water vapor controlled at 30%.

3.3.6. Surficial characterization

As aforementioned in section 3.3.5, the interfacial resistance of SPAE is the lowest among the three, possibly because of its more hydrophilic surface. Hence, surficial characterizations were executed. Contact angle measurements, examined on the surface of dry membranes at ambient temperature and RH (22 °C and 40 % RH, respectively), are presented in Figure 3-8. The contact angle of SPAE (88.8°) is smaller than both of SPPB (97.8°) and N211 (98.3°). The contact angle for N211 in this research is consistent with previous studies on Nafion® membranes.[147,148] The hydrophobicity on the N211 surface arises from its fluorine-rich surface.[223] The surficial hydrophobicity of SPPB membranes is likely because of its lower fraction of 'open' ionic domains at the surface, like what was reported for other hydrocarbon-based PEMs.[197]

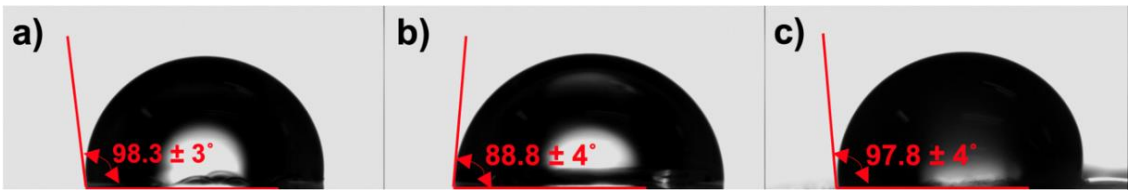

Figure 3-8. Contact angle measurements (10 replicates each) of dry membranes a) N211, b) SPAE, and c) SPPB under at 22 °C and 40% RH.

Also, the surficial features of membranes were tested by conductive AFM. Conductive AFM is essential to image regional distribution of hydrophilic, open proton-conducting channels on surface of PEMs.[157,215] For consistency, identical procedure and machine settings were maintained for all three membranes in conductive AFM measurements. However, no ionic current signal was detected for membrane N211. In Figure 3-9, the bright/dark contrast represents the conductive/insulative or hydrophilic/hydrophobic regions at the membrane surface. The scales display the magnitudes of the surface current signals detected by the conductive AFM for the membranes under identical settings. The focus of this measurement is, however, discovering the hydrophilic and conductive domains on the surface of the membrane by the bright/dark contrast instead of the magnitudes of the current density. As presented in Figure 3-9, at room temperature and RH (22 °C and 40 % RH, respectively), the percentage of active area,[157] on which the surficial current was detected by the conductive AFM, is 32% for SPAE, much higher than that of SPPB (~4 %) and previously reported Nafion 211 under similar circumstances (13.7% at 55% RH).[157] Membrane SPAE's high percentage of hydrophilic area on the surface agrees with the observation in section 3.3.3, that SPAE possesses a higher value for the specific site capacity, a_L (9.14) versus N211 (6.37) and SPPB (7.64).[124,127,129] Similar high percentage of active area on the surface of a membrane has also been reported for another highly sulfonated poly(arylene ether)-based material with similar structure to SPAE.[9] The hydrophilicity of membrane SPAE may be attributed to the random post-functionalization of the polymer, and the presence of the ether group.[224,225]

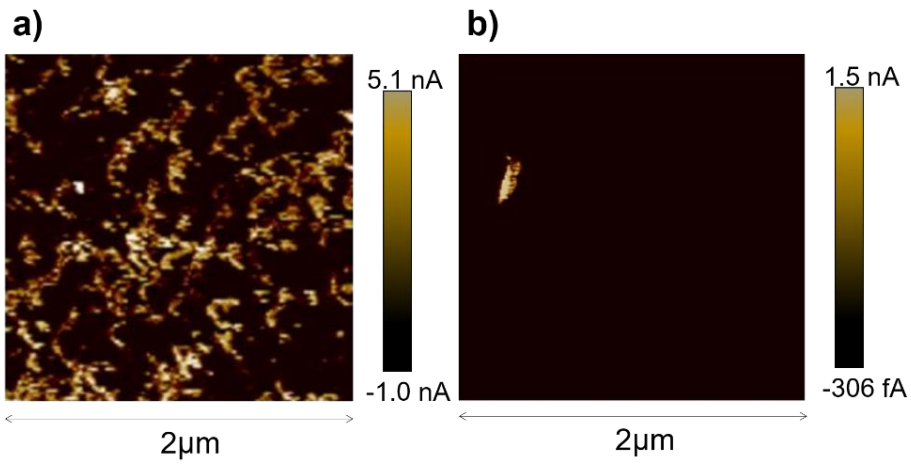

Figure 3-9. Peak-Force Tunneling atomic force microscope current image for a) SPAE and b) SPPB membranes at ambient relative humidity and temperature. With identical procedure and machine settings for both SPAE and SPPB, no signal was detected for membrane N211.

3.4. Conclusion

Sorption isotherm of the second generation sulfonated phenylated poly(phenylene), SPPB, was studied by DVS, interpreted by the Park model, and compared to Nafion reference and the HC-based reference, SPAE. In Langmuir-type sorption, it was found that SPAE possessed the highest surface site capacity, representing a higher surficial hydrophilicity compared to either SPPB or N211. In Henry-type sorption, K_H values for both SPAE and SPPB were higher than N211 due to their larger IEC. In clustering-type sorption, a sharp increase in water sorption was observed for N211 membranes due to a more flexible backbone, and more acidic sulfonic acid groups. The poly(phenylene) SPPB was the most permeable when liquid was on one side and vapor the other, when thickness was > ~30 µm, because it possessed the lowest internal resistance caused by a large IEC and potentially more contiguous internal morphology brought by the wholly aromatic backbone. In stark contrast, when thickness was < ~30 µm, SPAE was the most permeable as it afforded the lowest membrane/vapor interfacial resistance, which was confirmed by contact angle measurements and conductive AFM. The more hydrophilic surface of SPAE might possibly allow the membrane to possess a higher water retention under dry environment, which helps to maintain the performance of a fuel cell under low relative humidity. However, the smaller internal resistance coefficient

of SPPB indicates a faster internal water transport within the bulk membrane when subject to a water concentration bias. Even though these HC-based PEMs swell excessively compared to PFSA membranes, the structure-property relationships found in this study provide valuable insight into water sorption and transport that may assist the design of next generation solid polymer electrolytes for electrochemical energy storage and conversion devices.

Chapter 4. Water transport through architecturally controlled, pyridyl-bearing sulfonated phenylated polyphenylenes: understanding the role of acid-base interactions

The work in this chapter is in part of: S. Xu*, Y. Wu*, M. Adamski, K. Fraser, S. Holdcroft, Understanding the role of acid-base interactions using architecturally-controlled, pyridyl-bearing sulfonated phenylated polyphenylenes, J. Mater. Chem. A. (2020).

* These authors contributed equally to this work

Yang Wu performed all the water vapor sorption, transient diffusion, and steady-state permeation measurements. Shaoyi Xu undertook synthesis and preparation of all proton exchange membranes in this study. Yang Wu and Shaoyi Xu both performed the liquid water sorption and conductivity measurements. Michael Adamski synthesized and prepared the membranes. Kate Fraser performed the density function theory (DFT) calculations. Professor Steven Holdcroft advised and supervised the work conducted.

Due to the large scope of this research, only the part concerning water sorption and transport with necessary background introduction is included in this chapter. Supporting information is provided in Appendix B.

4.1. Introduction

Hydrocarbon-based polymers, functionalized with sulfonic acid groups, often require high sulfonic acid content for a contiguous hydrophilic percolation network of protons and water. High extent of sulfonation causes a high degree of swelling in water that reduces the mechanical integrity. One approach to restrict swelling and improve mechanical properties of the polymers is to incorporate basic *N*-heterocyclic groups. [226,227] The incorporation creates the acid-base interaction. The interaction is between the polymer-bound, pendent sulfonates and polymer-bound, protonated *N*-heterocyclic cations.[226,227] This method has been known to enhance mechanical strength, improve chemical and thermal stability, and reduce swelling and membrane water sorption.[228–231] However, this approach also reduces proton conductivity because the incorporated basic group neutralizes $–SO_3H$ and binds the originally hydrated, mobile proton.[228–231] It is challenging to induce sufficient intermolecular interactions through the acidic-base neutralization, and subsequent mechanical strength enhancement with reduction in swelling, without causing a large fraction of protons bound and immobile. Solution to this challenge would require a range of polymers with varying incorporated base content but similar molecular structure and a systematic study of the acid-base interaction.

Recently, a novel approach was published to adjust the extent of acid-base interactions within the proton-conducting polymer.[232] The approach involves incorporating a sterically-hindered pyridine moiety (triphenylated pyridyl, TPPy, see Figure 4-1) into the sulfonated phenylated poly(phenylene)s (Figure 4-1).[232] Following this initial work, incorporation of various pyridyl analogues of the triphenylated phenyl unit into sulfophenylated polyphenylenes, as shown in Figure 4-1, would yield a unique series of polymers to probe acid-base interactions in PEMs. These polymers with similar molecular structure, varying in acid-base content, facilitate the examination on the effects of replacing a single carbon atom with a basic nitrogen atom in the polymeric repeating unit. This series of polymers also possess the added novelty of introducing steric hindrance into selected basic sites, which is an unexplored area in the field of proton exchange membranes.

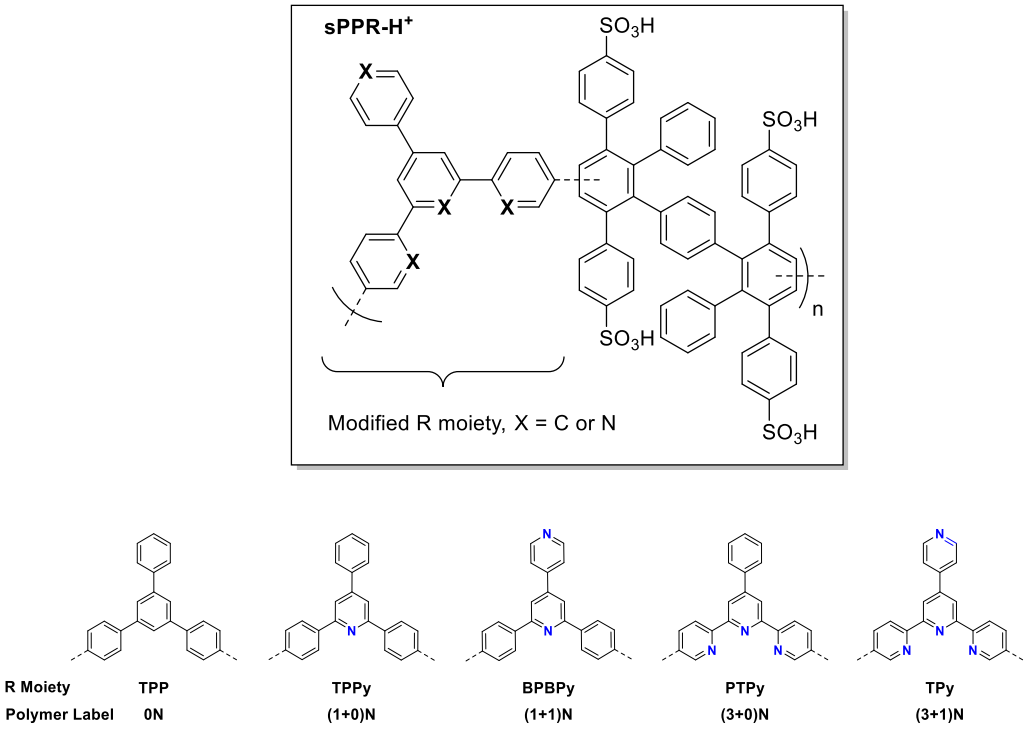

Figure 4-1. Sulfonated phenylated poly(phenylene)s (SPPR) containing varying R moieties: triphenylated phenyl (TPP), triphenylated pyridyl (TPPy), biphenylated bipyridyl (BPBPy), phenylated tripridyl (PTPy), and tetrapyridyl (TPy) moieties. Numerical label is written to distinguish the nitrogen atoms incorporated internally or externally to the ring.

Therefore, properties of the series of sulfonated phenylated polyphenylenes containing an increasing number of N-atoms within the repeat unit are examined and reported (see Figure 4-1). These are sulfonated phenylated polyphenylenes (sPP) containing the following linkages: triphenylated phenyl (sTPPPP); triphenylated pyridyl (sTPPyPP); biphenylated bipyridyl (sBPBPyPP); phenylated tripridyl (sPTPyPP), and; tetrapyridyl (sTPyPP). They are also abbreviated as 0N-H^+, (1+0)N-H^+, (1+1)N-H^+, (3+0)N-H^+, and; (3+1)N-H^+, respectively, in which number of internally-positioned pyridyl groups is distinguished from the externally-positioned. For example, (3+1)N-H^+ contains 3 internally-positioned pyridyl groups (terpyridine) and 1 externally-positioned pyridyl. The physicochemical properties of the sulfonated phenylated polyphenylenes were systematically evaluated and compared. Comparisons were carried out in two areas: (1) Water sorption and mass transport properties for the fully hydrated membranes; and (2) Water sorption and mass transport properties for the partially hydrated membranes,

namely vapour sorption, transient diffusion, and steady-state water permeation, the background of which are provided below.

Dynamic vapor sorption (DVS) analyzer was used to monitor the changes in mass of samples exposed to water vapor under different relative humidities. DVS also allowed quantification of the transient water diffusion in membranes following a change in relative humidity. An abundance of reports of sorption isotherms and transient diffusion measurements of PEMs exist, but these focus on perfluorosulfonic acid ionomer membranes.[29] There are no reports on transient water diffusion for PEMs that incorporate acid-base interactions.

Steady-state water permeation through a proton exchange membrane, i.e., the rate of water transport through a membrane, is a critical parameter for many electrochemical devices. Steady-state water permeation through PFSA-based membranes have been extensively investigated,[18,29,163–165,197,200,233,234] but only a few experimental studies of water permeation through HC-based PEMs have been reported.[197] There are no reports on steady-state water permeation through PEMs that incorporate acid-base interactions. In response, this chapter reports water permeation under two scenarios: mass transport through fully hydrated membranes, and through membranes exposed to liquid water on one side and water vapour on the other, as these scenarios are often found in aqueous-based electrochemical devices incorporating solid polymer electrolytes.

The result of this study, drawn from a series of proton conducting, sulfonated polymers that possess the same theoretical IEC and molecular architecture, but for which the acid-neutralizing N-content is systematically increased with precise placement of the N-atoms, allow for structure-property relationships of acid-base polymers to be explored with unprecedented molecular control.

4.2. Experimental

4.2.1. Materials

Detailed information on the deionized water (Milli-pore water), commercial Nafion® membranes are given in section 2.2, chapter 2.

4.2.2. Experimental techniques

Sorption isotherm, liquid-vapour permeation, liquid-liquid permeation, transient diffusion, and proton conductivity measurement are described in detail in chapter 2. Sorption isotherm, LVP, and LLP measurement were run at 80 °C. Also, detailed instruction on permeability, and resistance determination are provided in chapter 2.

Due to the limited accessibility of membranes with identical thickness, the steady-state permeance (p, mol m^{-1} s^{-1}) was defined as the product of molar water flux (J, mol m^{-2} s^{-1}) and wet thickness of membranes (L, m).

4.3. Results and discussion

4.3.1. Mechanical analysis of membranes[2]

Stress-strain data for 0N-H^+, (1+0)N-H^+, (1+1)N-H^+, and (3+1)N-H^+ membranes can be found in Table 4-1. When four N-atoms are introduced into the sulfonated polyphenylenes, the (3+1)N-H^+ membranes become stronger (tensile strength = 44.9 ± 0.4 MPa) but less flexible (elongation at break = 7.2 ± 0.1%), compared to (1+0)N-H^+ (43.3 MPa, 55.5 %, respectively). Intermolecular interactions likely dominate in (1+1)N-H^+, (3+0)N-H^+ and (3+1)N-H^+ polymers. Intermolecular crosslinking of polymers represents the proton of one polymer chain is bound to or may be shared with the pyridine group of another polymer chain. Intermolecular crosslinking often increases the interactions between polymer chains and inhibits the movement of them. Enhanced tensile strength and reduced elongation at break is therefore often observed in polymers with intermolecular crosslinking.[235] In contrast, compared to 0N-H^+, (1+0)N-H^+ is more flexible and of lower tensile strength. This change may be attributed to reduced intermolecular interactions,[235] because the steric hindrance about the centered pyridine may limit or prevent the acid-base interaction between the pyridine lone pair and $–SO_3H$ proton on other polymer chains. In comparison, the additional pyridine groups contained in the (1+1)N-H^+ and (3+1)N-H^+ polymers are more “exposed”, as they do not possess flanking phenyl moieties to provide steric hindrance. Thus, intermolecular crosslinking between the pyridine and $–SO_3H$ groups is expected to play a dominant role in (1+1)N-H^+,

[2] Mechanical strength analysis of membranes was mainly carried out by Dr. Shaoyi Xu.

and (3+1)N-H^+, especially since the externally-exposed pyridines to be fully protonated and the resultant pyridiniums more effective as acid-base crosslinking sites. These membranes exhibit an expected reduction in elongation at break compared to (1+0)N-H^+ membranes. (3+0)N-H^+ deserves special mention as these particular membranes are exceptionally brittle and characterization of this membrane type is limited. The precise reason for this is not yet understood but it lies in the fact that the terpyridium site is multi-protonated and hence subject to localized acid-base crosslinking, without the added advantage of possessing an externally-exposed pyridine that would preferably be protonated like (3+1)N-H^+, which is film forming.

Table 4-1. Mechanical properties[a] of polymers measured under ambient conditions.

Ionomers	**0N-H^+**	**(1+0)N-H^+**	**(1+1)N-H^+**	**(3+0)N-H^+**	**(3+1)N-H^+**
Tensile strength (MPa)	54.8 ± 1.9	43.3 ± 1.1	19.9 ± 0.1	N/A	44.9 ± 0.4
Elongation at break (%)	36.8 ± 1.7	55.5 ± 3.1	3.8 ± 0.1	N/A	7.2 ± 0.1
Young's modulus (MPa)	584 ± 82	402 ± 24	700 ± 1	N/A	793 ± 48
Mechanical class	strong and tough	strong and tough	strong and brittle	brittle	strong and brittle

[a] Mechanical analysis were performed under ambient conditions (23 ^oC, 50% RH)

4.3.2. Fully hydrated membranes: liquid water sorption

Liquid water sorption measurements were executed on membranes by immersing them in Millipore water at 30 ^oC until constant mass had been achieved. Liquid sorption data are summarized in Table 4-2and plotted in Figure 4-2. Dimensional swelling of the hydrocarbon-based PEMs decrease with the increasing of the number of incorporated N atoms: 0N-H^+ (82 ± 3 vol%) > (1+0)N-H^+ (62 ± 2 vol%) > (1+1)N-H^+ (56 ± 6 vol%) > (3+1)N-H^+ (20 ± 2 vol%). This result confirms the success at restricting dimensional swelling via

addition of basic pyridyl groups into the polymer to abate the effective concentration of sulfonic acid groups within the membrane.

Table 4-2. Liquid water sorption of membranes at 30 ºC: Liquid water uptake (WU_{liquid}), hydration number (λ), dimensional swelling (DS), and water volume fraction (Xv).

Membrane	IEC_{exp} (mmol g^{-1})[a]	WU_{liquid} (%)[b]	λ[c]	DS (%)[d]	X_v(water)[e]
0N-H$^+$	2.90 ± 0.04	80 ± 3	15.3 ± 0.5	82 ± 3	0.83 ± 0.03
(1+0)N-H$^+$	1.98 ± 0.08	54.4 ± 0.7	15.2 ± 0.1	62 ± 2	0.64 ± 0.03
(1+1)N-H$^+$	1.80 ± 0.20	52 ± 3	16.0 ± 0.5	56 ± 6	0.58 ± 0.05
(3+0)N-H$^+$	1.58 ± 0.04	N/A	N/A	N/A	N/A
(3+1)N-H$^+$	1.38 ± 0.14	49 ± 3	20 ± 1	20 ± 2	0.51 ± 0.03
N211	0.9 ± 0.1	37 ± 3	22.8 ± 0.3	24 ± 2	0.36 ± 0.03

[a] based on experimental acid-base titration.
[b] liquid water uptake at 30 ºC.
[c] based on the experimental IEC.
[d] x-axis (thickness) swelling in dimensional swelling.
[e] water volume fraction at 30 ºC.

As see in Figure 4-2, water volume fraction (Xv) of the membranes is proportional to the experimentally-determined IEC values of the membranes. Among the four hydrocarbon-based membranes, 0N-H$^+$ possesses the highest IEC, 2.90 ± 0.04 mmol g^{-1}, as well as the highest WU_{liquid} (79.8 ± 2.6%) and Xv (0.83 ± 0.03). The (3+1)N-H$^+$ membrane with the lowest IEC, 1.38 ± 0.14 mmol g^{-1}, shows the lowest liquid water uptake (49 ± 3%) and smallest water volume fraction (0.51 ± 0.03). As more N-atoms are incorporated into the polymer, the number of free protons decreases and the number of ionic crosslinks increases, both of which contribute to a lower water uptake. The hydration numbers, λ of the polymers are similar (15-16), with the exception of (3+1)N-H$^+$, which shows a slightly higher value, as seen in Table 4-2. λ values, while included for comparison, should be treated with caution in these polymers with both acidic and basic functional

groups because their calculation excludes water molecules that may be associated with hydrophilic protonated pyridyl-sulfonic acid complexes.

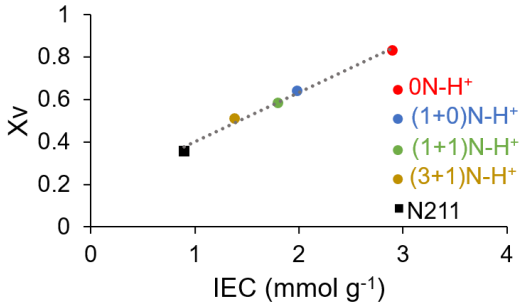

Figure 4-2. Correlations between ion exchange capacity and liquid water volume fraction at 30 ºC, respectively, of 0N-H$^+$, (1+0)N-H$^+$, (1+1)N-H$^+$, (3+1)N-H$^+$, and N211 polymeric membranes.

4.3.3. Steady-state liquid-liquid permeation

The thickness-normalized water permeance of each fully-hydrated membrane was calculated and plotted against the differential pressure and chemical potential gradient of water between the two sides of the membrane at 80 °C in Figure 4-3a and Figure 4-3b, respectively. Water permeance of each membrane increases linearly with the increasing differential pressure (chemical potential gradient). Permeability, the slope of water permeance against chemical potential gradient, decreases with the increasing number of pyridyl moieties in the polymeric repeat unit (see Table 4-3): 0N-H$^+$ > (1+0)N-H$^+$ > (1+1)N-H$^+$ > (3+1)N-H$^+$ and is correlated with the water volume fraction as shown in Figure 4-4. This observance is consistent with the increasing acid-base interactions within the polymer, a reduction of free protons, an increase in ionic crosslinking, and a reduction in the percolation network for water transport.[57,232] For reference, water permeability of N211 is shown in Table 4-3 to be 1.00×10^{-3} mol^2 m^{-2} s^{-1} kJ^{-1} and similar to previously reported values.[163–165,172] Of the hydrocarbon-based membranes, the permeability of (3+1)N-H$^+$ is statistically identical to that of N211.

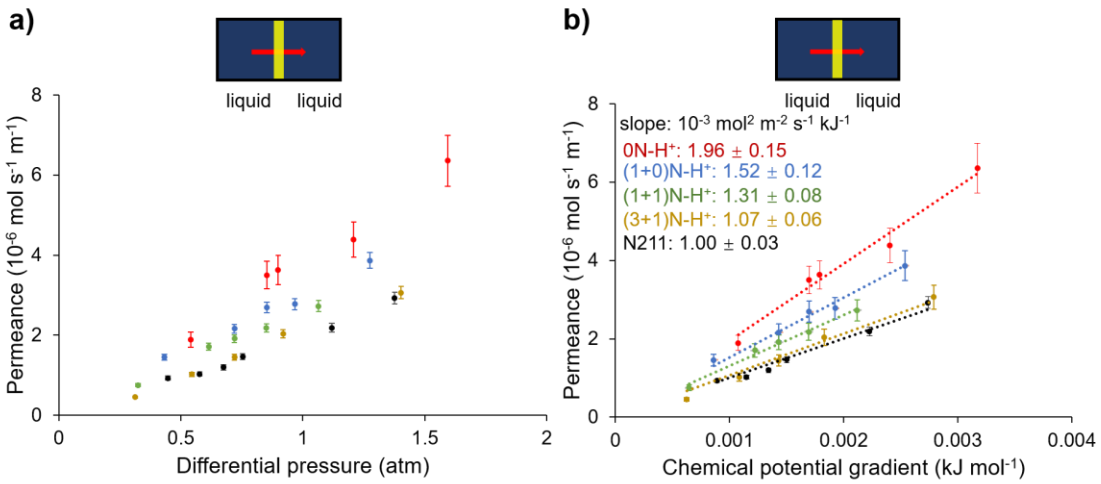

Figure 4-3. Steady-state liquid-liquid permeation plotted against a) the differential pressure and b) chemical potential gradient at 80 ºC.

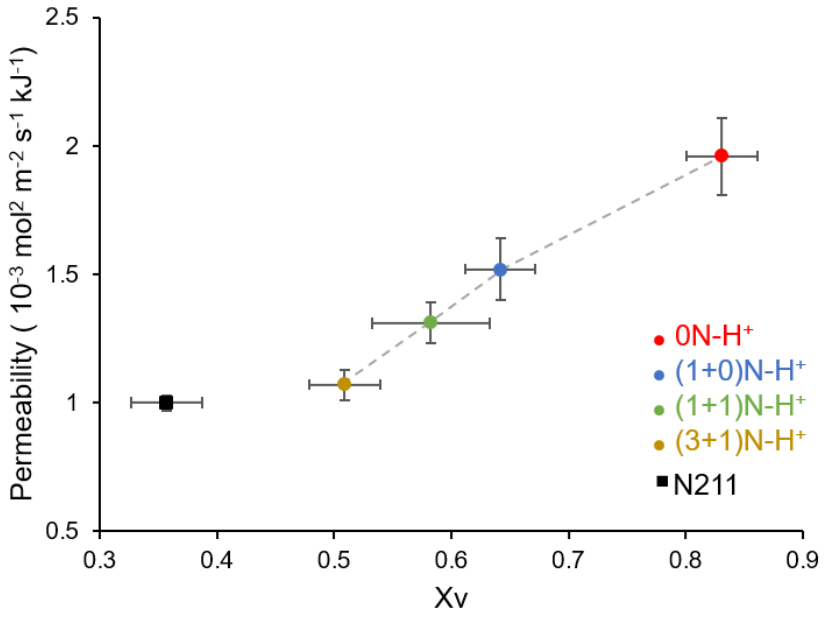

Figure 4-4. Liquid-liquid permeability of fully hydrated membranes at 80 °C as a function of water volume fraction, Xv.

Table 4-3. **Liquid-liquid permeability of membranes at 80 ºC**

membrane	LLP permeability ($\times 10^3$ mol^2 m^{-2} s^{-1} kJ^{-1})
0N-H$^+$	1.96 ± 0.15
(1+0)N-H$^+$	1.52 ± 0.12
(1+1)N-H$^+$	1.31 ± 0.08
(3+0)N-H$^+$	N/A
(3+1)N-H$^+$	1.07 ± 0.06
N211	1.00 ± 0.03

4.3.4. Proton conductivity in fully hydrated state

Proton conductivities of the 0N-H$^+$, (1+0)N-H$^+$, (1+1)N-H$^+$ and (3+1)N-H$^+$ membranes were measured at 30 ºC when fully hydrated in liquid water. Conductivities and effective mobilities of fully hydrated membranes are plotted in Figure 4-5 and summarized in Table 4-4.

Table 4-4. Proton conductivity (σ), experimental acid concentration [H$^+$], effective mobility (μ) and water volume fraction (Xv) of fully hydrated membranes at 30 ºC.

Membrane	σ (mS cm^{-1})	[H$^+$] (mol L^{-1})	μ (10^{-3} cm^2 s^{-1} V^{-1})	Xv
0N-H$^+$	210 ± 10	3.0 ± 0.1	0.72 ± 0.03	0.83 ± 0.03
(1+0)N-H$^+$	150 ± 10	2.3 ± 0.2	0.68 ± 0.03	0.64 ± 0.03
(1+1)N-H$^+$	110 ± 10	2.0 ± 0.1	0.56 ± 0.03	0.58 ± 0.05
(3+0)N-H$^+$	N/A	N/A	N/A	N/A
(3+1)N-H$^+$	78 ± 3	1.4 ± 0.1	0.58 ± 0.03	0.51 ± 0.03
N211	95 ± 3	1.0 ± 0.1	0.93 ± 0.04	0.36 ± 0.03

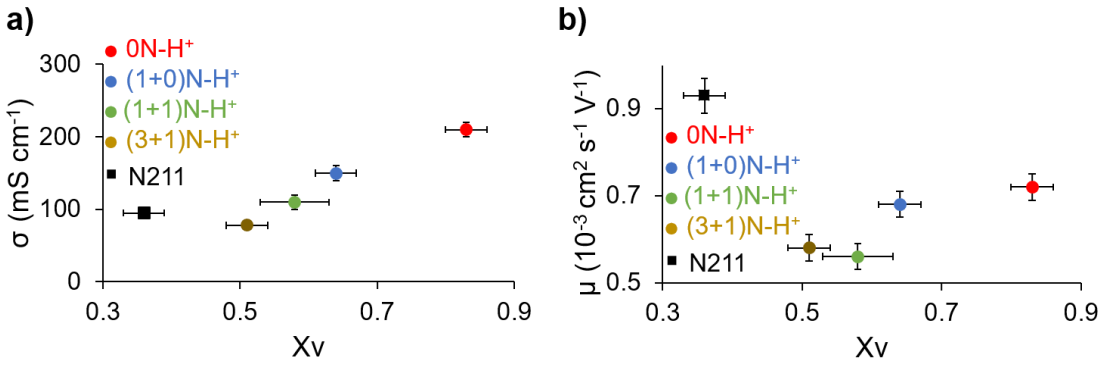

Figure 4-5. (a) in-plane conductivity vs Xv of fully hydrated membranes at 30 ºC; (b) effective proton mobility vs Xv of fully hydrated membranes at 30 ºC.

To gain insights to proton conduction in fully hydrated state, proton conductivity against water volume fraction was plotted in Figure 4-5a. The conductivity shows an increasing trend as Xv increases. 0N-H$^+$ exhibits the highest conductivity (210 mS cm^{-1}) and water volume fraction (0.83) among the four polymers. Although (3+1)N-H$^+$ membrane shows the lowest Xv (0.51), it still is higher than N211 (0.36). Sufficient water content is beneficial to acid dissociation for proton mobility among HC-based polymers. Thus, it can be inferred that the high Xv of (3+1)N-H$^+$ contributes to efficient proton conducting behavior.

The effective proton mobility, μ, is plotted against water content in Figure 4-5b. Notably, the effective proton mobility of membrane (1+1)N-H$^+$ and (3+1)N-H$^+$ are similar (0.56 ×10^{-3} cm^2 s^{-1} V^{-1} vs 0.58×10^{-3} cm^2 s^{-1} V^{-1}, respectively), both of which are lower than those of (1+0)N-H$^+$ and 0N-H$^+$ (0.68 ×10^{-3} cm^2 s^{-1} V^{-1} vs 0.72×10^{-3} cm^2 s^{-1} V^{-1}, respectively). This difference in mobility occurs as a result of the incorporation of an exposed pyridine which readily interact with sulfonic acid groups, promoting the intermolecular crosslinking and possibly increasing the tortuosity of conducting channels. The obviously higher effective proton mobility of N211 (0.93 ×10^{-3} cm^2 s^{-1} V^{-1}) than the HC-based membranes is not unexpected due to the Nafion's more contiguous morphology as a PFSA membrane, which facilitates proton transport.

4.3.5. Water vapour sorption isotherm

As some electrochemical applications (e.g., proton exchange membrane fuel cell) require exposure of solid polymer electrolytes to water vapour, not liquid water, water vapor uptake values (WU_{vapor}) of each membrane exposed to water vapour were recorded at 80 °C under varied RH values. Measurements were conducted both sorption (0 to 70% RH) and then desorption (70 to 0% RH). Water vapor uptake decreases substantially with the increasing number of N-atoms in the polymers as shown in Figure 4-6, which is consistent with water contents found for fully hydrated membranes. Water vapor uptake of each membrane during desorption is observed to be higher than that during sorption, resulting in a measurable hysteresis. This hysteresis is more pronounced in 0N-H^+ and (1+0)N-H^+ membranes. Hysteresis often stems from surface reorganization of the membrane.[29] Under dry environments, dehydration at the surface retards water loss, leading to higher water contents for a particular RH when RH decreases. In Nafion®, for example, water conducting domains of polymers tend to align parallel to the surface, minimizing water transport and preventing water loss.[148] Hence, the hysteresis area predicts, qualitatively, the extent of morphological reorganization at the surface of a membrane. In this context, reorganization of dehydration of the membrane's surface is more prominent for 0N-H^+ and (1+0)N-H^+ membranes than for (1+1)N-H^+ and (3+1)N-H^+ membranes. Also, it has previously been reported that there is a more distinctive water-clustering region, therefore higher likelihood of morphological rearrangement, in 0N-H^+ than (1+0)N-H^+, as evidenced by small-angle X-ray scattering experiments.[232] The notably reduced hysteresis in (1+1)N-H^+ and (3+1)N-H^+ membranes is possibly a result of the intermolecular ionic crosslinking which decreases flexibility of the constituent polymer chains.[235]

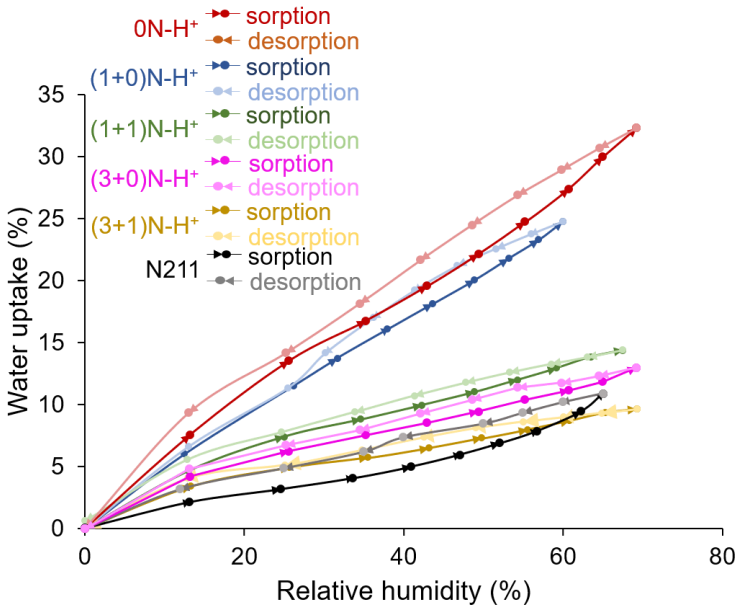

Figure 4-6. Sorption isotherm of 0N, (1+0)N-H$^+$, (1+1)N-H$^+$, (3+0)N-H$^+$, (3+1)N-H$^+$, and N211 polymer membranes at 80 ^{o}C during adsorption (0 – 70% RH) and then desorption (70 – 0% RH) relative humidity cycles.

Shown in Figure 4-7 are plots of hydration number vs RH. Typical sigmoidal sorption isotherm patterns are observed for all five membranes. The Park model was applied to deconvolute dynamic vapor sorption. Approximation values of the Park model coefficients for each membrane are summarized in Table 4-5. According to the Park model,[124,127–130] typical sorption isotherms consist of three separate, independent processes: Langmuir, Henry, and clustering-type sorption.

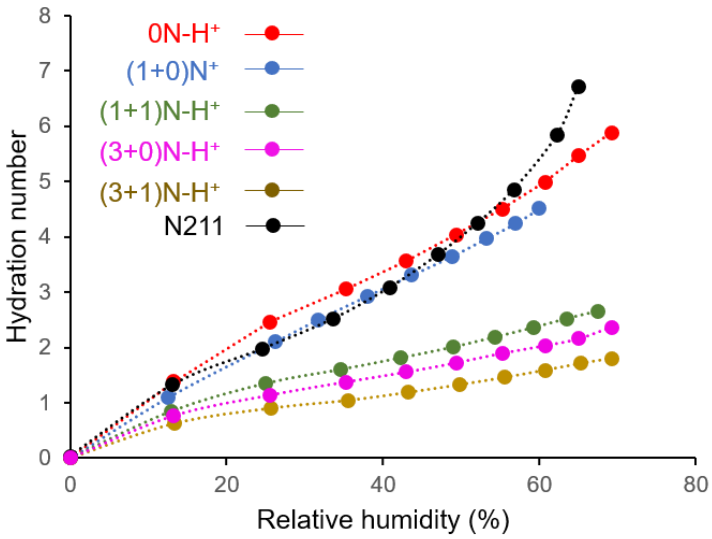

Figure 4-7. Water vapor sorption isothem of membranes at 80 ºC expressed as hydration number. The dotted lines represent a data fit to the Park model.

Table 4-5. Value of variables (± limits of 95% confidence) in Park model expressed in hydration number

	0N-H⁺	**(1+0)N-H⁺**	**(1+1)N-H⁺**	**(3+0)N-H⁺**	**(3+1)N-H⁺**	**N211**
a_L	8.53±0.24	5.58±0.04	2.76±0.06	2.06±0.13	1.04±0.01	6.44±0.14
K_L	1.51±0.04	1.83±0.01	3.49±0.03	6.78±0.18	10.3±0.03	1.84±0.18
K_H ($\times 10^4$)	6.34±0.18	5.15±0.03	5.14±0.05	5.08±0.15	4.94±0.07	4.97±0.18
n	4±1	2±0	3±0	2±1	2±0	5±0
K_A	1.68±0.13	2.17±0.04	0.793±0.01	1.06±0.22	0.932±0.02	5.38±0.24
R^2	0.99	0.99	0.99	0.99	0.99	0.99

In the low RH regime, Langmuir-type sorption is mainly responsible for the increase in water content, wherein formation of a layer of water at the surface of a membrane occurs,[124,127] and initial solvation of surficial sulfonic acid groups occurs.[29] This correlates with the accessible surface concentration of sulfonic acid groups and is quantified by the specific site capacity, a_L.[29,193] a_L decreases with the increasing number of N-atoms 0N-H^+ (8.53) > (1+0)N-H^+ (5.58) > (1+1)N-H^+ (2.76) > (3+0)N-H^+ (2.06) > (3+1)N-H^+ (1.04), as listed in Table 4-5 and is consistent with a decrease in surface acidic groups at the membrane surface due to increasing extents of neutralization. In the mid-RH region, Henry-type sorption, which is reliant on sulfonic acid groups within the bulk membrane that provide solvation, [124,128,130,200,236], and the Henry law's coefficient, K_H, is correlated to the IEC of the membranes. K_H decreases in the order 0N-H^+ (6.34×10^{-4}) > (1+0)N-H^+ (5.15×10^{-4}) > (1+1)N-H^+ (5.14×10^{-4}) > (3+0)N-H^+ (5.08×10^{-4}) >(3+1)N-H^+ (4.94×10^{-4}), as the increasing number of pyridyl moieties reduce the IEC.

In the high RH regime, clustering-type sorption becomes a dominant factor to the increase in water vapor sorption. In this case, free water and interconnected ionic clusters form to accommodate more incoming water molecules,[124,127–131] which leads to swelling at various level.[124,127] Both the flexibility of the backbone, and the affinity to water molecules are contributing factors in affecting the clustering-type sorption.[124,127,128] As shown in Figure 4-7, a more discernible concave of sorption was observed in N211, which can also be represented by the highest value in both n and K_A of clustering-type sorption, 5 and 5.38, respectively (Table 4-5). In the clustering-type sorption, n serves as the average number of water molecules per cluster while K_A stands for the extent of water clustering process.[124,127–131] The value of n is dependent on the polymer flexibility, while K_A relies on the acidity. Consequently, compared to the hydrocarbon-based membranes, both the higher flexibility,[57] and the high acidity of Nafion® contribute to its highest value in both n (5), and K_A (5.38).[193]

4.3.6. Transient diffusivity of water vapor

RH-dependent rates of water transient diffusion in membranes were measured by dynamic vapour sorption analyzer. The instantaneous rate of change in mass of water

versus time for a given step in relative humidity surrounding the membrane is shown in Figure B 1 for each membrane in Appendix B. Rates of change in mass occur only when the relative humidity changes. This observation demonstrates that major vaporous water uptake or loss occurs mostly within the first few minutes after a change in RH. In addition, the peak of instantaneous mass-change rate for each membrane is larger in the lower RH regime (e.g., < 30% RH) than in the higher RH regime, as observed in Figure B 1 in Appendix B. This observation has also been reported in other transient diffusion studies.[173–175,190] At the same relative humidity regime, the peak mass-change rate decreases with the increasing number of N-atoms in the polymeric repeat unit: 0N-H^+ > (1+0)N-H^+ > (1+1)N-H^+ > (3+0)N-H^+ > (3+1)N-H^+. For example, for the RH step 0-13%, the peak mass-change rate, dm/dt, is 0.062% s^{-1} for 0N-H^+, 0.029% s^{-1} for (1+0)N-H^+, 0.022% $s^{-1}$for (1+1)N-H^+, 0.017% s^{-1} for (3+0)N-H^+ and 0.011% s^{-1} for (3+1)N-H^+. To further illustrate the transient water diffusion process, the normalized water uptake, [(M_t-M_o)/(M_∞-M_o)], was plotted against time for each membrane, as shown in Figure B 2 in Appendix B. M_t, M_0, and M_∞ represent instantaneous mass, initial mass, and equilibrated mass, respectively. In agreement with the observation of Figure B 1 that the peak of instantaneous mass-change rate is smaller in the higher RH regime, the normalized water uptake requires a longer time to reach 1.0 under higher relative humidity than under lower RH. Similar to Figure B 1, for the same RH step, the time required for the water uptake to reach to the normalized value 1.0 increases with the number of incorporated pyridyl moieties within the polymer.

Transient diffusion represents how quickly water sorption within the membrane responds to the humidity changes. This is an important parameter of a PEM, as it must readily adjust to the dynamic environment within an operating fuel cell.[173] To extract information on transient diffusion of membrane, the Weibull model was employed, see Equation 4-1. The rate constant of diffusion, k_{sorp}, for each membrane under the RH interval was determined by plotting the normalized water uptake against time as shown in Figure B 2 and summarized in Table B 1.

$$\left(\frac{M_t - M_0}{M_\infty - M_0}\right) \cong \exp\left[-\left(k_{sorp}t\right)^A\right] \text{ [200]} \qquad \textbf{Equation 4-1}$$

Transient diffusivity, *D*, was then calculated, and plotted in Figure 4-8 with data given in Table B 2 in Appendix B. Due to limitations of the single exponential fitting (simple exponential smoothing) in Weibull model, discrepancies do exist between the regression

and experimental data after 3000 seconds, especially under high RH steps. The transient diffusivity obtained in this study for N211 lie in the 10^{-6} to 10^{-8} cm^2 s^{-1} range throughout the RH range examined, at 80 °C. This is in good agreement with other reports of N211.[173,174] As seen in Figure 4-8, *D* of each membrane is smaller under high relative humidity, possibly because: i) there may exist a secondary mechanism such as a slower relaxation of the polymer backbone becoming dominant at high relative humidity;[29] ii) there is an increased amount of water present at high RH than in low RH;[29] iii) the enthalpy of solvation that represents the driving force of transient diffusion reduces under high RH;[29,173] iv) a faster non-Fickian diffusion occurs in the lower RH regime.[29,190]

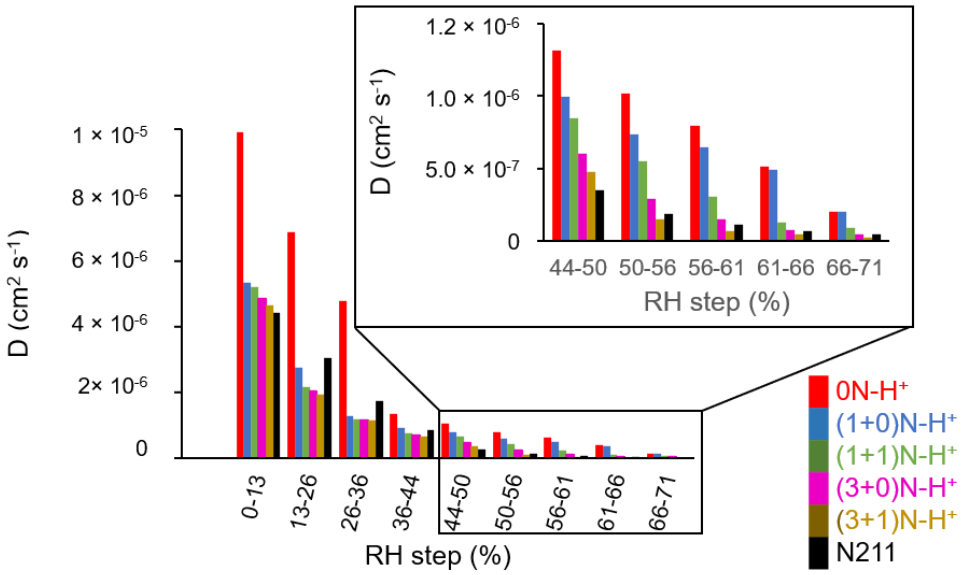

Figure 4-8. Water transient diffusivity, *D*, of each membrane at each relative humidity interval at 80 °C. Data are also provided in Table B 2.

In Figure 4-8, it is found that the transient diffusivity at each RH step decreases with increasing number of nitrogen atoms in the polymer repeating unit. Membranes of 0N-H^+ possesses the highest transient diffusivity in all RH intervals, whereas membranes of (3+1)N-H^+ possesses the lowest. This is likely due to the change in water diffusion and relaxation of the backbone caused by the incorporation of pyridyl groups. The diffusion of water into the membrane mainly depends on interactions between water and sulfonic acid groups within the bulk membrane.[29,175,190] Incorporation of N atoms tends to diminish the transient diffusivity since the effective acid content decreases due to acid-base interactions between sulfonic acid groups and incorporated pyridines. Secondly, the

relaxation time would be extended, and therefore transient diffusivity reduced for polymers with stiffer backbones during the hydration process.[29,200] Incorporation of pyridine moieties is likely to retard the movement of the polymer backbones within a membrane via intermolecular crosslinking,[235] extending the relaxation time and in-turn decreasing the transient diffusivity.

4.3.7. Steady-state liquid-vapor permeation

Measurements of the liquid-vapor permeation (LVP) of membranes were executed with one side exposed to water vapor under various RH and the other side exposed to liquid water, both at 80 °C. The driving force for water transport is controlled by varying the RH of the vapour, which subsequently determines the chemical potential gradient formed across the membrane. Water permeance of the membranes is plotted below as a function of both the RH and the chemical potential gradient of water. As shown in Figure 4-9b, water permeance of each membrane increases linearly with increasing chemical potential gradient. Water permeability, derived from the slope of each linear fit and summarized in Table 4-6, decreases with increasing number of incorporated N-atoms in the polymeric repeat unit, and is correlated with a decreasing water uptake in both liquid and vaporous states (see Table 4-6). For comparison, the permeability of (3+1)N-H^+, 3.3 $\times 10^{-6}$ mol^2 m^{-2} s^{-1} kJ^{-1}, is similar to that of N211, but 0N-H^+ (4.9×10^{-6} mol^2 m^{-2} s^{-1} kJ^{-1}) is much higher.

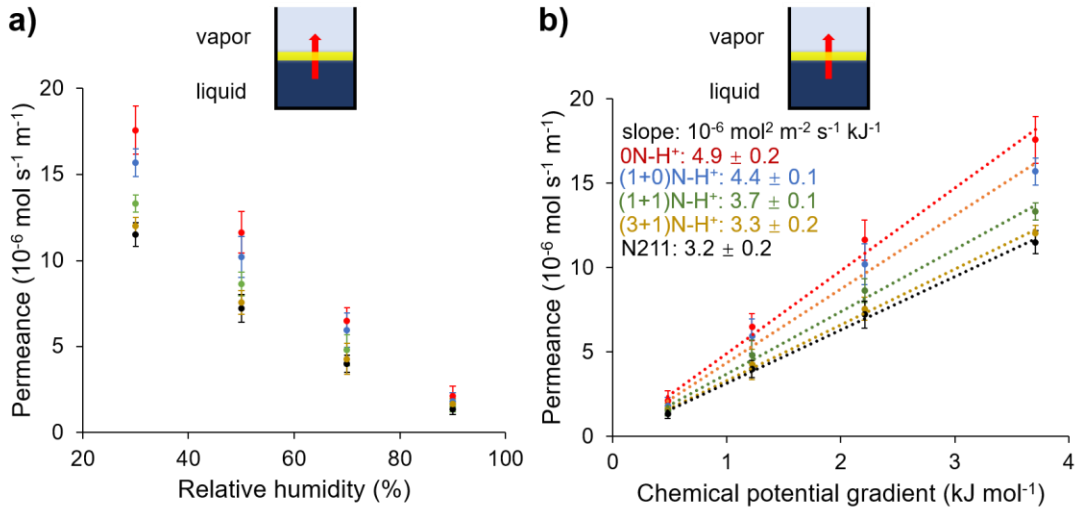

Figure 4-9. Steady-state liquid-vapor permeation plotted as a function of a) the relative humidity and b) the chemical potential gradient of membranes at 80 °C.

Table 4-6. Steady-state liquid-vapour permeability and water uptake (WU) of membranes at 80 °C

membrane	LVP permeability ($\times 10^6$ mol^2 m^{-2} s^{-1} kJ^{-1})	WU_{liquid} (%)[a]	WU_{vapour} (%)[b]
0N-H+	4.9 ± 0.2	80 ± 3	16.8 ± 0.1
(1+0)N-H$^+$	4.4 ± 0.1	54.4 ± 0.7	13.8 ± 0.1
(1+1)N-H$^+$	3.7 ± 0.1	52 ± 3	8.82 ± 0.01
(3+0)N-H$^+$	N/A	N/A	7.55 ± 0.01
(3+1)N-H$^+$	3.3 ± 0.1	49 ± 3	5.71 ± 0.01
N211	3.2 ± 0.1	37 ± 3	4.07 ± 0.01

[a] liquid water uptake at 30 °C.

[b] vaporous water uptake at 30% RH, 80 °C.

4.3.8. Proton conductivity of water vapour humidified state

Proton conductivities of the four HC-based PEMs and N211 reference were measured under different relative humidities at 80 °C and were plotted in Figure 4-10. Proton conductivity of each membrane increases with the relative humidity from 35% to 95%. This increase is because water content increases with RH and water facilitates proton transport. The proton conductivities of both 0N and (1+0)N-H^+ are similar throughout the mid-RH range, and similar to N211, but much higher than (1+1)N-H^+ and (3+1)N-H^+. According to previous work,[232] the adjacent phenyl rings on the central pyridine of (1+0)N-H^+ provide appreciable steric hindrance, which lowers the p*K*a (to 3.25) of the pyridine-H^+ conjugate acid, and hence facilitates proton dissociation compared to an unhindered pyridine moiety. Thus, the addition of one sterically hindered pyridine ((1+0)N-H^+ vs. 0N-H^+) does not lead to a significant reduction in proton conductivity (119 mS cm^{-1} vs 155 mS cm^{-1} at 95% RH and 80 °C, respectively (see Figure 4-10). The addition of a second pyridine (exposed), e.g., (1+1)N-H^+, imparts a significant reduction in conductivity: 13 mS cm^{-1}, compared to that of (1+0)N-H^+ (119 mS cm^{-1}). p*K*a of the conjugate acid of pyridine is 5.25, which means the additional protonated pyridine exists in its un-dissociated form in water.[235] The difference in proton conductivity between (1+1)N-H^+ and (3+1)N-H^+ membranes is, however, minimal (13 vs. 12 mS cm^{-1}) which implies the additional two internally-facing pyridines exert little influence on proton conductivity, and that the presence of the externally exposed pyridine moiety is the determining factor affecting proton conductivity.

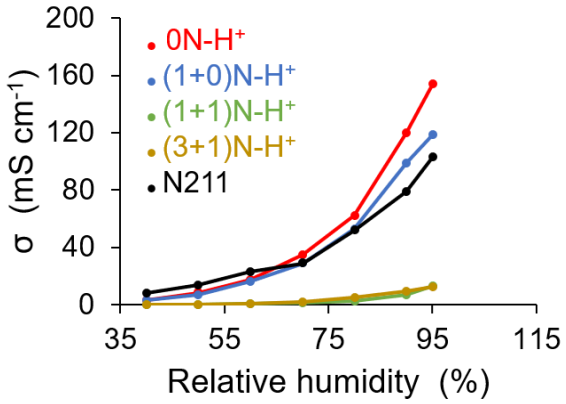

Figure 4-10. Proton conductivity of membranes at 80 °C as a function of RH.

To gain additional insight on the effect of membrane hydration, proton conductivity of each membrane is plotted against DVS-determined water vapor uptake at 80 °C (Figure 4-11a). The increasing water content in this plot is achieved by varying the relative humidity from 40% RH to a maximum of 95% RH. The water contents of (1+0)N-H^+ are marginally lower than its pyridine-free counterpart, 0N-H^+ for a given RH (e.g., 37 vs 43 wt%, respectively, at 95% RH). The proton conductivity of (1+0)N-H^+ is, hence, lower (119 mS cm^{-1} for (1+0)N-H^+ vs. 155 mS cm^{-1} for 0N-H^+ at 95% RH/80 °C). Moreover, the experimental IEC (yielding available protons) is lower as illustrated previously in Table 4-2. However, upon further addition of an externally-directed pyridine, (1+1)N-H^+) and (3+1)N-H^+, vaporous water contents 80 °C are significantly reduced (18 and 13 wt%, respectively at 95% RH. Similarly, proton conductivities diminished to 13 and 12 mS cm^{-1}, respectively. It becomes clear that the presence of exposed basic pyridine groups markedly abate water uptake and proton conductivity compared to internally-facing basic pyridine groups in which the hindered N-atom is sterically hindered.

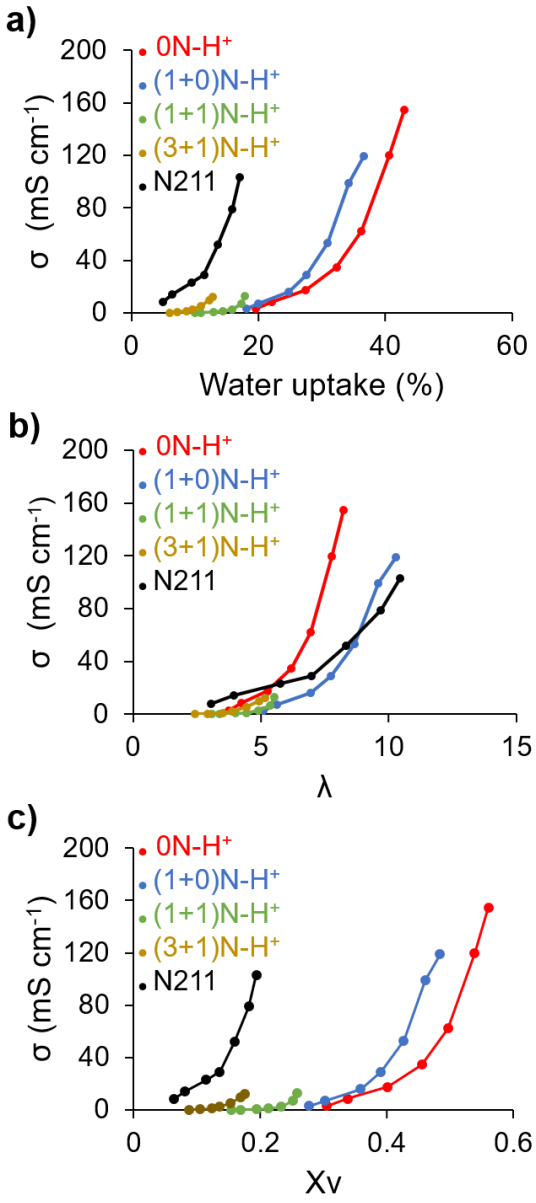

Figure 4-11. In-plane proton conductivity of membranes at 80 ºC versus (a) water vapor uptake, (b) vaporous hydration number and (c) vaporous water content.

In Figure 4-11b conductivity is plotted against λ. Proton conductivities of all membranes are relatively low (< 20 mS cm^{-1}) when λ <5 due to the diminished proton transport when insufficient free water exists within the membrane.[18] Due to the relatively low λ, even at 95 %RH, for both (1+1)N-H^+ (5.5) and (3+1)N-H^+ (5.2), proton conductivities remained comparatively low at 95% RH and 80 ºC (13 mS cm^{-1} and 12 mS cm^{-1}, respectively). In

membranes where larger λ values are observed to exist (λ > 5), unbound water is assumed to be present and proton conductivity increases substantially. In this regime, conductivity may be attributed to the Grotthus mechanism, which depicts proton transport via a series of hydrogen-bond formation and breaking with water molecules.[18,237] The rate of increase in proton conductivity with hydration number for (1+0)N-H^+ is slower that 0N-H^+ (see Figure 4-11b) which could be due to the weaker surface mechanism for proton transport, in which the sulfonic acid group participates in the H-bond formation/breaking process with adjacent water molecules.[18,237]

Proton conductivity against water content is plotted in Figure 4-11c. Proton conductivity increases for each sulfonated polyphenylene as water content increases. Xv, 0.56 and 0.48, is observed for 0N-H^+ and (1+0)N-H^+ at their highest conductivities, 155 and 119 $mScm^{-1}$, respectively. However, for (1+1)N-H^+ and (3+1)N-H^+ the water content, Xv, is only 0.26 and 0.19, respectively, and hence their highest conductivities are reduced to low values, 13 and 12 $mScm^{-1}$, respectively. With an increase in the externally exposed nitrogen groups, inter-molecular acid-base crosslinking is enhanced, which also leads to a reduced water content and reduces proton conductivity.

4.4. Conclusion

A series of novel sulfonated phenylated phenylene polymers containing increasing numbers of nitrogen atoms (0 to 4), 0N-H^+, 1N, (1+1)N-H^+, (3+0)N-H^+, and (3+1)N-H^+, were synthesized to undertake a comparative study of nearly identical structures wherein the only variance was a systematic replacement of carbon atoms with nitrogen atom. As the number of N atoms is increased from 0 to 4 in 0N-H^+ to (3+1)N-H^+, proton conductivity decreases due to acid-base neutralization between the basic pyridine group and acidic –SO_3H group. The effect of self-neutralization on the membranes is to restrict water content through acid-base crosslinking. Liquid and vaporous water sorption, steady-state water permeability, and transient diffusivity decrease in the order: 0N-H^+ > (1+0)N-H^+ > (1+1)N-H^+ > (3+1)N-H^+. When four pyridyl groups are introduced, dimensional swelling of the resulting polymer (3+1)N-H^+ is reduced from 82% to 20%, similar to that of the N211 reference (24%). At 80 ^oC, the steady-state water permeabilities and transient diffusivity of (3+1)N-H^+ are not significantly reduced, compared to N211.

Proton conductivities of fully hydrated membranes, where water volumes remained high and when correlated to water volume, are equal to twice that of N211, depending on water content. This high conductivity is because of the much higher proton carrier concentration as the effective proton mobility were much lower than N211 despite their higher water content. Under reduced RH, proton conductivities are commensurate with water sorption of those polymers containing 2 or more pyridines having lower water content and much lower proton conductivities. Under these conditions (1+1)N-H^+ and (3+1)N-H^+ possess very low proton conductivity as result of a diminished hydration number caused by restricted water uptake, which in turn was the result of the externally-exposed pyridines, which are preferentially protonated and form stronger acid-base crosslinks.

These studies provide insight into the design of proton exchange membranes and transport properties. They serve to direct further optimal placement of atoms to control acid-base interaction, to control the extent of ionic crosslinking, and to maximize transport properties with minimal water content. Future work will be directed to extending these correlations to transport properties in catalyst layers because the requirements for water sorption and proton conductivity are often different from those of membranes. Polymer's interactions with catalysts and support materials in the catalyst layer's formation of porous network adds further complexity of analyzing water sorption and transport through the catalyst layer.

Chapter 5. Influence of the hydrocarbon-based ionomer in the catalyst layer on the mass transport

The work in this chapter has been in preparation as Y. Wu, E. Balogun, S. Holdcroft, Influence of the hydrocarbon-based ionomer in the catalyst layer on the mass transport.

Yang Wu performed all water transport examination, surface characterization, and mathematical modelling approximation. Emmanuel Balogun undertook the membrane electrode assembly preparation and performed the in-situ fuel cell tests. Professor Steven Holdcroft supervised the work conducted.

This chapter will focus on mass transport examination, surficial characterization, mathematical approximation, and interpretation, which were executed by the author of this thesis. Supporting information is provided in Appendix C.

5.1. Introduction

Large scale commercialization of proton exchange membrane fuel cell (PEMFC) demands further reduction in cost (to $30/ kW) and better fuel efficiency (60%).[51,67] To achieve these goals, catalyst layer within the fuel cell received particular attention. Catalyst layer, where the electrochemical reactions develop, comprises agglomerates of carbon-supported platinum particles coated with the proton exchange ionomers (PEI).[51,76,77] Currently, the benchmark ionomer is Nafion®, a perfluorosulfonic acid (PFSA) ionomer. PFSA ionomer facilitates the decay and complicates the recycling of Pt catalyst.[51] Fluorine-free hydrocarbon(HC-)based polymers are easier to functionalize and comparatively more proton-conductive than their perfluorosulfonic counterparts. Subsequently, HC-based ionomers are intensively sought after as alternatives.[56]

Structure-property study on the free-standing hydrocarbon-based membrane is in its infancy.[53,67,68] Reviews on the HC-based ionomers integrated into catalyst layers are even rarer, so far only one by Peron et al.[56] They found that i) polyaromatic polymers are more prone to form true solutions compared to PFSA ionomers in the catalyst ink; ii) lack of phase aggregation and ionic network in the HC-based catalyst layer may cause poor proton conduction; iii) increasing the content of sulfonated HC-based ionomer decreases catalyst layer's porosity and impedes gas diffusion; iv) strong interactions between HC-based ionomer and Pt/C results in the densification of the catalyst layer and impact the fuel cell performance; v) the higher the degree of sulfonation in the ionomer, the higher the water uptake, subsequently the lower gas permeability, and higher the probability of flooding.[56]

Some studies investigated water uptake and transport in catalyst layers containing Nafion® ionomer. Holdcroft et al. reported a larger fraction of mesopores (< 20nm) caused higher water uptake in the catalyst layer because of the more substantial capillary effect.[207] Weber et al. fabricated catalyst layers with superhydrophobic surfaces (contact angle >150°) and increased water content by using electrospray coating technology.[208] Computational studies predicted a higher diffusivity of water vapor in the catalyst layer than the bulk membrane based on porous nature of the former.[174,209–213] An experimental research examined the influence of catalyst layers containing Nafion® ionomer on the liquid-vapor permeation through Nafion® membranes and detected no significant difference.[82]

To date, water transport studies on catalyst layers containing HC-based ionomers are still tentative and are seldom related to the catalyst layer's surficial features or fuel cell performance. No research has been reported on how HC-based ionomers affect water uptake and transport through the catalyst layer. Understanding the influence of HC-based ionomers on water transport within the catalyst layer may assist to bridge fuel cell performance and catalyst layer composition.

Lately, a chemically stable, proton-conductive sulfonated polyaromatic polymer - sulfonated phenylated poly(phenylene) biphenyl (SPPB) was reported (Figure 5-1).[63] *In situ* fuel cell test showed promising results for polymer SPPB both as a free-standing membrane[63] and as proton conductive ionomer in the catalyst layer (> 1 W cm^{-2} peak power density).[214] Yet, little is known about how this novel proton exchange ionomer would affect the water uptake and electrochemical performance of the catalyst layer. The proton conductive ionomer, SPPB, therefore provides an opportunity to characterize the water uptake and transport behavior of the HC-based catalyst layer. In this chapter, water vapor uptake, transient diffusion, and steady-state permeation through the catalyst layer containing SPPB with differing ionomer content were tested and compared to the reference CL of Nafion® ionomer. Electrochemical performances were examined by running in situ fuel cell test on membrane electrode assemblies of catalyst layers incorporated with differing content of SPPB. Surficial characterizations such as contact angle and surficial roughness were also executed on the catalyst layers. The chemical composition (ionomer content) was later correlated to surficial features, water transport, electrochemical performance of the catalyst layer. Such correlation enables an essential understanding of the relationship between catalyst layer composition and fuel cell operation, of the origins behind the cathode flooding phenomenon, and possible the enhancement of water management of the fuel cell.

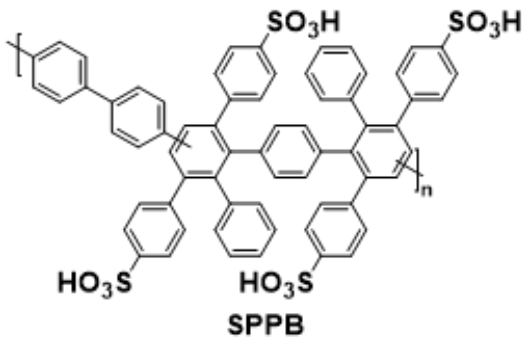

Figure 5-1. Chemical structures of sulfonated phenylated poly(phenylene) biphenyl (SPPB). Identical to Figure 1-13

5.2. Experimental

5.2.1. Material

Membrane and ionomer SPPB, catalyst ink, Milli-pore water, commercial Nafion® membranes were obtained as described in section 2.2, chapter 2.

5.2.2. Catalyst coated membranes (CCM)

Catalyst inks containing i) Nafion® and ii) SPPB of various ionomer contents (10, 15, 20, 25, and 30 wt%) were applied onto pristine N211 membranes via spray coating using a Sono-tak ExactaCoat spray coater (flow rate 0.25 ml/min, Idle power 2 Watts, run power 0.5 Watts), respectively. The catalyst loading was ≅ 0.4 mg Pt cm^{-2} on each side over an area of 5 cm^2 (2.24 x 2.24 cm).

5.2.3. Influence on steady-state water permeation

Detailed information of steady-state liquid-vapor permeation measurement is provided in section 2.4.1, chapter 2.

Catalyst inks containing 20 wt% of Nafion® and SPPB were used in this section. The catalyst inks were spray coated on the membrane substrate, pristine N211, as stated in section 5.2.2 with modifications mentioned below. For each type of catalyst layer (CL Nafion®, or CL SPPB), three experimental groups were prepared: 1) catalyst layer on the desorption side; 2) CL on the sorption side; and 3) CL on both sides of the membrane.

These were compared to a control group, the pristine Nafion® membrane (N211). The membrane with catalyst layers coated on both sides was designated a catalyst-coated membrane (CCM), while the membrane with catalyst layer coated only on the desorption side, facing the water vapor, was denoted $hCCM_d$; and the membrane with catalyst layer coated only on the sorption side, facing the liquid water, was symbolled $hCCM_s$. Five replicates in each group were measured for repeatability and t-test.

5.2.4. Water vapor uptake and transient diffusion

Catalyst inks containing i) Nafion® and ii) SPPB of various ionomer contents (10, 15, 20, 25, and 30 wt%) were applied onto polytetrafluoroethylene (PTFE) sheet (0.2 µm, Sartorius Stedium) following the protocol as mentioned in section 5.2.2. Samples were initially dried in the dynamic vapor sorption (DVS) apparatus (Advance, Surface Measurement Systems, U.K.) at 80 °C and 0 % RH for 6 h, after which the initial dry mass of the sample, M_{dry}, was determined. Then, relative humidity within the sample was regulated to increase from 0 to 70 %, in 10 % increment (± 1.0 %) at 80 °C. Changes in mass of samples, resulted from uptake of water vapor, under established relative humidity were measured with the integrated Ultrabalance™ (± 0.1 µg) in the DVS apparatus. At each set relative humidity, enough time interval was provided (> 120 mins) for the sample to equilibrate to a stabilized mass, $M_{hydrated}$, before further hydration. Water vapor uptake under each relative humidity was then determined as shown in Equation 5-1.

$$water\ uptake = \frac{M_{hydrated} - M_{dry}}{M_{CL,dry}} \text{ [208]} \qquad \textbf{Equation 5-1}$$

where $M_{CL,dry}$ is the weight of dry catalyst layer of the sample.

Effective rate constant of transient diffusion was determined after being approximated to Equation 5-2.[200]

$$\left(\frac{M_{t,CL} - M_{0,CL}}{M_{\infty,CL} - M_{0,CL}}\right) \cong \exp\left[-k_{sorp}t\right] \text{ [200]} \qquad \textbf{Equation 5-2}$$

Here, $M_{t,CL}$, $M_{0,CL}$, $M_{\infty,CL}$, and t are instantaneous mass, initial mass, equilibrated mass of the catalyst layer, and instantaneous time, respectively.

5.2.5. *In situ* fuel cell test

The fuel cell performance of 5 cm^2 active area membrane electrode assemblies was evaluated using the fuel cell test station (Scribner 890CL). The resulting catalyst-coated-membranes were sandwiched between two 5 cm^2 gas diffusion layers (GDL) and compressed using a torque wrench, with the adequacy of compression determined by pressure-sensitive paper. The membrane electrode assembly was conditioned at 80 °C and 100 % relative humidity with constant inlet gas flows of 0.5 standard liters per minute (slpm) hydrogen at the anode and 1.0 standard liters per minute oxygen at the cathode. The cells were conditioned, then equilibrated at open circuit voltage (OCV) prior to subsequent measurements. Polarization curves were taken from the OCV to a shutoff potential of 0.3 V over 200 mA steps, measuring 5 min per point. The resolution of the kinetic region was determined by a current scan from 0.00 – 0.20 A via 0.01 A steps at 1 min per point. Similarly, the ohmic region scan was scanned from 0.50 A – 1.50 A, with 0.50 A steps at 5 min each point. The mass transfer region of the polarization curve was obtained by scanning through 2 A – 15 A, using 1 A steps at 5min $point^{-1}$. The polarization curve were approximated using 0-dimensional (0-D) equation as shown in Equation 5-3:[208]

$$V = E' - b \cdot log\frac{j}{L_{Pt}A_{Pt} \cdot j_0} - \mathrm{j} \cdot R^{dc} \text{ [208]} \qquad \textbf{Equation 5-3}$$

in which V is the cell voltage, j the current density, E' the thermodynamic potential, b the Tafel slope, L_{Pt} the platinum loading (0.4 mg cm^{-2}), A_{Pt} the effective electrochemical surface area, j_0 the catalyst area-normalized exchange current density (8.5 x 10^{-9} A cm^{-2} Pt [79]), and $R^{dc\,(direct\ current)}$ the internal resistance. The values of A_{Pt} and R^{dc} were determined by the least-square analysis (smallest square residual analysis).[208] Only points below 0.8 A cm^{-2} were approximated to Equation 5-3 avoid oxygen transport limitations, which the equation did not include.[208]

5.2.6. Determination of the experimental electrochemical surface area[3]

A VersaStat 4 Potentiostat/Frequency Response Analyzer (FRA) was used for all subsequent electrochemical characterizations. Cyclic voltammograms (CV) of fuel cells were measured by sweeping the potential between 0.04 V and 0.80 V vs. reversible hydrogen electrode (RHE) at a scan rate of 50 mV/s, after an initial potential hold at 0.4 V vs. RHE for 45 sec. The current peaks observed in the CV was used to determine the relative rates of reactions in the PEMFC using different CCMs. Measurement conditions were 80 °C and 100 % RH, with inlet gas flows of 0.5 slpm H_2 at the anode and 0.5 slpm O_2 at the cathode until stable potential of less than 0.15 V was achieved, after which the gas flow at the cathode was set to zero. The electrochemical surface area associated to the hydrogen adsorption can be evaluated by the following equation:

$$ECSA = \frac{Q}{L_{Pt} \times \mu_{Pt}} \qquad \textbf{Equation 5-4}$$

where Q is the charge density of the atomic hydrogen adsorption, L_{Pt} is the Pt loading (0.4 mg Pt/cm^2) and μ_{pt} is a constant (210 mC cm^{-2} Pt), which is the charge required to reduce a monolayer of protons on a polycrystalline Pt surface of 1 cm^2. The Q for desorption and adsorption is extracted by fitting the CV data with the aid of a Core view software.

5.2.7. Characterization tests

Contact angle measurements and surficial roughness measurements are described in section 2.8 and section 2.9 in chapter 2, respectively.

5.3. Results and discussion

5.3.1. Water vapor uptake

Water vapor uptake of each catalyst layer, with differing ionomer content (10 to 30 wt%), was measured with DVS analyzer at 80 °C and plotted in Figure 5-2. As a reference,

[3] Measured and calculated by Emmanuel Balogun.

water vapor uptake curve of the pristine membrane was added in the graph to each catalyst layer containing the respective ionomer. Generally, water vapor uptakes in CLs containing the hydrocarbon-based ionomer, SPPB, are higher than those in the CL Nafion® throughout the examining ionomer content range (10 to 30 wt%). This is not unexpected due to the higher ion exchange capacity (3.3 vs 0.9 mmol g^{-1}) of ionomer SPPB compared to Nafion®.[126]

In Figure 5-2a, water vapor uptake of CL SPPB (10 to 20 wt%) is not significantly different from that of the membrane SPPB throughout the testing RH range. The catalyst layer with 30 wt% of SPPB has lower water vapor uptake than the two catalyst layers with lower ionomer contents. The similarity of water vapor uptake between the pristine membrane and catalyst layers containing the HC-based proton exchange ionomer (PEI) is likely due to the polyaromatic polymers are prone to form true solutions in the catalyst ink.[56] The ultra-thin SPPB film in the CL is likely similar to the bulk membrane SPPB with minimal interfacial effect between SPPB ionomer/vapor given the high ion exchange capacity of the HC based ionomer. On the contrary, water vapor uptake of CL Nafion®, for all the ionomer content tested, is lower than the respective membrane N211 as seen in Figure 5-2b. Water vapor uptake of CL Nafion® (10 vs. 20 wt%) are not significantly different, and both higher than that of CL Nafion® with 30 wt% ionomer content. The water vapor uptake of membrane N211 at 80 °C is consistent with published literature.[29,200] Similar observation was reported that catalyst layer containing Nafion® ionomer possesses diminished water vapor uptake than Nafion® membrane.[201,208] This observation would be explained by the large interfacial effect between Nafion®/ vapor given its hydrophobic fluorine-rich surface[163,165,197] that has been exacerbated when thickness of Nafion® film gets to order of nanometer in the CL.[29,201] The lower water vapor uptake in both CL SPPB and CL Nafion with 30 wt% ionomer content could be attributed to the decreased accessibility of platinum particles.[201]

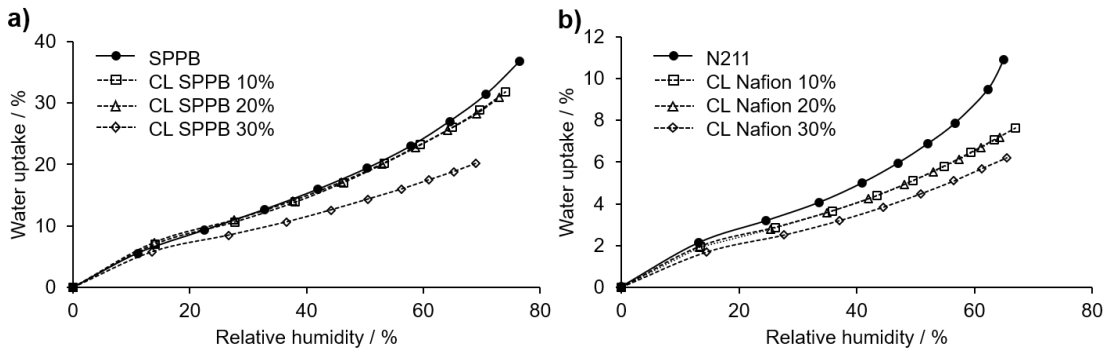

Figure 5-2. Water vapor uptake as a function of relative humidity of (a) CL SPPB and (b) CL Nafion® with different ionomer content at 80 °C.

5.3.2. Influence of catalyst layer on liquid-vapor permeation

Liquid vapor permeation measurements were carried out on each sample group for each type of catalyst layer. The molar water fluxes through each group are presented in Figure 5-3. The asterisks in the graph denote groups that are deemed statistically different from the control group (N211) under the same relative humidity, with confidence level larger than 95% obtained from the t-test.

In Figure 5-3a, as shown for CL SPPB, catalyst layer does not influence water permeation through the membrane regardless of the direction (see Table C 3, Appendix C). Even for a fully coated CCM, the CL SPPB on both sides of the membrane do not influence the molar water flux through the assembly significantly. When deposited on the desorption side of the membrane, CL SPPB does not influence the water permeation through the assembly, $hCCM_d$. This is potentially due to the high porosity and hydrophilicity of catalyst layer cancelling out the influence from addition of membrane/CL and CL/vapor interfaces and wet thickness.[82] Insignificance from the addition of CL on the sorption side, $hCCM_a$, could be attributed to high activity of water outweighs interfacial effect.

A 3-D, multicomponent, multiphase transport computational fluid dynamics study,[238] predicted that water transport limitations associated with the catalyst layer would negatively affect fuel cell performance by retarding O_2 from reaching reaction sites and producing larger ohmic losses.[239] However, in our experimental measurements, the molar water fluxes of liquid-vapor permeation through $hCCM_d$ and $hCCM_s$ for CL Nafion®

(Figure 5-3b) are not significantly different from that through the control group, indicating that depositing CL Nafion on either the desorption ($hCCM_d$) or sorption side ($hCCM_s$) of the membrane does not influence the liquid-vapor permeation within the RH range tested, as reported previously.[82] This can conceivably be explained by the high porosity of the catalyst layer. However, for catalyst-coated membranes (CCM), with catalyst layers coated on both sides of the membrane, the molar water fluxes were approximately 10% lower compared to those of the control group, a pristine N211 membrane, between 30% to 70% RH. No significant differences were found between all three experimental groups *and* the control group at 90% relative humidity, though. This is may be due to experimental difficulties in obtaining data with enough precision under such high relative humidity.

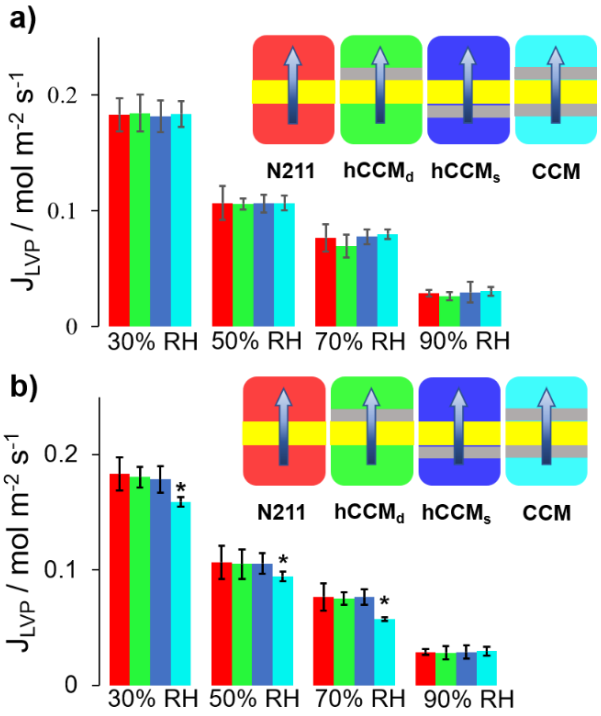

Figure 5-3. Effects of catalyst layers a) CL SPPB and b) CL Nafion® with 20 wt% ionomer content on liquid-vapor permeation through membrane N211 under various relative humidities at 80 °C. $hCCM_d$ represents the catalyst layer facing the water vapor while $hCCM_s$ means the catalyst layer facing the liquid water. The asterisks denote groups that are statistically different from the control group (N211) under the same relative humidity (with the confidence level larger than 95%)

5.3.3. Transient diffusion in the catalyst layer

In time-dependent DVS, the instantaneous change in mass of a sample under certain RH gradient was monitored and recorded. For example, the instantaneous mass-change rate, dm/dt, of CL SPPB (10 wt% ionomer content) under differential RH intervals at 80 °C was plotted against time in Figure C 1, Appendix C. First, the major mass change only occurred in the first 600 s after RH change triggered, which is much shorter than the time interval monitored in this study (>6000 s). This observation demonstrates that enough time was given for each catalyst layer to equilibrate for stable mass before subject to the next RH gradient. Secondly, as seen in Figure C 1, the instantaneous mass change rate for CL SPPB (ionomer content, 10 wt%) is larger when exposed to lower RH intervals than that to higher RH intervals. To quantitatively analyze transient diffusion of water vapor into catalyst layers, the normalized mass gain of CL SPPB (ionomer content, 10 wt%) resulted from hydration against time was plotted in Figure 5-4 as an example. In the normalized mass gain, $(M_t - M_0) / (M_\infty - M_0)$, M_t, M_0, and M_∞ are instantaneous mass, initial mass, and equilibrated mass, respectively. Under higher RH intervals, it takes a longer period for the normalized mass gain to reach to 1 than under lower RH intervals. Reasons behind this observation could possibly be the following: i) driving force of transient diffusion, i.e., the enthalpy of solvation, decreases under higher RH;[29,173] or ii) there exists a faster non-Fickian diffusion under lower RH.[29,190]

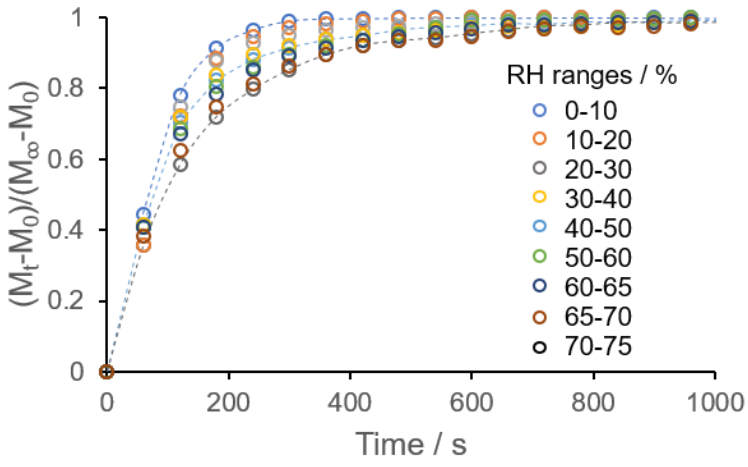

Figure 5-4. Normalized water uptake, $[M_t - M_0] / [M_\infty - M_0]$, over time in sorption period of CL SPPB with 10% ionomer content at 80 °C.

After approximating the normalized mass gain to Equation 5-2, the value of effective rate constant of transient diffusion under each RH interval was determined and plotted in Figure 5-5 for each catalyst layer. In Figure 5-5, the data of a reference membrane N211, was added. The effective rate constants of diffusion for N211 membrane in this research lie within the same order of magnitude of the reported values.[29,200,201] Transient diffusion is a complex process involving accommodation of water molecules into pore structure of the catalyst layer and relaxation of backbone of the CL matrix. The rate constant of transient diffusion represents how promptly the material responds to the dynamic humidity change in an operating fuel cell. In Figure 5-5a, k_{sorp} of CL SPPB with 10% and 20 wt% ionomer content are not statistically different and close to the reference membrane N211 throughout the examining RH intervals at 80 °C. When ionomer content increases to 30 wt%, k_{sorp} of CL SPPB becomes lower compared to the reference or CLs SPPB with smaller ionomer content. Therefore, a lower ionomer content (<30 wt%) favors a larger water vapor uptake in CL SPPB, as mentioned in section 5.3.1, and faster transient diffusion rate. In contrast, ionomer Nafion® is found to slow down transient diffusion in the catalyst layer compared to the pristine membrane N211, throughout the testing range of ionomer content (Figure 5-5b). Similar hindered transient diffusion was previously reported in catalyst layer with ionomer Nafion®.[201] This observation is attributed to the CL/vapor interfacial effect restricts mass transport within Nafion® ionomer thin film because of Nafion's more hydrophobic perfluorinated chemical composition.[201]

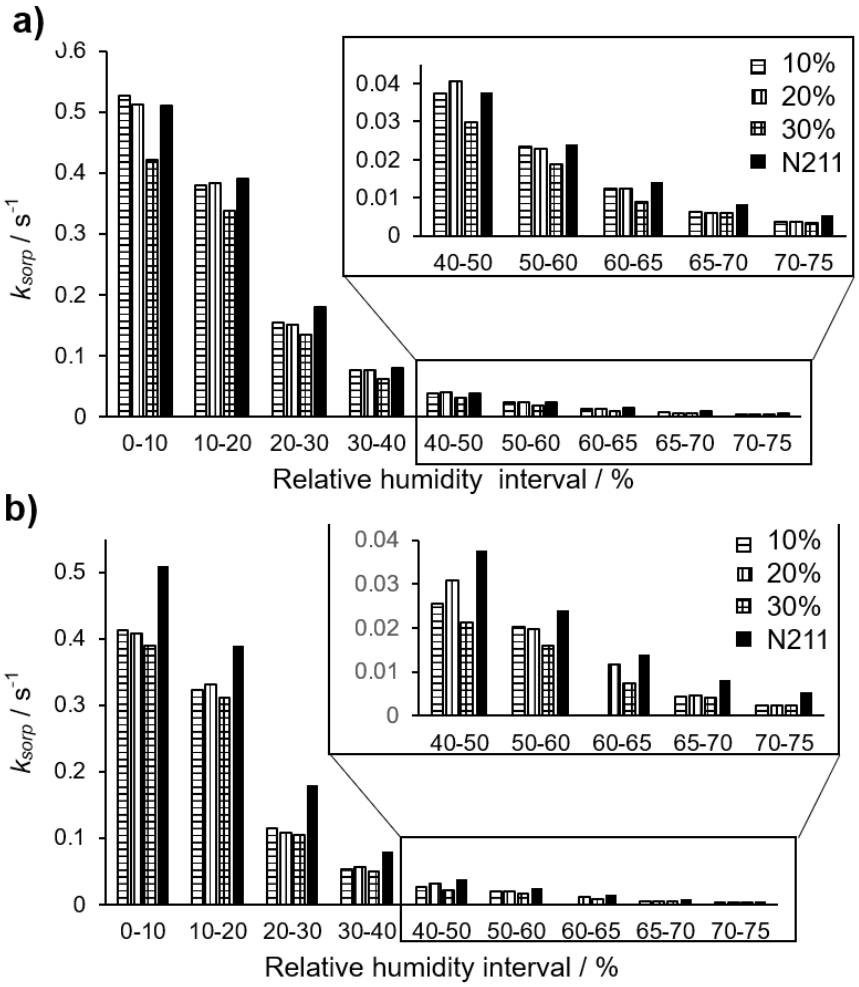

Figure 5-5. Effective rate constant of transient diffusion, k_{sorp}, of (a) CL SPPB and (b) CL Nafion® under different relative humidity intervals at 80 °C.

5.3.4. Surficial characterization

Contact angle measurements were conducted in a class-100 dust free room (less than 100 particles per cubic foot) under ambient environment (20 °C and 40% RH) to discover surficial hydrophobicity of catalyst layers with different ionomers and ionomer content (Figure 5-6). CL SPPB with 10 wt% ionomer content was so wettable that the contact angle could not be measured as seen in Figure 5-6a. Exact contact angle values for each catalyst layer were plotted against ionomer content in Figure 5-7 as the primary y-axis. In the meantime, surface roughness of each catalyst layer was measured with AFM, and the root mean square roughness, R_q, was plotted as the secondary y-axis against

ionomer content in Figure 5-7. In Figure 5-7a, CL SPPB possesses a hydrophilic surface with contact angle smaller than 50°. Increase in ionomer content of SPPB results in an increasing contact angle and decreasing surficial roughness after 15 wt% (contact angle:7°; R_q: 377 nm). The observation of a less rough surface of the CL SPPB with increasing ionomer content could be because the catalyst ink containing more polyaromatic ionomer behaves more like true solution,[56] and renders a smoother surface in spray coating process. The less rough surface (higher ionomer content of SPPB) would then decrease the surficial hydrophilicity (larger contact angle) due to the Cassie-Baxter effect: surface roughness increases the surface hydrophilicity of an already hydrophilic surface.[240] On the contrary, CL Nafion® has a hydrophobic surface as the contact angle is larger than 120° (see Figure 5-7b). The surficial roughness of CL Nafion® varies with the ionomer content in a “V-shape” with the lowest value (221 nm) at 20 wt% as shown in Figure 5-7b. Same as surficial roughness, the contact angle of CL Nafion® changes with the ionomer content in a “V-shape” with the lowest value (126°) at identical ionomer content (20 wt%). The same pattern observed in both contact angle and root mean square roughness changing with ionomer content could be explained by the Cassie-Baxter effect: surface roughness increases the surficial hydrophobicity for an already hydrophobic surface like CL Nafion.[240]

Surficial hydrophilicity/hydrophobicity is not only dependent on the chemical composition of the catalyst layer but also physical characters such as surface roughness. The high ion exchange capacity of ionomer SPPB bestows hydrophilicity to the catalyst layer; the perfluorinated backbone of ionomer Nafion® provides a hydrophobic surface on the catalyst layer. Ionomer content within the catalyst layer governs the extent of hydrophilicity/hydrophobicity by altering the surficial roughness as guided by the Cassie-Baxter effect: increase in ionomer content within the CL SPPB decreases the hydrophilicity by smoothing the surface.

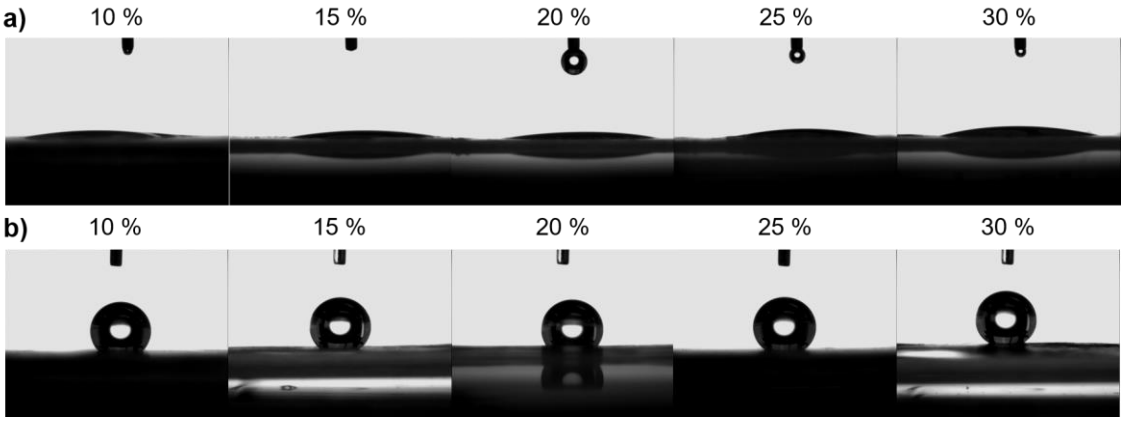

Figure 5-6. Contact angle measurements of (a) CL SPPB and (b) CL Nafion with different ionomer percent (10 to 30 w/t % in 5 % gradient) under ambient environment (20 °C, 40% RH).

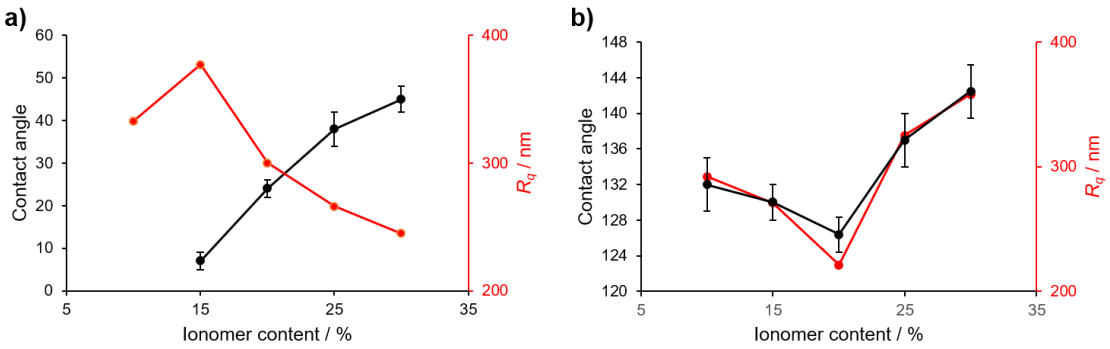

Figure 5-7. Contact angle (primary axis) and root mean square roughness (secondary axis), R_q, of (a) CL SPPB and (b) CL Nafion® with different ionomer content under ambient environment (20 °C, 40% RH).

5.3.5. Fuel Cell Analyses

In situ electrochemical fuel cell tests were executed on membrane electrode assembly equipped with CL SPPB in different ionomer contents coated on the benchmark membrane N211. All tests were operated at 80 °C, 100% RH, 0.5 standard liters per minute H_2, and 1.0 standard liters per minute O_2. As shown in Figure 5-8, cell voltage (primary axis) and power density (secondary axis) of membrane N211 coated with CL SPPB containing various ionomer content (10 to 30 wt%) were plotted against current

density. In Figure 5-8, the MEA with CL SPPB (15 wt% ionomer content) displays the least voltage loss and the highest power density. The peak power density of this MEA is over 1000 mW cm^{-2}.

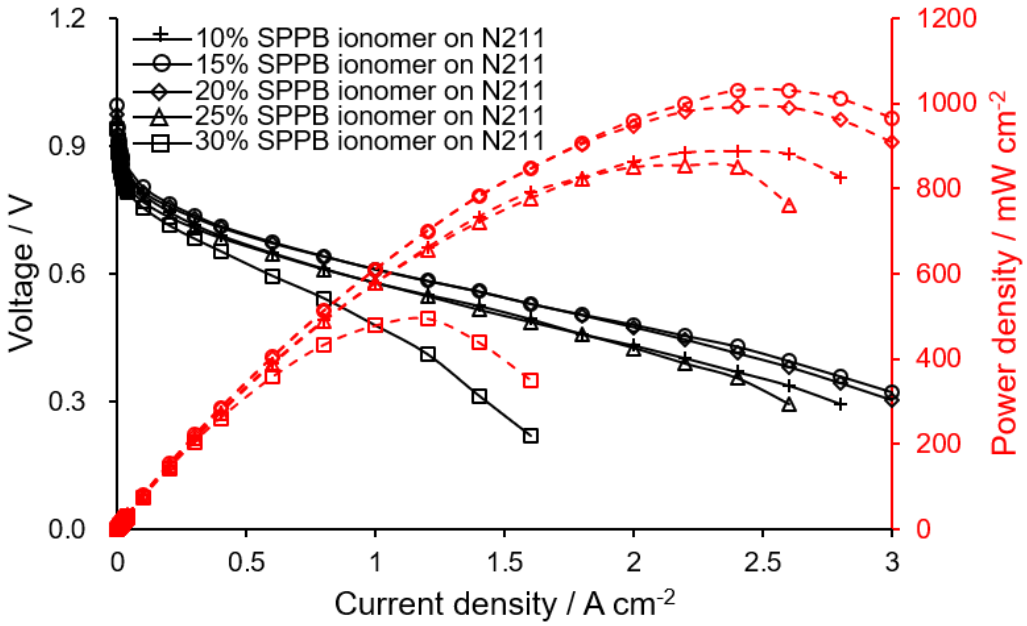

Figure 5-8. Polarization (black lines, primary axis) and power density (red lines, secondary axis) curves showing the performance of sPPB ionomer CCMs with 10, 15, 20, 25 and 30 wt% ionomer in the catalyst layer. Nafion (N211) membrane thickness was 25 µm. Operated at 80 °C, 100% RH, 0.5 standard litres per minute H_2, 1.0 standard litres per minute O_2.

To decipher the electrochemical performance of these MEAs with CL SPPB, the polarization curves in Figure 5-8 were approximated to the 0-D equation (Equation 5-3). Only points below 0.8 A cm^{-2} were taken in approximation to avoid limitations from the oxygen transport which the Equation 5-3 did not consider.[208] Approximated values, determined by the least square analysis (Table 5-1), for the effective electrochemical surface area (A_{Pt}) and internal resistance (R^{dc}) were then plotted against ionomer content as the primary and secondary y-axis, respectively in Figure 5-9. In Figure 5-9, large limits (95% confidence) are observed for the A_{Pt} values. This observation corresponds to the seemingly heteroscedasticity in residual distribution shown in Appendix C. The loss of precision in approximating polarization curve to the 0-D equation possibly originates from

its over-simplification in 1) omitting the influence of oxygen transport overpotential and 2) merely assuming the exchange current density proportional to the ECSA without considering the other reactants' concentration and catalyst's reactivity. Thus, the approximation values showing the general trend against the ionomer content do not necessarily represent the exact magnitude of A_{Pt} and R^{dc}. To further support the trend of ECSA against ionomer content predicted by the 0-D equation, the experimental ECSA values (A_{Pt_exp}) determined by the cyclic voltammograms were added in Table 5-1 and plotted in Figure 5-10. Indeed, both A_{Pt} and A_{Pt_exp} display a similar pattern against ionomer content in Figure 5-9 and Figure 5-10, respectively.

In Figure 5-9, CL SPPB (15 wt% ionomer content) has highest effective electrochemical surface area for the catalyst (93.8 m^2 g^{-1}) and the lowest internal resistance (0.099 Ω cm^2). The internal resistance, when less than15 wt%, decreases with the ionomer content because the presence of more ionomer increases the proton conductance. When greater than 15 wt%, internal resistance increases with the ionomer content. The increase in internal resistance with ionomer content is likely caused by the increase in thickness of the CL as reported before.[208] The effective electrochemical surface area generally decreases with the ionomer content (Figure 5-9 and Figure 5-10). This is probably because the higher ionomer content diminishes the exposure of the catalyst. Interestingly, trend of the effective electrochemical surface area with ionomer content is in accordance with the surface roughness as discussed in section 5.3.4. The increase in surface roughness, generally, corresponds to the increase in the effective ECSA. The rougher the surface of the CL, the greater the exposed area of the platinum particles and, therefore not unexpectedly the higher effective ECSA.

Table 5-1. Value of variables (± limits of 95% confidence) in 0-D equation. Residual distribution is provided in Appendix C.

Ionomer content (%)	b	A_{Pt} (m^2 g^{-1})	R^{dc} (Ω cm^2)	A_{Pt_exp} (m^2 g^{-1})[a]
10	0.077±0.005	77.6±22.1	0.143±0.018	65.3
15	0.078±0.001	93.8±42.7	0.099±0.016	66.2
20	0.067±0.006	35.2±9.1	0.125±0.006	50.7
25	0.075±0.008	34.4±7.8	0.131±0.005	38.9
30	0.077±0.003	38.3±19.4	0.195±0.016	37.5

[a] Experimental electrochemical surface area determined by the cyclic voltammograms, by Emmanuel Balogun.

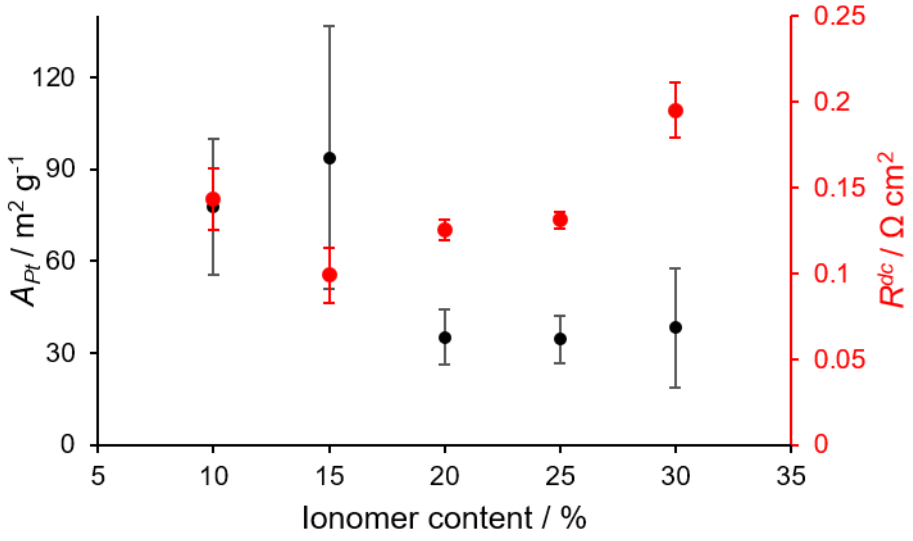

Figure 5-9. Approximated effective electrochemical surface area (primary axis) and internal resistance (secondary axis) extracted from 0-D equation of CL SPPB with various ionomer contents.

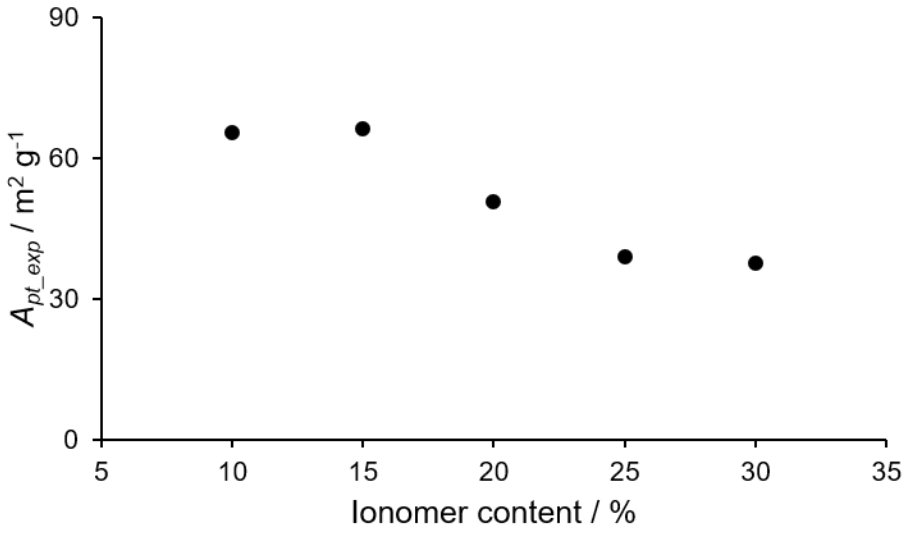

Figure 5-10. Experimental effective electrochemical surface area of CL SPPB with various ionomer contents. Similar trend of A_{Pt_exp} against ionomer content is observed in A_{Pt} vs ionomer content.

Meanwhile, it has been widely acknowledged that CL containing ionomer Nafion® with 30 wt% ionomer content renders the best electrochemical performance.[88,101,241] Therefore, the in situ fuel cell test was also run on the MEA with CL Nafion® (30 wt%) as seen in Figure 5-11. 0-D approximation of the polarization curve provides A_{Pt} and R^{dc} as 12.7±4.1 m^2 g^{-1} and 0.088±0.002 Ω cm^2, respectively. When comparing the two catalyst layers with their respective best performance ionomer content, CL SPPB (15 wt%) and CL Nafion® (30 wt%), it was found that both the effective ECSA (93.8 vs 12.7 m^2 g^{-1}) and internal resistance (0.099 vs 0.088 Ω cm^2) of CL SPPB are higher than CL Nafion®. The lower internal resistance of CL Nafion® (30 wt%) reveals a more conductive catalyst layer composed of Nafion® ionomer that is more phase-segregated and less tortuous transporting protons.[56] However, the high effective ECSA for CL SPPB (15 wt%) demonstrates a more efficient utilization of the platinum catalyst, which is crucial to further cut down cost of the fuel cell.

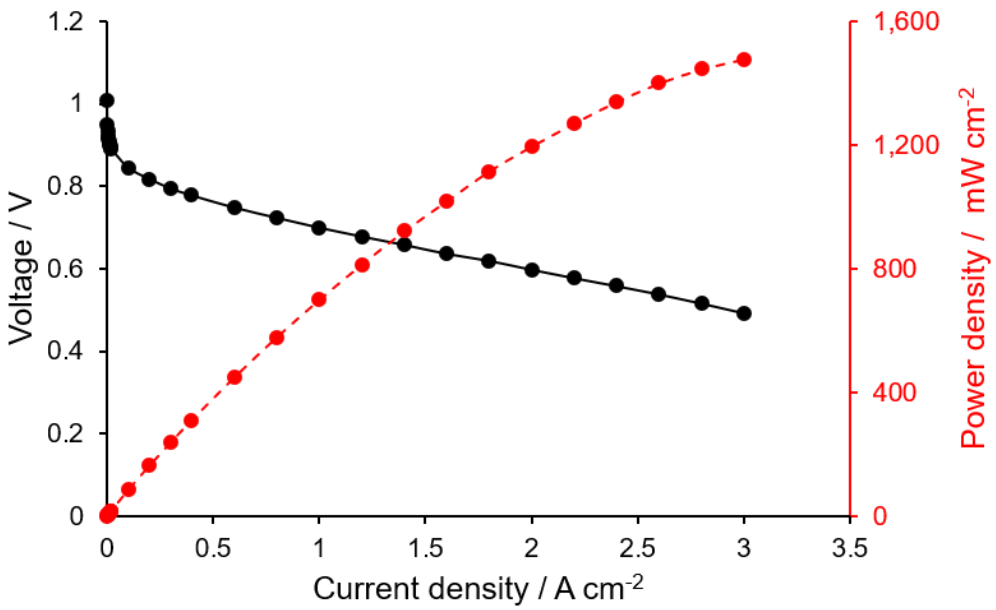

Figure 5-11. **Polarization (black lines, primary axis) and power density (red lines, secondary axis) curves showing the performance of Nafion® ionomer CCMs with 30 wt% ionomer in the catalyst layer. Nafion (N211) membrane thickness was 25 µm. Operated at 80 °C, 100% RH, 0.5 standard litres per minute H_2, 1.0 standard litres per minute O_2.**

5.4. Conclusion

Catalyst layer composed of the novel hydrocarbon-based proton exchange ionomer, SPPB, was studied for a series of mass transport properties, which were later related to surface characterizations (contact angle and surface roughness) and in situ fuel cell tests. In the study, a lower ionomer content in CL SPPB favors a larger water vapor uptake and faster transient diffusion rate. The CL SPPB does not significantly affect the liquid vapor permeation through the membrane electrode assembly, unlike the CL Nafion® deceasing the molar water fluxes by ~10% when coated on both sides of the membrane N211. Noteworthily, surficial hydrophilicity/hydrophobicity is found to be dependent on both the chemical composition (ionomer content) and roughness of the CL. HC-based SPPB with higher IEC makes the catalyst layer hydrophilic. Increase in the ionomer content smoothens the surface, therefore decreases the surface hydrophilicity increases the contact angle of the surface of CL SPPB.

In the *in situ* fuel cell test, CL SPPB (15 wt%) shows the best electrochemical performance with the highest effective ECSA (93.8 $m^2 g^{-1}$) and lowest internal resistance (0.099 Ω cm^2). Interestingly, the effective ECSA and the surficial roughness both decrease with the ionomer content. Also, the internal resistance of the MEA rises with the SPPB ionomer content because the presence of more ionomer likely increases the thickness of the catalyst layer. In summary, future development of HC-based catalyst layer ought to tune ionomer content to decrease internal resistance and increase surface roughness therefore, increase the effective ECSA for premium electrochemical performance.

Chapter 6. Conclusion and future work

6.1. Conclusion

Understanding water transport through innovative polymer electrolyte membranes and porous electrodes is crucial for water management and performance improvements of fuel cells. This thesis expands application of the steady-state permeation protocol, previously for the PFSA membranes, to the novel HC-based polymers, namely the second generations of the sulfonated phenylated poly(phenylene) from the Holdcroft group. Barring the steady-state permeation measurements, this work incorporates transient diffusion to examine the membrane's ability to adjust water content to a dynamic environment. Vapor sorption isotherm, coupled with the Park model, is utilized to correlate vapor sorption behavior to the chemical/structural features such as surficial hydrophilicity and backbone flexibility of the HC-based PEMs. Conductive AFM and surface roughness are also conducted to collectively complete the structure-transport correlation.

Three specific projects are executed and reported. Potential structure features affecting water sorption and transport behaviors are identified. A wholly aromatic and stiff backbone with high degree of sulfonation in SPPB renders a contiguous morphology, high ion exchange capacity and therefore, a low internal resistance coefficient. The stiffer backbone of SPPB is confirmed by its shorter elongation at break than both the HC-based and commercial reference (SPAE and N211, respectively). Sulfonated phenylated poly(phenylene) with the basic pyridyl incorporated exhibits reduced water sorption, water and proton transport, which is more phenomenal when the pyridyl is exposed rather than encumbered. It is because the acid-base interaction induces intermolecular crosslinking among polymer backbones, stiffens the backbone shown in the stress tests, diminishes the morphological rearrangement observed in sorption isotherm, and prolongs the relaxation process shown in transient diffusion. Ionomer SPPB with high acid content bestows the catalyst layer hydrophilicity with higher vapor sorption and transient diffusion than the traditional CL with Nafion® ionomer. Decrease in ionomer content of SPPB roughens the CL's surface and favors vapor sorption and transport. These insights will assist in modifying the structure of future generations of the sulfonated phenylated poly(phenylene) for desirable mass transport through both the membrane and the catalyst

layer, which subsequently leads to electrochemical performance improvements of fuel cells. Detailed summarization of the three projects is provided below.

Initiating the structure-transport correlation for hydrocarbon-based proton exchange membranes

Vapor sorption isotherm and steady-state water permeation of the second generation of sulfonated phenylated poly(phenylene), SPPB, are reported and compared to the HC-based reference (SPAE) and the commercial reference (N211) in chapter 3. Sorption isotherms were investigated using dynamic vapor sorption analyzer, then fitted and interpreted using the Park model. In Langmuir-type sorption, SPAE possesses the highest surface site capacity, representing higher surficial hydrophilicity compared to either SPPB or N211. In Henry-type sorption, K_H values for both SPAE and SPPB are higher than N211 due to their larger ion exchange capacity. In clustering-type sorption, a sharp increase in water sorption is observed for N211 membranes due to a more flexible backbone and more acidic sulfonic acid groups. In steady-state liquid-vapor permeation, SPPB is the most permeable when the thickness is > ~30 μm, as it possesses the lowest internal resistance caused by a large ion exchange capacity and potentially more contiguous internal morphology brought by its wholly aromatic backbone. When thickness is < ~30 μm, SPAE is the most permeable due to its lowest membrane/vapor interfacial resistance, which is confirmed by contact angle measurements and conductive AFM.

From the practical perspective, the hydrophilic surface of SPAE may allow the membrane higher water retention under the dry environment, and subsequently a more stable fuel cell performance under low RH. Meanwhile, the SPPB possesses a quicker response to water concentration bias with its smaller internal resistance coefficient, therefore a faster internal water permeation.

Understanding the effect of acid-base interactions using architecturally-controlled, pyridyl-bearing sulfonated phenylated polyphenylenes

Chapter 4 reports water and proton transport through polymers with similar chemical structure but with an increasing number of strategically-placed N-atoms in the form of pyridyl units. As the number of N-atoms increases, the fraction of immobilized protons of $–SO_3H$ is increased, and the material's ion exchange capacity, proton conductivity, liquid and vaporous water sorption, dimensional swelling, steady-state water permeability, and

transient diffusivity all decrease. With four N-atoms per repeating unit ((3+1)N-H^+), dimensional swelling and steady-state water permeability of the fully hydrated polymer are similar to the N211 reference. However, proton conductivity of (3+1)N-H^+ is substantially reduced, compared to N211, due to its low water sorption.

The addition of basic pyridyl groups increases the likelihood of intermolecular crosslinking among polymer backbones, thereby stiffening the backbone and prolonging its relaxation process during hydration. Since the addition of pyridyl groups lead to enhanced intermolecular crosslinking, polymers containing more nitrogen atoms – (1+1)N-H^+ and (3+1)N-H^+ – appear to avoid appreciable water uptake and exhibit decreased hydration numbers. (3+1)N-H^+ exhibited a low proton conductivity of only 12 mS cm^{-1} with a diminished hydration number (λ = 5.2). For all four membranes, proton conductivity exponentially grows only when λ > 5 (0N-H^+ and (1+0)N-H^+), where the Grotthus mechanism becomes dominant for proton transport. Collectively, an ideal HC-based PEM should maintain a hydration number above 5 and possess a favorable feature, such as limited acid-base interactions (and hence crosslinks) to enhance overall membrane strength, whilst simultaneously preventing a sacrifice in mass transport. This research provides insight to direct further synthesis for optimal placement of atoms to control acid-base interaction, control the extent of ionic crosslinking, to maximize transport properties with minimal swelling.

Understanding the effect of hydrocarbon-based ionomer on water transport through the catalyst layer

Chapter 5 tested water vapor uptake, transient diffusion, and steady-state permeation through the CL containing SPPB with differing ionomer contents and compared them to the reference CL of Nafion® ionomer. Both vapor uptake and the effective rate constant of transient diffusion of CL SPPB are higher than those of CL Nafion®. Addition of the SPPB-containing catalyst layer would not hinder liquid vapor permeation (LVP)e through the membrane-electrode-assembly (MEA). However, an approx. 10% decrease of LVP was measured when both sides of the membrane were coated with Nafion®-containing catalyst layers.

The CL of 15 wt% SPPB possesses the most hydrophilic and roughest surface, which agrees with the highest effective electrochemical surface area (93.8 m^2 g^{-1}) and lowest

internal protic resistance (0.099 Ω cm^2) described by the 0-D equation. Surficial hydrophilicity was found dependent on both the chemical composition and roughness of the CL. HC-based ionomer SPPB makes the catalyst layer hydrophilic with high ion exchange capacity. Increasing the ionomer content smoothens the surface, decreases surface hydrophilicity, and increases the contact angle of the surface of CL SPPB.

This research initiated an extensive experimental analysis of mass transport in the catalyst layer containing novel HC-based ionomer. It demonstrates ionomer in the catalyst layer alters not only its chemical composition but also physical features like surficial roughness. Future development of HC-based catalyst layer ought to tune ionomer content to decrease internal resistance and increase surface roughness, therefore higher effective electrochemical surface area, for the premium electrochemical performance and efficient utilization of the catalyst.

6.2. Future work

Understanding of water sorption and transport through emerging hydrocarbon-based polymer electrolyte membranes is limited, compared to that of the Nafion® membranes. Better knowledge of the structure-transport relationship is urgent to modify the structure of future HC-based polymers for desirable water transport properties. Therefore, electrochemical performance of fuel cells could be enhanced. Future work on water transport through polymer electrode membranes and the porous electrodes can be conducted in three different areas.

Further profiling the structure-property-transport relationship

Given the success at obtaining essential insights from this structure-transport relationship study, it is critical to continue similar water transport studies on other generations of the sulfonated phenylated poly(phenylene). For example, Figure 6-1 shows another structure modification on the tunable SPPB to reduce backbone linearity, promote macromolecular entanglement and therefore, further decrease water sorption.[125] A larger coverage of the structure-transport study renders more insights on future structure-modification to facilitate water and proton transport, abate volume swelling, and increase mechanical robustness of novel HC-based proton exchange membranes.

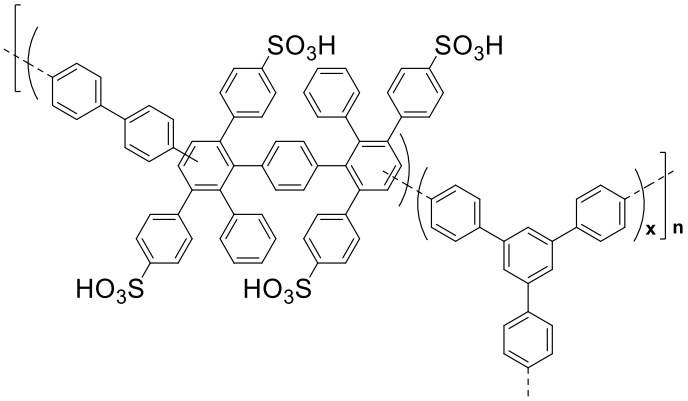

Figure 6-1. Chemical structure of the sulfonated phenylated poly(phenylene)containing a branching unit, where x is the degree of branching in moles. [125]

Simplifying units of the steady-state permeation model

In this thesis, steady-state permeation (diffusion) takes chemical potential gradient (kJ mol^{-1}) as the driving force, which causes relatively complicated units of the permeability (mol^2 m^{-1} s^{-1} kJ^{-1}), the interfacial resistance (kJ m^2 s mol^{-2}) and the internal resistance coefficient (kJ m s mol^{-2}). Complex units of those parameters make the steady-state permeation model less appealing and hard to compare with other water transport studies. Therefore, future work can also focus on simplifying the units reported for steady-state permeation models. Some initial efforts have been reported and are shown below.[126]

Liquid-vapor permeation data for the three membranes in chapter 3 under 30% RH and 70 °C were converted to the Fickian diffusion coefficient, $D_{Fickian}$, and are presented in the first row of Table 6-1.[164] The diffusion coefficient was calculated as $D_{Fickian} = J_{LVP} \times L/\Delta C$, where J_{LVP} is the molar water flux of liquid-vapor permeation, L is the wet thickness (33 μm), and ΔC the concentration difference between liquid water and water vapor under 30% RH and 70 °C.[164] Molar concentration of liquid water at 70 °C is 54.3 M (density of liquid water: 0.978 g/mL). Molar concentration of water vapor 30% RH at 70 °C is 0.00328 M (saturated water vapor pressure: 0.308 atm, 30% RH vapor pressure: 0.0923 atm). The Fickian diffusivity of N211 derived in this study agrees with the reported values in the same

order of magnitude (10^{-6} cm^2 s^{-1}) under similar conditions, 70 °C and 30 to 50 % RH.[171,176,242]

Permeability, *P*, is the multiplication of permeance and the wet thickness of the membrane. The liquid-vapor permeabilities of the three membranes under 30% RH and 70 °C were included in the second row of Table 6-1. The liquid-vapor permeability of N211 in this study agrees with the reported values, 1 to 4 $\times 10^{-6}$ mol^2 m^{-1} s^{-1} kJ^{-1}.[163–165] To facilitate literature comparisons of permeability, the units kJ was replaced with 10^6 g m^2 s^{-2}, and mol was replaced with 18 g, the molar mass of water. These values are shown in the third row of Table 6-1.

These attempts are primitive, and therefore more attention and thoughts should be concentrated on simplifying the steady-state model, making it more relevant and convenient for future water transport studies.

Table 6-1. Water diffusion coefficient and Permeability for the SPPB, SPAE, and N211 membranes under 30% RH and 70 °C

membrane	SPPB	SPAE	N211
$D_{Fickian}$ ($\times 10^6$ cm^2 s^{-1})	1.63 ± 0.05	1.43 ± 0.03	1.11 ± 0.05
P ($\times 10^6$ mol^2 m^{-1} s^{-1} kJ^{-1})[a]	2.4 ± 0.1	2.2 ± 0.1	1.6 ± 0.1
P ($\times 10^{10}$ g m^{-3} s)[b]	7.8 ± 0.3	7.1 ± 0.3	5.2 ± 0.2

[a] Permeability, multiplication of permeance and the wet thickness, of membranes
[b] Permeability converted to base units

Studying ultrathin hydrocarbon-based polymers

Membrane/vapor and membrane/CL interfacial effect are crucial in mass transport. However, understanding of this interfacial effect and characterization techniques are not always available. In chapter 3, interfacial resistance was examined and correlated to the results obtained from conductive AFM, contact angle measurement, and Park model approximation. Chapter 5 tested influence of the

membrane/CL interface on water transport. However, much more could be done if ultrathin (hundreds of nanometers scale) hydrocarbon-based polymer was available.

In the ultrathin films, spatial confinement affects the morphological pattern and backbone interactions, causing an anisotropic ionic domain orientation, and subsequently a significant difference from the bulk membrane.[243–247] Interfacial effect of phase-segregated polymers has been an attractive research topic.[204,205,248–260] Symbolizing the interface of bulk membrane, ultrathin films receive a lot of attention.[243–247] Investigating water sorption and transport through ultrathin hydrocarbon-based polymers, if available, would benefit development of the fuel cell in two aspects.

1) To gain better understanding of surficial morphology features and interfacial mass transport properties of bulk membranes. Therefore, the rate-limiting membrane/vapor interface in liquid-vapor permeation can gain extra insights to be possibly ameliorated.

2) To study the structure and behavior of ionomer films in the catalyst layers of electrochemical devices. A better understanding of ionomer/catalyst and ionomer/vapor interactions is the key element to increase the triple-phase boundary, catalyst efficiency, and ultimately electrochemical performance of fuel cells.

References

[1] J. Krane, Climate Risk and the Fossil Fuel Industry: Two Feet High and Rising, James A. Baker III Institute for Public Policy of Rice University, 2016. https://scholarship.rice.edu/handle/1911/91261 (accessed August 16, 2020).

[2] World Energy Resources 2016, World Energy Counc. (n.d.). https://www.worldenergy.org/publications/entry/world-energy-resources-2016 (accessed August 16, 2020).

[3] P.J. Sellers, D.S. Schimel, B. Moore, J. Liu, A. Eldering, Observing carbon cycle–climate feedbacks from space, Proc. Natl. Acad. Sci. 115 (2018) 7860–7868. https://doi.org/10.1073/pnas.1716613115.

[4] The 2016 BP Statistical Review of World Energy, Watts That. (2016). https://wattsupwiththat.com/2016/06/10/the-2016-bp-statistical-review-of-world-energy/ (accessed August 16, 2020).

[5] Mission Innovation, (n.d.). http://mission-innovation.net/ (accessed August 16, 2020).

[6] Energy Fact Book 2019-2020, 2019. https://www.nrcan.gc.ca/sites/www.nrcan.gc.ca/files/energy/pdf/Energy%20Fact%20Book_2019_2020_web-resolution.pdf.

[7] O.Z. Sharaf, M.F. Orhan, An overview of fuel cell technology: Fundamentals and applications, Renew. Sustain. Energy Rev. 32 (2014) 810–853. https://doi.org/10.1016/j.rser.2014.01.012.

[8] Fuel Cell Systems Explained, 1st ed., John Wiley & Sons, Ltd, 2003. https://doi.org/10.1002/9781118878330.

[9] Hydrogen: Status and Possibilities - University of Victoria, n.d. https://www.uvic.ca/research/centres/globalstudies/publications/publicationsdb/pubs/hydrogen-status-and-possibilities-id-273.php (accessed August 18, 2020).

[10] S.J. Hamrock, M.A. Yandrasits, Proton Exchange Membranes for Fuel Cell Applications, J. Macromol. Sci. Part C. 46 (2006) 219–244. https://doi.org/10.1080/15583720600796474.

[11] G. Sandstede, E.J. Cairns, V.S. Bagotsky, K. Wiesener, History of low temperature fuel cells, in: Handb. Fuel Cells, American Cancer Society, 2010. https://doi.org/10.1002/9780470974001.f104011.

[12] Fuel Cell Electric Vehicles Powered by Ballard Have Now Driven Over 50 Million Kilometers – Enough to Circle the Globe 1,250 Times, (n.d.). https://www.ballard.com/about-ballard/newsroom/news-releases/2020/08/04/fuel-cell-electric-vehicles-powered-by-ballard-have-now-driven-over-50-million-kilometers-enough-to-circle-the-globe-1-250-times (accessed August 19, 2020).

[13] N. Garland, K. McMurphy, J. Kopasz, T. Benjamin, The Department of Energy's Fuel Cell Subprogram, in: 2008.

[14] N. Garland, D. Papageorgopoulos, J. Stanford, Hydrogen and Fuel Cell Technology: Progress, Challenges, and Future Directions, Energy Procedia. 28 (2012) 2–11. https://doi.org/10.1016/j.egypro.2012.08.034.

[15] J. Marcinkoski, J. Spendelow, A. Wilson, D. Papageorgopoulos, Fuel Cell System Cost - 2015, Department of Energy, United States of America, 2015.

[16] D.P. Wilkinson, J. Zhang, R. Hui, J. Fergus, X. Li, J. Zhang, R. Hui, J. Fergus, X. Li, Proton Exchange Membrane Fuel Cells : Materials Properties and Performance, CRC Press, 2009. https://doi.org/10.1201/9781439806661.

[17] J. Matthey, The Role of Platinum in Proton Exchange Membrane Fuel Cells, Johns. Matthey Technol. Rev. (n.d.). https://www.technology.matthey.com/article/57/4/259-271/ (accessed August 19, 2020).

[18] K. Jiao, X. Li, Water transport in polymer electrolyte membrane fuel cells, Prog. Energy Combust. Sci. 37 (2011) 221–291. https://doi.org/10.1016/j.pecs.2010.06.002.

[19] F. Barbir, PEM Fuel Cells - Theory and Practice - 2nd Edition, Elsevier, 2012.

[20] J.E. Mueller, D. Fantauzzi, T. Jacob, Multiscale Modeling of Electrochemical Systems, in: Electrocatalysis, John Wiley & Sons, Ltd, 2014: pp. 1–74. https://doi.org/10.1002/9783527680436.ch1.

[21] K.D. Kreuer, Hydrocarbon membranes, in: Handb. Fuel Cells, American Cancer Society, 2010. https://doi.org/10.1002/9780470974001.f303037.

[22] P. Atkins, J. de Paula, J. Keeler, Atkins' Physical Chemistry, Eleventh Edition, Oxford University Press, Oxford, New York, 2017.

[23] M. Eikerling, A. Kulikovsky, Polymer Electrolyte Fuel Cells: Physical Principles of Materials and Operation, CRC Press, 2015. https://www.routledge.com/Polymer-Electrolyte-Fuel-Cells-Physical-Principles-of-Materials-and-Operation/Eikerling-Kulikovsky/p/book/9781138077447 (accessed August 19, 2020).

[24] R. Devanathan, Recent developments in proton exchange membranes for fuel cells, Energy Environ. Sci. 1 (2008) 101–119. https://doi.org/10.1039/B808149M.

[25] J.W.T. Grubb, Fuel cell, US2913511A, 1959. https://patents.google.com/patent/US2913511A/en (accessed August 19, 2020).

[26] Polymers for PEM Fuel Cells, 1st ed., John Wiley & Sons, Ltd, 2014. https://doi.org/10.1002/9781118869345.

[27] Y. Tanaka, Ion Exchange Membranes-Fundamentals and Applications-2nd edition, Elsevier Science, 2015.

[28] R. Borup, J. Meyers, B. Pivovar, Y.S. Kim, R. Mukundan, N. Garland, D. Myers, M. Wilson, F. Garzon, D. Wood, P. Zelenay, K. More, K. Stroh, T. Zawodzinski, J. Boncella, J.E. McGrath, M. Inaba, K. Miyatake, M. Hori, K. Ota, Z. Ogumi, S. Miyata, A. Nishikata, Z. Siroma, Y. Uchimoto, K. Yasuda, K. Kimijima, N. Iwashita, Scientific Aspects of Polymer Electrolyte Fuel Cell Durability and Degradation, Chem. Rev. 107 (2007) 3904–3951. https://doi.org/10.1021/cr050182l.

[29] A. Kusoglu, A.Z. Weber, New Insights into Perfluorinated Sulfonic-Acid Ionomers, Chem. Rev. 117 (2017) 987–1104. https://doi.org/10.1021/acs.chemrev.6b00159.

[30] T.D. Gierke, G.E. Munn, F.C. Wilson, The morphology in nafion perfluorinated membrane products, as determined by wide- and small-angle x-ray studies, J. Polym. Sci. Polym. Phys. Ed. 19 (1981) 1687–1704. https://doi.org/10.1002/pol.1981.180191103.

[31] W.Y. Hsu, T.D. Gierke, Ion transport and clustering in nafion perfluorinated membranes, J. Membr. Sci. 13 (1983) 307–326. https://doi.org/10.1016/S0376-7388(00)81563-X.

[32] J.A. Elliott, S. Hanna, J.N. Newton, A.M.S. Elliott, G.E. Cooley, Elimination of orientation in perfluorinated ionomer membranes, Polym. Eng. Sci. 46 (2006) 228–234. https://doi.org/10.1002/pen.20478.

[33] E.J. Roche, M. Pineri, R. Duplessix, A.M. Levelut, Small-angle scattering studies of nafion membranes, J. Polym. Sci. Polym. Phys. Ed. 19 (1981) 1–11. https://doi.org/10.1002/pol.1981.180190101.

[34] M. Fumagalli, S. Lyonnard, G. Prajapati, Q. Berrod, L. Porcar, A. Guillermo, G. Gebel, Fast Water Diffusion and Long-Term Polymer Reorganization during Nafion Membrane Hydration Evidenced by Time-Resolved Small-Angle Neutron Scattering, J. Phys. Chem. B. 119 (2015) 7068–7076. https://doi.org/10.1021/acs.jpcb.5b01220.

[35] P.C. van der Heijden, A. de la Rosa, G. Gebel, O. Diat, Relaxation of drawn Nafion films studied with birefringence experiments, Polym. Adv. Technol. 16 (2005) 102–107. https://doi.org/10.1002/pat.553.

[36] B. Loppinet, G. Gebel, Rodlike Colloidal Structure of Short Pendant Chain Perfluorinated Ionomer Solutions, Langmuir. 14 (1998) 1977–1983. https://doi.org/10.1021/la9710987.

[37] G. Gebel, Structural evolution of water swollen perfluorosulfonated ionomers from dry membrane to solution, Polymer. 41 (2000) 5829–5838. https://doi.org/10.1016/S0032-3861(99)00770-3.

[38] E.J. Roche, M. Pineri, R. Duplessix, Phase separation in perfluorosulfonate ionomer membranes, J. Polym. Sci. Polym. Phys. Ed. 20 (1982) 107–116. https://doi.org/10.1002/pol.1982.180200109.

[39] H.-G. Haubold, Th. Vad, H. Jungbluth, P. Hiller, Nano structure of NAFION: a SAXS study, Electrochimica Acta. 46 (2001) 1559–1563. https://doi.org/10.1016/S0013-

4686(00)00753-2.

[40] J.A. Elliott, S. Hanna, A.M.S. Elliott, G.E. Cooley, Interpretation of the Small-Angle X-ray Scattering from Swollen and Oriented Perfluorinated Ionomer Membranes, Macromolecules. 33 (2000) 4161–4171. https://doi.org/10.1021/ma991113+.

[41] K.M. Cable, K.A. Mauritz, R.B. Moore, Anisotropic ionic conductivity in uniaxially oriented perfluorosulfonate ionomers, Chem. Mater. 7 (1995) 1601–1603. https://doi.org/10.1021/cm00057a002.

[42] L. Rubatat, A.L. Rollet, G. Gebel, O. Diat, Evidence of Elongated Polymeric Aggregates in Nafion, Macromolecules. 35 (2002) 4050–4055. https://doi.org/10.1021/ma011578b.

[43] L. Rubatat, G. Gebel, O. Diat, Fibrillar Structure of Nafion: Matching Fourier and Real Space Studies of Corresponding Films and Solutions, Macromolecules. 37 (2004) 7772–7783. https://doi.org/10.1021/ma049683j.

[44] M.-H. Kim, C.J. Glinka, S.A. Grot, W.G. Grot, SANS Study of the Effects of Water Vapor Sorption on the Nanoscale Structure of Perfluorinated Sulfonic Acid (NAFION) Membranes, Macromolecules. 39 (2006) 4775–4787. https://doi.org/10.1021/ma060576u.

[45] K. Schmidt-Rohr, Q. Chen, Parallel cylindrical water nanochannels in Nafion fuel-cell membranes, Nat. Mater. 7 (2008) 75–83. https://doi.org/10.1038/nmat2074.

[46] A. Kusoglu, T.J. Dursch, A.Z. Weber, Nanostructure/Swelling Relationships of Bulk and Thin-Film PFSA Ionomers, Adv. Funct. Mater. 26 (2016) 4961–4975. https://doi.org/10.1002/adfm.201600861.

[47] K.-D. Kreuer, G. Portale, A Critical Revision of the Nano-Morphology of Proton Conducting Ionomers and Polyelectrolytes for Fuel Cell Applications, Adv. Funct. Mater. 23 (2013) 5390–5397. https://doi.org/10.1002/adfm.201300376.

[48] A.-L. Rollet, O. Diat, G. Gebel, A New Insight into Nafion Structure, J. Phys. Chem. B. 106 (2002) 3033–3036. https://doi.org/10.1021/jp020245t.

[49] Q. Berrod, S. Lyonnard, A. Guillermo, J. Ollivier, B. Frick, A. Manseri, B. Améduri, G. Gébel, Nanostructure and Transport Properties of Proton Conducting Self-Assembled Perfluorinated Surfactants: A Bottom-Up Approach toward PFSA Fuel Cell Membranes, Macromolecules. 48 (2015) 6166–6176. https://doi.org/10.1021/acs.macromol.5b00770.

[50] K.-D. Kreuer, Ion Conducting Membranes for Fuel Cells and other Electrochemical Devices, Chem. Mater. 26 (2014) 361–380. https://doi.org/10.1021/cm402742u.

[51] S. Holdcroft, Fuel Cell Catalyst Layers: A Polymer Science Perspective, Chem. Mater. 26 (2014) 381–393. https://doi.org/10.1021/cm401445h.

[52] J. Miyake, K. Miyatake, Fluorine-free sulfonated aromatic polymers as proton exchange membranes, Polym. J. 49 (2017) 487–495.

https://doi.org/10.1038/pj.2017.11.

[53] D.W. Shin, M.D. Guiver, Y.M. Lee, Hydrocarbon-Based Polymer Electrolyte Membranes: Importance of Morphology on Ion Transport and Membrane Stability, Chem. Rev. 117 (2017) 4759–4805. https://doi.org/10.1021/acs.chemrev.6b00586.

[54] A. Kraytsberg, Y. Ein-Eli, Review of Advanced Materials for Proton Exchange Membrane Fuel Cells, Energy Fuels. 28 (2014) 7303–7330. https://doi.org/10.1021/ef501977k.

[55] J.A. Kerres, Design Concepts for Aromatic Ionomers and Ionomer Membranes to be Applied to Fuel Cells and Electrolysis, Polym. Rev. 55 (2015) 273–306. https://doi.org/10.1080/15583724.2015.1011754.

[56] J. Peron, Z. Shi, S. Holdcroft, Hydrocarbon proton conducting polymers for fuel cell catalyst layers, Energy Environ. Sci. 4 (2011) 1575–1591. https://doi.org/10.1039/C0EE00638F.

[57] T.J. Peckham, S. Holdcroft, Structure-Morphology-Property Relationships of Non-Perfluorinated Proton-Conducting Membranes, Adv. Mater. 22 (2010) 4667–4690. https://doi.org/10.1002/adma.201001164.

[58] H.-F. Lee, B. Britton, Y.-C. Huang, T.J. Peckham, Y.-Y. Hsu, Y.-C. Tseng, P.-C. Huang, C.-C. Lee, M.-Y. Chang, S. Holdcroft, W.-Y. Huang, Effect of ketone versus sulfone groups on the properties of poly(arylene ether)-based proton exchange membranes, J. Mater. Sci. 51 (2016) 9805–9821. https://doi.org/10.1007/s10853-016-0214-z.

[59] J. Han, K. Kim, J. Kim, S. Kim, S.-W. Choi, H. Lee, J. Kim, T.-H. Kim, Y.-E. Sung, J.-C. Lee, Cross-linked highly sulfonated poly(arylene ether sulfone) membranes prepared by in-situ casting and thiol-ene click reaction for fuel cell application, J. Membr. Sci. 579 (2019) 70–78. https://doi.org/10.1016/j.memsci.2019.02.048.

[60] L. Wang, Z. Liu, Y. Liu, L. Wang, Crosslinked polybenzimidazole containing branching structure with no sacrifice of effective N-H sites: Towards high-performance high-temperature proton exchange membranes for fuel cells, J. Membr. Sci. 583 (2019) 110–117. https://doi.org/10.1016/j.memsci.2019.04.030.

[61] T.J.G. Skalski, M. Adamski, B. Britton, E.M. Schibli, T.J. Peckham, T. Weissbach, T. Moshisuki, S. Lyonnard, B.J. Frisken, S. Holdcroft, Sulfophenylated Terphenylene Copolymer Membranes and Ionomers, ChemSusChem. 11 (2018) 4033–4043. https://doi.org/10.1002/cssc.201801965.

[62] J. Miyake, R. Taki, T. Mochizuki, R. Shimizu, R. Akiyama, M. Uchida, K. Miyatake, Design of flexible polyphenylene proton-conducting membrane for next-generation fuel cells, Sci. Adv. 3 (2017) eaao0476. https://doi.org/10.1126/sciadv.aao0476.

[63] M. Adamski, T.J.G. Skalski, B. Britton, T.J. Peckham, L. Metzler, S. Holdcroft, Highly Stable, Low Gas Crossover, Proton-Conducting Phenylated Polyphenylenes, Angew. Chem. Int. Ed. 56 (2017) 9058–9061. https://doi.org/10.1002/anie.201703916.

[64] T.J.G. Skalski, B. Britton, T.J. Peckham, S. Holdcroft, Structurally-Defined, Sulfo-Phenylated, Oligophenylenes and Polyphenylenes, J. Am. Chem. Soc. 137 (2015) 12223–12226. https://doi.org/10.1021/jacs.5b07865.

[65] K. Kang, D. Kim, Pendant dual-sulfonated poly(arylene ether ketone) multi-block copolymer membranes for enhanced proton conductivity at reduced water swelling, J. Membr. Sci. 578 (2019) 103–110. https://doi.org/10.1016/j.memsci.2019.02.043.

[66] K.H. Lee, J.Y. Chu, A.R. Kim, D.J. Yoo, Enhanced Performance of a Sulfonated Poly(arylene ether ketone) Block Copolymer Bearing Pendant Sulfonic Acid Groups for Polymer Electrolyte Membrane Fuel Cells Operating at 80% Relative Humidity, ACS Appl. Mater. Interfaces. 10 (2018) 20835–20844. https://doi.org/10.1021/acsami.8b03790.

[67] M.A. Hickner, H. Ghassemi, Y.S. Kim, B.R. Einsla, J.E. McGrath, Alternative Polymer Systems for Proton Exchange Membranes (PEMs), Chem. Rev. 104 (2004) 4587–4612. https://doi.org/10.1021/cr020711a.

[68] H. Zhang, P.K. Shen, Recent Development of Polymer Electrolyte Membranes for Fuel Cells, Chem. Rev. 112 (2012) 2780–2832. https://doi.org/10.1021/cr200035s.

[69] L. Gubler, T. Nauser, F.D. Coms, Y.-H. Lai, C.S. Gittleman, Perspective—Prospects for Durable Hydrocarbon-Based Fuel Cell Membranes, J. Electrochem. Soc. 165 (2018) F3100. https://doi.org/10.1149/2.0131806jes.

[70] H. Hou, M.L. Di Vona, P. Knauth, Durability of Sulfonated Aromatic Polymers for Proton-Exchange-Membrane Fuel Cells, ChemSusChem. 4 (2011) 1526–1536. https://doi.org/10.1002/cssc.201000415.

[71] T.R. Ralph, D.E. Barnwell, P.J. Bouwman, A.J. Hodgkinson, M.I. Petch, M. Pollington, Reinforced Membrane Durability in Proton Exchange Membrane Fuel Cell Stacks for Automotive Applications, J. Electrochem. Soc. 155 (2008) B411. https://doi.org/10.1149/1.2838163.

[72] T. Holmes, T.J.G. Skalski, M. Adamski, S. Holdcroft, Stability of Hydrocarbon Fuel Cell Membranes: Reaction of Hydroxyl Radicals with Sulfonated Phenylated Polyphenylenes, Chem. Mater. 31 (2019) 1441–1449. https://doi.org/10.1021/acs.chemmater.8b05302.

[73] G. Maier, J. Meier-Haack, Sulfonated Aromatic Polymers for Fuel Cell Membranes, in: G.G. Scherer (Ed.), Fuel Cells II, Springer, Berlin, Heidelberg, 2008: pp. 1–62. https://doi.org/10.1007/12_2008_135.

[74] A.J. Berresheim, M. Müller, K. Müllen, Polyphenylene Nanostructures, Chem. Rev. 99 (1999) 1747–1786. https://doi.org/10.1021/cr970073+.

[75] E.M.W. Tsang, Z. Zhang, A.C.C. Yang, Z. Shi, T.J. Peckham, R. Narimani, B.J. Frisken, S. Holdcroft, Nanostructure, Morphology, and Properties of Fluorous Copolymers Bearing Ionic Grafts, Macromolecules. 42 (2009) 9467–9480. https://doi.org/10.1021/ma901740f.

[76] T. Soboleva, X. Zhao, K. Malek, Z. Xie, T. Navessin, S. Holdcroft, On the micro-, meso-, and macroporous structures of polymer electrolyte membrane fuel cell catalyst layers, ACS Appl. Mater. Interfaces. 2 (2010) 375–384. https://doi.org/10.1021/am900600y.

[77] N. Zamel, The catalyst layer and its dimensionality – A look into its ingredients and how to characterize their effects, J. Power Sources. 309 (2016) 141–159. https://doi.org/10.1016/j.jpowsour.2016.01.091.

[78] E. Antolini, Review in Applied Electrochemistry. Number 54 Recent Developments in Polymer Electrolyte Fuel Cell Electrodes, J. Appl. Electrochem. 34 (2004) 563–576. https://doi.org/10.1023/B:JACH.0000021923.67264.bb.

[79] K.C. Neyerlin, W. Gu, J. Jorne, H.A. Gasteiger, Determination of Catalyst Unique Parameters for the Oxygen Reduction Reaction in a PEMFC, J. Electrochem. Soc. 153 (2006) A1955. https://doi.org/10.1149/1.2266294.

[80] H.A. Gasteiger, S.S. Kocha, B. Sompalli, F.T. Wagner, Activity benchmarks and requirements for Pt, Pt-alloy, and non-Pt oxygen reduction catalysts for PEMFCs, Appl. Catal. B Environ. 56 (2005) 9–35. https://doi.org/10.1016/j.apcatb.2004.06.021.

[81] S. Gottesfeld, Some Observations on the Oxygen Reduction Reaction (ORR) At Platinum Catalysts based on Post Year 2000 Reports, ECS Trans. 6 (2008) 51. https://doi.org/10.1149/1.2943224.

[82] M. Adachi, T. Romero, T. Navessin, Z. Xie, Z. Shi, W. Mérida, S. Holdcroft, Water Permeation Through Catalyst-Coated Membranes, Electrochem. Solid-State Lett. 13 (2010) B51–B54. https://doi.org/10.1149/1.3357339.

[83] T.-H. Kim, J.H. Yoo, T. Maiyalagan, S.-C. Yi, Influence of the Nafion agglomerate morphology on the water-uptake behavior and fuel cell performance in the proton exchange membrane fuel cells, Appl. Surf. Sci. 481 (2019) 777–784. https://doi.org/10.1016/j.apsusc.2019.03.113.

[84] E. Passalacqua, F. Lufrano, G. Squadrito, A. Patti, L. Giorgi, Nafion content in the catalyst layer of polymer electrolyte fuel cells: Effects on structure and performance, Electrochimica Acta. 46 (2001) 799–805. https://doi.org/10.1016/S0013-4686(00)00679-4.

[85] D. Lee, S. Hwang, Effect of loading and distributions of Nafion ionomer in the catalyst layer for PEMFCs, Int. J. Hydrog. Energy. 33 (2008) 2790–2794. https://doi.org/10.1016/j.ijhydene.2008.03.046.

[86] C.-M. Lai, J.-C. Lin, F.-P. Ting, S.-D. Chyou, K.-L. Hsueh, Contribution of Nafion loading to the activity of catalysts and the performance of PEMFC, Int. J. Hydrog. Energy. 33 (2008) 4132–4137. https://doi.org/10.1016/j.ijhydene.2008.05.074.

[87] S. Jeon, J. Lee, G.M. Rios, H.-J. Kim, S.-Y. Lee, E. Cho, T.-H. Lim, J. Hyun Jang, Effect of ionomer content and relative humidity on polymer electrolyte membrane fuel cell (PEMFC) performance of membrane-electrode assemblies (MEAs)

prepared by decal transfer method, Int. J. Hydrog. Energy. 35 (2010) 9678–9686. https://doi.org/10.1016/j.ijhydene.2010.06.044.

[88] K.-H. Kim, K.-Y. Lee, H.-J. Kim, E. Cho, S.-Y. Lee, T.-H. Lim, S.P. Yoon, I.C. Hwang, J.H. Jang, The effects of Nafion® ionomer content in PEMFC MEAs prepared by a catalyst-coated membrane (CCM) spraying method, Int. J. Hydrog. Energy. 35 (2010) 2119–2126. https://doi.org/10.1016/j.ijhydene.2009.11.058.

[89] A. Velázquez-Palenzuela, F. Centellas, E. Brillas, C. Arias, R.M. Rodríguez, J.A. Garrido, P.-L. Cabot, Kinetic effect of the ionomer on the oxygen reduction in carbon-supported Pt electrocatalysts, Int. J. Hydrog. Energy. 37 (2012) 17828–17836. https://doi.org/10.1016/j.ijhydene.2012.09.090.

[90] S.H. Ahn, S. Jeon, H.-Y. Park, S.-K. Kim, H.-J. Kim, E. Cho, D. Henkensmeier, S.J. Yoo, S.W. Nam, T.-H. Lim, J.H. Jang, Effects of platinum loading on the performance of proton exchange membrane fuel cells with high ionomer content in catalyst layers, Int. J. Hydrog. Energy. 38 (2013) 9826–9834. https://doi.org/10.1016/j.ijhydene.2013.05.123.

[91] T. Suzuki, S. Tsushima, S. Hirai, Effects of Nafion® ionomer and carbon particles on structure formation in a proton-exchange membrane fuel cell catalyst layer fabricated by the decal-transfer method, Int. J. Hydrog. Energy. 36 (2011) 12361–12369. https://doi.org/10.1016/j.ijhydene.2011.06.090.

[92] G.-Y. Chen, C. Wang, Y.-J. Lei, J. Zhang, Z. Mao, Z.-Q. Mao, J.-W. Guo, J. Li, M. Ouyang, Gradient design of Pt/C ratio and Nafion content in cathode catalyst layer of PEMFCs, Int. J. Hydrog. Energy. 42 (2017) 29960–29965. https://doi.org/10.1016/j.ijhydene.2017.06.229.

[93] S.-J. Shin, J.-K. Lee, H.-Y. Ha, S.-A. Hong, H.-S. Chun, I.-H. Oh, Effect of the catalytic ink preparation method on the performance of polymer electrolyte membrane fuel cells, J. Power Sources. 106 (2002) 146–152. https://doi.org/10.1016/S0378-7753(01)01045-X.

[94] T.-H. Yang, Y.-G. Yoon, G.-G. Park, W.-Y. Lee, C.-S. Kim, Fabrication of a thin catalyst layer using organic solvents, J. Power Sources. 127 (2004) 230–233. https://doi.org/10.1016/j.jpowsour.2003.09.018.

[95] J.-H. Kim, H.Y. Ha, I.-H. Oh, S.-A. Hong, H.-I. Lee, Influence of the solvent in anode catalyst ink on the performance of a direct methanol fuel cell, J. Power Sources. 135 (2004) 29–35. https://doi.org/10.1016/j.jpowsour.2004.03.058.

[96] R. Fernández, P. Ferreira-Aparicio, L. Daza, PEMFC electrode preparation: Influence of the solvent composition and evaporation rate on the catalytic layer microstructure, J. Power Sources. 151 (2005) 18–24. https://doi.org/10.1016/j.jpowsour.2005.02.048.

[97] M. Chisaka, H. Daiguji, Effect of Organic Solvents on Catalyst Layer Structure in Polymer Electrolyte Membrane Fuel Cells, J. Electrochem. Soc. 156 (2008) B22. https://doi.org/10.1149/1.3000592.

[98] A. Therdthianwong, P. Ekdharmasuit, S. Therdthianwong, Fabrication and Performance of Membrane Electrode Assembly Prepared by a Catalyst-Coated Membrane Method: Effect of Solvents Used in a Catalyst Ink Mixture, Energy Fuels. 24 (2010) 1191–1196. https://doi.org/10.1021/ef901105k.

[99] T.T. Ngo, T.L. Yu, H.-L. Lin, Nafion-based membrane electrode assemblies prepared from catalyst inks containing alcohol/water solvent mixtures, J. Power Sources. Complete (2013) 1–10. https://doi.org/10.1016/j.jpowsour.2013.03.055.

[100] W. Wang, S. Chen, J. Li, W. Wang, Fabrication of catalyst coated membrane with screen printing method in a proton exchange membrane fuel cell, Int. J. Hydrog. Energy. 40 (2015) 4649–4658. https://doi.org/10.1016/j.ijhydene.2015.02.027.

[101] Y.S. Kim, C.F. Welch, N.H. Mack, R.P. Hjelm, E.B. Orler, M.E. Hawley, K.S. Lee, S.-D. Yim, C.M. Johnston, Highly durable fuel cell electrodes based on ionomers dispersed in glycerol, Phys. Chem. Chem. Phys. 16 (2014) 5927–5932. https://doi.org/10.1039/C4CP00496E.

[102] The Effect of Cathode Structures on Nafion Membrane Durability - IOPscience, (n.d.). https://iopscience.iop.org/article/10.1149/2.0151412jes (accessed March 10, 2020).

[103] T.-H. Kim, J.-Y. Yi, C.-Y. Jung, E. Jeong, S.-C. Yi, Solvent effect on the Nafion agglomerate morphology in the catalyst layer of the proton exchange membrane fuel cells, Int. J. Hydrog. Energy. 42 (2017) 478–485. https://doi.org/10.1016/j.ijhydene.2016.12.015.

[104] T. Suzuki, T. Koyama, S. Tsushima, Analysis of Ionomer Distribution in Catalyst Layers by Two-Stage Ion-Beam Processing, ECS Trans. 80 (2017) 419. https://doi.org/10.1149/08008.0419ecst.

[105] Experimental analysis of PEM fuel cell performance using lung channel design bipolar plate: International Journal of Green Energy: Vol 16, No 15, (n.d.). https://www.tandfonline.com/doi/abs/10.1080/15435075.2019.1677238?src=recsys&journalCode=ljge20 (accessed March 10, 2020).

[106] T.E. Springer, T.A. Zawodzinski, S. Gottesfeld, Polymer Electrolyte Fuel Cell Model, J. Electrochem. Soc. 138 (1991) 2334. https://doi.org/10.1149/1.2085971.

[107] M. Saito, K. Hayamizu, T. Okada, Temperature Dependence of Ion and Water Transport in Perfluorinated Ionomer Membranes for Fuel Cells, J. Phys. Chem. B. 109 (2005) 3112–3119. https://doi.org/10.1021/jp045624w.

[108] K.D. Kreuer, W. Weppner, A. Rabenau, Investigation of proton-conducting solids, Solid State Ion. 3–4 (1981) 353–358. https://doi.org/10.1016/0167-2738(81)90112-0.

[109] G. Alberti, R. Narducci, M. Sganappa, Effects of hydrothermal/thermal treatments on the water-uptake of Nafion membranes and relations with changes of conformation, counter-elastic force and tensile modulus of the matrix, J. Power Sources. 178 (2008) 575–583. https://doi.org/10.1016/j.jpowsour.2007.09.034.

[110] K. Kidena, T. Ohkubo, N. Takimoto, A. Ohira, PFG-NMR approach to determining the water transport mechanism in polymer electrolyte membranes conditioned at different temperatures, Eur. Polym. J. 46 (2010) 450–455. https://doi.org/10.1016/j.eurpolymj.2009.12.012.

[111] Mechanical properties and microstructure changes of proton exchange membrane under immersed conditions - Shi - 2014 - Polymer Engineering & Science - Wiley Online Library, (n.d.). https://onlinelibrary-wiley-com.proxy.lib.sfu.ca/doi/full/10.1002/pen.23770 (accessed August 22, 2020).

[112] F.M. Collette, F. Thominette, H. Mendil-Jakani, G. Gebel, Structure and transport properties of solution-cast Nafion® membranes subjected to hygrothermal aging, J. Membr. Sci. 435 (2013) 242–252. https://doi.org/10.1016/j.memsci.2013.02.002.

[113] W. Wagner, A. Pruss, International Equations for the Saturation Properties of Ordinary Water Substance. Revised According to the International Temperature Scale of 1990. Addendum to J. Phys. Chem. Ref. Data 16, 893 (1987), J. Phys. Chem. Ref. Data. 22 (1993) 783–787. https://doi.org/10.1063/1.555926.

[114] R. Vetter, J.O. Schumacher, Experimental parameter uncertainty in proton exchange membrane fuel cell modeling. Part I: Scatter in material parameterization, J. Power Sources. 438 (2019) 227018. https://doi.org/10.1016/j.jpowsour.2019.227018.

[115] P. Futerko, I.-M. Hsing, Thermodynamics of Water Vapor Uptake in Perfluorosulfonic Acid Membranes, J. Electrochem. Soc. 146 (1999) 2049. https://doi.org/10.1149/1.1391890.

[116] A. Morin, G. Gebel, L. Porcar, Z. Peng, N. Martinez, A. Guillermo, S. Lyonnard, Quantitative Multi-Scale Operando Diagnosis of Water Localization inside a Fuel Cell, J. Electrochem. Soc. 164 (2016) F9. https://doi.org/10.1149/2.1401614jes.

[117] P. Choi, N.H. Jalani, R. Datta, Thermodynamics and proton transport in Nafion I. Membrane swelling, sorption, and ion-exchange equilibrium, J. Electrochem. Soc. 152 (2005) E84–E89. https://doi.org/10.1149/1.1855872.

[118] A. Kusoglu, B.L. Kienitz, A.Z. Weber, Understanding the effects of compression and constraints on water uptake of fuel-cell membranes, J. Electrochem. Soc. 158 (2011) B1504–B1514. https://doi.org/10.1149/2.097112jes.

[119] T. Thampan, S. Malhotra, H. Tang, R. Datta, Modeling of conductive transport in proton-exchange membranes for fuel cells, J. Electrochem. Soc. 147 (2000) 3242–3250. https://doi.org/10.1149/1.1393890.

[120] H. Takata, N. Mizuno, M. Nishikawa, S. Fukada, M. Yoshitake, Adsorption properties of water vapor on sulfonated perfluoropolymer membranes, Int. J. Hydrog. Energy. 32 (2007) 371–379. https://doi.org/10.1016/j.ijhydene.2006.09.041.

[121] C. Yang, S. Srinivasan, A.B. Bocarsly, S. Tulyani, J.B. Benziger, A comparison of physical properties and fuel cell performance of Nafion and zirconium phosphate/Nafion composite membranes, J. Membr. Sci. 237 (2004) 145–161.

https://doi.org/10.1016/j.memsci.2004.03.009.

[122] P. Choi, R. Datta, Sorption in proton-exchange membranes. An explanation of Schroeder's paradox, J. Electrochem. Soc. 150 (2003) E601–E607. https://doi.org/10.1149/1.1623495.

[123] A. Kusoglu, M.H. Santare, A.M. Karlsson, Mechanics-based model for non-affine swelling in perfluorosulfonic acid (PFSA) membranes, Polymer. 50 (2009) 2481–2491. https://doi.org/10.1016/j.polymer.2009.03.045.

[124] Y. Zheng, U. Ash, R.P. Pandey, A.G. Ozioko, J. Ponce-González, M. Handl, T. Weissbach, J.R. Varcoe, S. Holdcroft, M.W. Liberatore, R. Hiesgen, D.R. Dekel, Water Uptake Study of Anion Exchange Membranes, Macromolecules. 51 (2018) 3264–3278. https://doi.org/10.1021/acs.macromol.8b00034.

[125] M. Adamski, T.J.G. Skalski, E.M. Schibli, M. Killer, Y. Wu, N. Peressin, B.J. Frisken, S. Holdcroft, Molecular branching as a simple approach to improving polymer electrolyte membranes, J. Membr. Sci. 595 (2020) 117539. https://doi.org/10.1016/j.memsci.2019.117539.

[126] Y. Wu, M. Adamski, H.-F. Lee, S. Holdcroft, Water transport through hydrocarbon-based proton exchange membranes, J. Membr. Sci. (2020) 118276. https://doi.org/10.1016/j.memsci.2020.118276.

[127] V. Detallante, D. Langevin, C. Chappey, M. Métayer, R. Mercier, M. Pinéri, Water vapor sorption in naphthalenic sulfonated polyimide membranes, J. Membr. Sci. 190 (2001) 227–241. https://doi.org/10.1016/S0376-7388(01)00437-9.

[128] D. Stoica, F. Alloin, S. Marais, D. Langevin, C. Chappey, P. Judeinstein, Polyepichlorhydrin Membranes for Alkaline Fuel Cells: Sorption and Conduction Properties, J. Phys. Chem. B. 112 (2008) 12338–12346. https://doi.org/10.1021/jp804787x.

[129] K. Fatyeyeva, C. Chappey, F. Poncin-Epaillard, D. Langevin, J.-M. Valleton, S. Marais, Composite membranes based on Nafion® and plasma treated clay charges: Elaboration and water sorption investigations, J. Membr. Sci. 369 (2011) 155–166. https://doi.org/10.1016/j.memsci.2010.11.062.

[130] B. Mecheri, V. Felice, Z. Zhang, A. D'Epifanio, S. Licoccia, A.C. Tavares, DSC and DVS Investigation of Water Mobility in Nafion/Zeolite Composite Membranes for Fuel Cell Applications, J. Phys. Chem. C. 116 (2012) 20820–20829. https://doi.org/10.1021/jp301762h.

[131] S. Alix, E. Philippe, A. Bessadok, L. Lebrun, C. Morvan, S. Marais, Effect of chemical treatments on water sorption and mechanical properties of flax fibres., Bioresour. Technol. 100 (2009) 4742–4749. https://doi.org/10.1016/j.biortech.2009.04.067.

[132] L. Maldonado, J.-C. Perrin, J. Dillet, O. Lottin, Characterization of polymer electrolyte Nafion membranes: Influence of temperature, heat treatment and drying protocol on sorption and transport properties, J. Membr. Sci. 389 (2012) 43–56.

https://doi.org/10.1016/j.memsci.2011.10.014.

[133] J.T. Hinatsu, M. Mizuhata, H. Takenaka, Water Uptake of Perfluorosulfonic Acid Membranes from Liquid Water and Water Vapor, J. Electrochem. Soc. 141 (1994) 1493. https://doi.org/10.1149/1.2054951.

[134] S. Shi, A.Z. Weber, A. Kusoglu, Structure/property relationship of Nafion XL composite membranes, J. Membr. Sci. 516 (2016) 123–134. https://doi.org/10.1016/j.memsci.2016.06.004.

[135] K.-D. Kreuer, The role of internal pressure for the hydration and transport properties of ionomers and polyelectrolytes, Solid State Ion. 252 (2013) 93–101. https://doi.org/10.1016/j.ssi.2013.04.018.

[136] C.K. Mittelsteadt, J. Staser, Simultaneous Water Uptake, Diffusivity and Permeability Measurement of Perfluorinated Sulfonic Acid Polymer Electrolyte Membranes, ECS Trans. 41 (2011) 101. https://doi.org/10.1149/1.3635547.

[137] F.M. Collette, C. Lorentz, G. Gebel, F. Thominette, Hygrothermal aging of Nafion®, J. Membr. Sci. 330 (2009) 21–29. https://doi.org/10.1016/j.memsci.2008.11.048.

[138] T.A.Z. Jr, C. Derouin, S. Radzinski, R.J. Sherman, V.T. Smith, T.E. Springer, S. Gottesfeld, Water Uptake by and Transport Through Nafion® 117 Membranes, J. Electrochem. Soc. 140 (1993) 1041. https://doi.org/10.1149/1.2056194.

[139] A. Kusoglu, S. Savagatrup, K.T. Clark, A.Z. Weber, Role of Mechanical Factors in Controlling the Structure–Function Relationship of PFSA Ionomers, Macromolecules. 45 (2012) 7467–7476. https://doi.org/10.1021/ma301419s.

[140] S.Y. Kim, M.J. Park, N.P. Balsara, A. Jackson, Confinement Effects on Watery Domains in Hydrated Block Copolymer Electrolyte Membranes, Macromolecules. 43 (2010) 8128–8135. https://doi.org/10.1021/ma101620k.

[141] M.J. Park, N.P. Balsara, A. Jackson, Order−Disorder Transitions in Block Copolymer Electrolytes at Equilibrium with Humid Air, Macromolecules. 42 (2009) 6808–6815. https://doi.org/10.1021/ma901073y.

[142] P. von Schroeder, Über Erstarrungs- und Quellugserscheinungen von Gelatine, Z. Für Phys. Chem. 45U (1903) 75–117. https://doi.org/10.1515/zpch-1903-4503.

[143] G. Alberti, R. Narducci, Evolution of Permanent Deformations (or Memory) in Nafion 117 Membranes with Changes in Temperature, Relative Humidity and Time, and Its Importance in the Development of Medium Temperature PEMFCs, Fuel Cells. 9 (2009) 410–420. https://doi.org/10.1002/fuce.200800148.

[144] M. Bass, V. Freger, Hydration of Nafion and Dowex in liquid and vapor environment: Schroeder's paradox and microstructure, Polymer. 49 (2008) 497–506. https://doi.org/10.1016/j.polymer.2007.11.054.

[145] Water−Nafion Equilibria. Absence of Schroeder's Paradox | The Journal of Physical Chemistry B, (n.d.). https://pubs-acs-

org.proxy.lib.sfu.ca/doi/abs/10.1021/jp073242v (accessed August 30, 2020).

[146] V. Freger, Hydration of Ionomers and Schroeder's Paradox in Nafion, J. Phys. Chem. B. 113 (2009) 24–36. https://doi.org/10.1021/jp806326a.

[147] M. Bass, A. Berman, A. Singh, O. Konovalov, V. Freger, Surface Structure of Nafion in Vapor and Liquid, J. Phys. Chem. B. 114 (2010) 3784–3790. https://doi.org/10.1021/jp9113128.

[148] M. Bass, A. Berman, A. Singh, O. Konovalov, V. Freger, Surface-Induced Micelle Orientation in Nafion Films, Macromolecules. 44 (2011) 2893–2899. https://doi.org/10.1021/ma102361f.

[149] T.A. Zawodzinski, S. Gottesfeld, S. Shoichet, T.J. McCarthy, The contact angle between water and the surface of perfluorosulphonic acid membranes, J. Appl. Electrochem. 23 (1993) 86–88. https://doi.org/10.1007/BF00241582.

[150] S. Goswami, S. Klaus, J. Benziger, Wetting and Absorption of Water Drops on Nafion Films, Langmuir. 24 (2008) 8627–8633. https://doi.org/10.1021/la800799a.

[151] J. Tang, W. Yuan, J. Zhang, H. Li, Y. Zhang, Evidence for a crystallite-rich skin on perfluorosulfonate ionomer membranes, RSC Adv. 3 (2013) 8947–8952. https://doi.org/10.1039/C3RA40430G.

[152] N.J. Economou, A.M. Barnes, A.J. Wheat, M.S. Schaberg, S.J. Hamrock, S.K. Buratto, Investigation of Humidity Dependent Surface Morphology and Proton Conduction in Multi-Acid Side Chain Membranes by Conductive Probe Atomic Force Microscopy, J. Phys. Chem. B. 119 (2015) 14280–14287. https://doi.org/10.1021/acs.jpcb.5b07255.

[153] Characterization of Surface Ionic Activity of Proton Conductive Membranes by Conductive Atomic Force Microscopy - IOPscience, (n.d.). https://iopscience-iop-org.proxy.lib.sfu.ca/article/10.1149/1.2154328/meta (accessed August 30, 2020).

[154] E. Aleksandrova, R. Hiesgen, D. Eberhard, K.A. Friedrich, T. Kaz, E. Roduner, Proton Conductivity Study of a Fuel Cell Membrane with Nanoscale Resolution, ChemPhysChem. 8 (2007) 519–522. https://doi.org/10.1002/cphc.200600704.

[155] H. Noguchi, K. Taneda, H. Minowa, H. Naohara, K. Uosaki, Humidity-Dependent Structure of Surface Water on Perfluorosulfonated Ionomer Thin Film Studied by Sum Frequency Generation Spectroscopy, J. Phys. Chem. C. 114 (2010) 3958–3961. https://doi.org/10.1021/jp907194k.

[156] R. Hiesgen, T. Morawietz, M. Handl, M. Corasaniti, K.A. Friedrich, Atomic Force Microscopy on Cross Sections of Fuel Cell Membranes, Electrodes, and Membrane Electrode Assemblies, Electrochimica Acta. 162 (2015) 86–99. https://doi.org/10.1016/j.electacta.2014.11.122.

[157] Q. He, A. Kusoglu, I.T. Lucas, K. Clark, A.Z. Weber, R. Kostecki, Correlating Humidity-Dependent Ionically Conductive Surface Area with Transport Phenomena in Proton-Exchange Membranes, J. Phys. Chem. B. 115 (2011) 11650–11657.

https://doi.org/10.1021/jp206154y.

[158] E. Aleksandrova, R. Hiesgen, K.A. Friedrich, E. Roduner, Electrochemical atomic force microscopy study of proton conductivity in a Nafion membrane, Phys. Chem. Chem. Phys. 9 (2007) 2735–2743. https://doi.org/10.1039/B617516C.

[159] O. Kwon, Y. Kang, S. Wu, D.-M. Zhu, Characteristics of Microscopic Proton Current Flow Distributions in Fresh and Aged Nafion Membranes, J. Phys. Chem. B. 114 (2010) 5365–5370. https://doi.org/10.1021/jp911182q.

[160] R. O'Hayre, G. Feng, W.D. Nix, F.B. Prinz, Quantitative impedance measurement using atomic force microscopy, J. Appl. Phys. 96 (2004) 3540–3549. https://doi.org/10.1063/1.1778217.

[161] D.A. Bussian, J.R. O'Dea, H. Metiu, S.K. Buratto, Nanoscale Current Imaging of the Conducting Channels in Proton Exchange Membrane Fuel Cells, Nano Lett. 7 (2007) 227–232. https://doi.org/10.1021/nl061170y.

[162] D. Novitski, S. Holdcroft, Determination of O2 Mass Transport at the Pt | PFSA Ionomer Interface under Reduced Relative Humidity, ACS Appl. Mater. Interfaces. 7 (2015) 27314–27323. https://doi.org/10.1021/acsami.5b08720.

[163] M. Adachi, Proton exchange membrane fuel cells: water permeation through Nafion(R) membranes, Thesis, Department of Chemistry - Simon Fraser University, 2010. http://summit.sfu.ca/item/9977 (accessed May 25, 2019).

[164] X. Luo, A. Wright, T. Weissbach, S. Holdcroft, Water permeation through anion exchange membranes, J. Power Sources. 375 (2018) 442–451. https://doi.org/10.1016/j.jpowsour.2017.05.030.

[165] X. Luo, S. Holdcroft, Water transport through short side chain perfluorosulfonic acid ionomer membranes, J. Membr. Sci. 520 (2016) 155–165. https://doi.org/10.1016/j.memsci.2016.07.021.

[166] S.C. Yeo, A. Eisenberg, Physical properties and supermolecular structure of perfluorinated ion-containing (nafion) polymers, J. Appl. Polym. Sci. 21 (1977) 875–898. https://doi.org/10.1002/app.1977.070210401.

[167] T. Takamatsu, M. Hashiyama, A. Eisenberg, Sorption phenomena in nafion membranes, J. Appl. Polym. Sci. 24 (1979) 2199–2220. https://doi.org/10.1002/app.1979.070241101.

[168] B. Kientiz, H. Yamada, N. Nonoyama, A.Z. Weber, Interfacial Water Transport Effects in Proton-Exchange Membranes, J. Fuel Cell Sci. Technol. 8 (2010) 011013-011013–7. https://doi.org/10.1115/1.4002398.

[169] D.A. Caulk, A.M. Brenner, S.M. Clapham, A Steady Permeation Method for Measuring Water Transport Properties of Fuel Cell Membranes, J. Electrochem. Soc. 159 (2012) F518. https://doi.org/10.1149/2.016209jes.

[170] L.M. Onishi, J.M. Prausnitz, J. Newman, Steady-State Diffusion Coefficients for

Water in Nafion in the Absence of Inert Gas, J. Electrochem. Soc. 159 (2012) B754. https://doi.org/10.1149/2.114206jes.

[171] N.S. Schneider, D. Rivin, Steady state analysis of water vapor transport in ionomers, Polymer. 51 (2010) 671–678. https://doi.org/10.1016/j.polymer.2009.12.005.

[172] X. Luo, Water permeation through polymer electrolyte membranes, Thesis, Science: Department of Chemistry, 2017. http://summit.sfu.ca/item/17446 (accessed May 25, 2019).

[173] P.M. Mangiagli, C.S. Ewing, K. Xu, Q. Wang, M.A. Hickner, Dynamic Water Uptake of Flexible Ion-Containing Polymer Networks, Fuel Cells. 9 (2009) 432–438. https://doi.org/10.1002/fuce.200800157.

[174] D.J. Burnett, A.R. Garcia, F. Thielmann, Measuring moisture sorption and diffusion kinetics on proton exchange membranes using a gravimetric vapor sorption apparatus, J. Power Sources. 160 (2006) 426–430. https://doi.org/10.1016/j.jpowsour.2005.12.096.

[175] M. Legras, Y. Hirata, Q.T. Nguyen, D. Langevin, M. Métayer, Sorption and diffusion behaviors of water in Nation 117 membranes with different counter ions, Desalination. 147 (2002) 351–357. https://doi.org/10.1016/S0011-9164(02)00608-2.

[176] S. Ge, X. Li, B. Yi, I.-M. Hsing, Absorption, Desorption, and Transport of Water in Polymer Electrolyte Membranes for Fuel Cells, J. Electrochem. Soc. 152 (2005) A1149–A1157. https://doi.org/10.1149/1.1899263.

[177] D. Rivin, C.E. Kendrick, P.W. Gibson, N.S. Schneider, Solubility and transport behavior of water and alcohols in Nafion™, Polymer. 42 (2001) 623–635. https://doi.org/10.1016/S0032-3861(00)00350-5.

[178] S. Ochi, O. Kamishima, J. Mizusaki, J. Kawamura, Investigation of proton diffusion in Nafion®117 membrane by electrical conductivity and NMR, Solid State Ion. 180 (2009) 580–584. https://doi.org/10.1016/j.ssi.2008.12.035.

[179] Q. Zhao, P. Majsztrik, J. Benziger, Diffusion and Interfacial Transport of Water in Nafion, J. Phys. Chem. B. 115 (2011) 2717–2727. https://doi.org/10.1021/jp1112125.

[180] X. Gong, A. Bandis, A. Tao, G. Meresi, Y. Wang, P.T. Inglefield, A.A. Jones, W.-Y. Wen, Self-diffusion of water, ethanol and decafluropentane in perfluorosulfonate ionomer by pulse field gradient NMR, Polymer. 42 (2001) 6485–6492. https://doi.org/10.1016/S0032-3861(01)00119-7.

[181] A. Guillermo, G. Gebel, H. Mendil-Jakani, E. Pinton, NMR and Pulsed Field Gradient NMR Approach of Water Sorption Properties in Nafion at Low Temperature, J. Phys. Chem. B. 113 (2009) 6710–6717. https://doi.org/10.1021/jp8110452.

[182] H.L. Yeager, A. Steck, Cation and Water Diffusion in Nafion Ion Exchange Membranes: Influence of Polymer Structure, J. Electrochem. Soc. 128 (1981) 1880.

https://doi.org/10.1149/1.2127757.

[183] J.-C. Perrin, S. Lyonnard, F. Volino, Quasielastic Neutron Scattering Study of Water Dynamics in Hydrated Nafion Membranes, J. Phys. Chem. C. 111 (2007) 3393–3404. https://doi.org/10.1021/jp065039q.

[184] A.M. Pivovar, B.S. Pivovar, Dynamic Behavior of Water within a Polymer Electrolyte Fuel Cell Membrane at Low Hydration Levels, J. Phys. Chem. B. 109 (2005) 785–793. https://doi.org/10.1021/jp046029x.

[185] J.-C. Perrin, S. Lyonnard, A. Guillermo, P. Levitz, Water dynamics in ionomer membranes by field-cycling NMR relaxometry, Magn. Reson. Imaging. 25 (2007) 501–504. https://doi.org/10.1016/j.mri.2007.01.002.

[186] Editors' Biographies, in: Polym. Energy Storage Deliv. Polyelectrolytes Batter. Fuel Cells, American Chemical Society, 2012: pp. 305–305. https://doi.org/10.1021/bk-2012-1096.ot001.

[187] A. Kusoglu, M.A. Modestino, A. Hexemer, R.A. Segalman, A.Z. Weber, Subsecond Morphological Changes in Nafion during Water Uptake Detected by Small-Angle X-ray Scattering, ACS Macro Lett. 1 (2012) 33–36. https://doi.org/10.1021/mz200015c.

[188] G. Gebel, S. Lyonnard, H. Mendil-Jakani, A. Morin, The kinetics of water sorption in Nafion membranes: a small-angle neutron scattering study, J. Phys. Condens. Matter. 23 (2011) 234107. https://doi.org/10.1088/0953-8984/23/23/234107.

[189] M.-C. Ferrari, J. Catalano, M. Giacinti Baschetti, M.G. De Angelis, G.C. Sarti, FTIR-ATR Study of Water Distribution in a Short-Side-Chain PFSI Membrane, Macromolecules. 45 (2012) 1901–1912. https://doi.org/10.1021/ma202099p.

[190] D.T. Hallinan, M.G. De Angelis, M. Giacinti Baschetti, G.C. Sarti, Y.A. Elabd, Non-Fickian Diffusion of Water in Nafion, Macromolecules. 43 (2010) 4667–4678. https://doi.org/10.1021/ma100047z.

[191] D.T. Hallinan, Y.A. Elabd, Diffusion and Sorption of Methanol and Water in Nafion Using Time-Resolved Fourier Transform Infrared−Attenuated Total Reflectance Spectroscopy, J. Phys. Chem. B. 111 (2007) 13221–13230. https://doi.org/10.1021/jp075178n.

[192] D.T. Hallinan, Y.A. Elabd, Diffusion of Water in Nafion Using Time-Resolved Fourier Transform Infrared−Attenuated Total Reflectance Spectroscopy, J. Phys. Chem. B. 113 (2009) 4257–4266. https://doi.org/10.1021/jp811325v.

[193] T. Peckham, J. Schmeisser, S. Holdcroft, Relationships of Acid and Water Content to Proton Transport in Statistically Sulfonated Proton Exchange Membranes: Variation of Water Content Via Control of Relative Humidity, J. Phys. Chem. B. 112 (2008) 2848–58. https://doi.org/10.1021/jp077218t.

[194] T.J. Peckham, J. Schmeisser, M. Rodgers, S. Holdcroft, Main-chain, statistically sulfonated proton exchange membranes: the relationships of acid concentration

and proton mobility to water content and their effect upon proton conductivity, J. Mater. Chem. 17 (2007) 3255–3268. https://doi.org/10.1039/B702339A.

[195] S. Motupally, A.J. Becker, J.W. Weidner, Diffusion of Water in Nafion 115 Membranes, J. Electrochem. Soc. 147 (2000) 3171. https://doi.org/10.1149/1.1393879.

[196] P. Shao, R.Y.M. Huang, Polymeric membrane pervaporation, J. Membr. Sci. 287 (2007) 162–179. https://doi.org/10.1016/j.memsci.2006.10.043.

[197] N. Zhao, D. Edwards, Z. Shi, S. Holdcroft, Interfacial vs. Internal Water Transport Resistance of Sulfonated Hydrocarbon Proton-Exchange Membranes, ECS Electrochem. Lett. 2 (2013) F22–F24. https://doi.org/10.1149/2.009303eel.

[198] T. Mashio, A. Ohma, K. Shinohara, Advanced In-situ Analysis of Reactant Gas Partial Pressure at Catalyst Layer/PEM Interfaces, ECS Trans. 16 (2008) 1009–1018. https://doi.org/10.1149/1.2981941.

[199] G.S. Hwang, D.Y. Parkinson, A. Kusoglu, A.A. MacDowell, A.Z. Weber, Understanding Water Uptake and Transport in Nafion Using X-ray Microtomography, ACS Macro Lett. 2 (2013) 288–291. https://doi.org/10.1021/mz300651a.

[200] P.W. Majsztrik, M.B. Satterfield, A.B. Bocarsly, J.B. Benziger, Water sorption, desorption and transport in Nafion membranes, J. Membr. Sci. 301 (2007) 93–106. https://doi.org/10.1016/j.memsci.2007.06.022.

[201] A. Kusoglu, A. Kwong, K.T. Clark, H.P. Gunterman, A.Z. Weber, Water Uptake of Fuel-Cell Catalyst Layers, J. Electrochem. Soc. 159 (2012) F530–F535. https://doi.org/10.1149/2.031209jes.

[202] P. Krtil, A. Trojánek, Z. Samec, Kinetics of Water Sorption in NafionThin Films − Quartz Crystal Microbalance Study, J. Phys. Chem. B. 105 (2001) 7979–7983. https://doi.org/10.1021/jp004162t.

[203] M.B. Satterfield, J.B. Benziger, Non-Fickian Water Vapor Sorption Dynamics by Nafion Membranes, J. Phys. Chem. B. 112 (2008) 3693–3704. https://doi.org/10.1021/jp7103243.

[204] A. Kongkanand, Interfacial Water Transport Measurements in Nafion Thin Films Using a Quartz-Crystal Microbalance, J. Phys. Chem. C. 115 (2011) 11318–11325. https://doi.org/10.1021/jp2028214.

[205] S.K. Dishari, M.A. Hickner, Antiplasticization and Water Uptake of Nafion Thin Films, ACS Macro Lett. 1 (2012) 291–295. https://doi.org/10.1021/mz200169a.

[206] J.A. Dura, V.S. Murthi, M. Hartman, S.K. Satija, C.F. Majkrzak, Multilamellar Interface Structures in Nafion, Macromolecules. 42 (2009) 4769–4774. https://doi.org/10.1021/ma802823j.

[207] T. Soboleva, K. Malek, Z. Xie, T. Navessin, S. Holdcroft, PEMFC Catalyst Layers: The Role of Micropores and Mesopores on Water Sorption and Fuel Cell Activity,

(2011). https://doi.org/10.1021/am200590w.

[208] J.J. Conde, M.A. Folgado, P. Ferreira-Aparicio, A.M. Chaparro, A. Chowdhury, A. Kusoglu, D. Cullen, A.Z. Weber, Mass-transport properties of electrosprayed Pt/C catalyst layers for polymer-electrolyte fuel cells, J. Power Sources. 427 (2019) 250–259. https://doi.org/10.1016/j.jpowsour.2019.04.079.

[209] I.V. Zenyuk, P.K. Das, A.Z. Weber, Understanding Impacts of Catalyst-Layer Thickness on Fuel-Cell Performance via Mathematical Modeling, J. Electrochem. Soc. 163 (2016) F691–F703. https://doi.org/10.1149/2.1161607jes.

[210] M.V. Williams, E. Begg, L. Bonville, H.R. Kunz, J.M. Fenton, Characterization of Gas Diffusion Layers for PEMFC, J. Electrochem. Soc. 151 (2004) A1173–A1180. https://doi.org/10.1149/1.1764779.

[211] K. Sakai, K. Sato, T. Mashio, A. Ohma, K. Yamaguchi, K. Shinohara, Analysis of Reactant Gas Transport in Catalyst Layers; Effect of Pt-loadings, ECS Trans. 25 (2009) 1193–1201. https://doi.org/10.1149/1.3210674.

[212] K. Sato, A. Ohma, K. Yamaguchi, K. Shinohara, Analysis of Water Transport in Catalyst Layers: The Effect of Carbon Supports, ECS Trans. 25 (2009) 273–283. https://doi.org/10.1149/1.3210578.

[213] K. Sato, A. Ohma, K. Yamaguchi, K. Shinohara, Analysis of Water Transport in Catalyst Layers, ECS Trans. 19 (2009) 39–50. https://doi.org/10.1149/1.3242367.

[214] E. Balogun, M. Adamski, S. Holdcroft, Communication—Non-Fluorous, Hydrocarbon PEMFCs, Generating $\greater$ 1 W cm-2 Power, J. Electrochem. Soc. 167 (2020) 084502. https://doi.org/10.1149/1945-7111/ab88bd.

[215] R. Hiesgen, S. Helmly, I. Galm, T. Morawietz, M. Handl, K.A. Friedrich, Microscopic Analysis of Current and Mechanical Properties of Nafion® Studied by Atomic Force Microscopy, Membranes. 2 (2012) 783–803. https://doi.org/10.3390/membranes2040783.

[216] S. Chen, H. Pan, Z. Chang, M. Jin, H. Pu, Synthesis and study of pyridine-containing sulfonated polybenzimidazole multiblock copolymer for proton exchange membrane fuel cells, Ionics. 25 (2019) 2255–2265. https://doi.org/10.1007/s11581-018-2610-7.

[217] B. Huang, X. Wang, H. Fang, S. Jiang, H. Hou, Mechanically strong sulfonated polybenzimidazole PEMs with enhanced proton conductivity, Mater. Lett. 234 (2019) 354–356. https://doi.org/10.1016/j.matlet.2018.09.131.

[218] C.C. de Araujo, K.D. Kreuer, M. Schuster, G. Portale, H. Mendil-Jakani, G. Gebel, J. Maier, Poly(p-phenylene sulfone)s with high ion exchange capacity: ionomers with unique microstructural and transport features, Phys. Chem. Chem. Phys. 11 (2009) 3305–3312. https://doi.org/10.1039/B822069G.

[219] M.L. Disabb-Miller, Y. Zha, A.J. DeCarlo, M. Pawar, G.N. Tew, M.A. Hickner, Water Uptake and Ion Mobility in Cross-Linked Bis(terpyridine)ruthenium-Based Anion

Exchange Membranes, Macromolecules. 46 (2013) 9279–9287. https://doi.org/10.1021/ma401701n.

[220] N. Follain, S. Roualdes, S. Marais, J. Frugier, M. Reinholdt, J. Durand, Water Transport Properties of Plasma-Modified Commercial Anion-Exchange Membrane for Solid Alkaline Fuel Cells, J. Phys. Chem. C. 116 (2012) 8510–8522. https://doi.org/10.1021/jp2109835.

[221] G.S. Park, Transport Principles—Solution, Diffusion and Permeation in Polymer Membranes, in: P.M. Bungay, H.K. Lonsdale, M.N. de Pinho (Eds.), Synth. Membr. Sci. Eng. Appl., Springer Netherlands, Dordrecht, 1986: pp. 57–107. https://doi.org/10.1007/978-94-009-4712-2_3.

[222] Y.S. Kim, B.S. Pivovar, Moving beyond mass-based parameters for conductivity analysis of sulfonated polymers, Annu. Rev. Chem. Biomol. Eng. 1 (2010) 123–148. https://doi.org/10.1146/annurev-chembioeng-073009-101309.

[223] R.S. McLean, M. Doyle, B.B. Sauer, High-Resolution Imaging of Ionic Domains and Crystal Morphology in Ionomers Using AFM Techniques, Macromolecules. 33 (2000) 6541–6550. https://doi.org/10.1021/ma000464h.

[224] H.-F. Lee, Preparation and Evaluation of Polymer Electrolytes for Fuel Cells, Department of Photonic-National Sun Yat-sen University, 2014. etd-0009115-153616 (accessed July 30, 2019).

[225] Y.-C. Huang, R.-H. Tai, H.-F. Lee, P.-H. Wang, R. Gopal, C.-C. Lee, M.-Y. Chang, W.-Y. Huang, Synthesis of Highly Sulfonated Poly(arylene ether) Containing Multiphenyl for Proton Exchange Membrane Materials, Int. J. Polym. Sci. (2016). https://doi.org/10.1155/2016/6545362.

[226] J. Kerres, A. Ullrich, F. Meier, T. Häring, Synthesis and characterization of novel acid–base polymer blends for application in membrane fuel cells, Solid State Ion. 125 (1999) 243–249. https://doi.org/10.1016/S0167-2738(99)00181-2.

[227] J.A. Kerres, Blended and Cross-Linked Ionomer Membranes for Application in Membrane Fuel Cells, Fuel Cells. 5 (2005) 230–247. https://doi.org/10.1002/fuce.200400079.

[228] M.P. Kulkarni, T.J. Peckham, O.D. Thomas, S. Holdcroft, Synthesis of highly sulfonated polybenzimidazoles by direct copolymerization and grafting, J. Polym. Sci. Part Polym. Chem. 51 (2013) 3654–3666. https://doi.org/10.1002/pola.26764.

[229] G. Wang, K.H. Lee, W.H. Lee, D.W. Shin, N.R. Kang, D.H. Cho, D.S. Hwang, Y. Zhuang, Y.M. Lee, M.D. Guiver, Durable Sulfonated Poly(benzothiazole-co-benzimidazole) Proton Exchange Membranes, Macromolecules. 47 (2014) 6355–6364. https://doi.org/10.1021/ma501409v.

[230] D.J. Jones, J. Rozière, Recent advances in the functionalisation of polybenzimidazole and polyetherketone for fuel cell applications, J. Membr. Sci. 185 (2001) 41–58. https://doi.org/10.1016/S0376-7388(00)00633-5.

[231] N. Tan, Y. Chen, G. Xiao, D. Yan, Synthesis and properties of sulfonated polybenzothiazoles with benzimidazole moieties as proton exchange membranes, J. Membr. Sci. 356 (2010) 70–77. https://doi.org/10.1016/j.memsci.2010.03.028.

[232] S. Xu, M. Adamski, M. Killer, E.M. Schibli, B.J. Frisken, S. Holdcroft, Sulfo-Phenylated Polyphenylenes Containing Sterically Hindered Pyridines, Macromolecules. 52 (2019) 2548–2559. https://doi.org/10.1021/acs.macromol.8b02289.

[233] Q. Duan, H. Wang, J. Benziger, Transport of liquid water through Nafion membranes, J. Membr. Sci. 392–393 (2012) 88–94. https://doi.org/10.1016/j.memsci.2011.12.004.

[234] Y. Aoyama, K. Suzuki, Y. Tabe, T. Chikahisa, T. Tanuma, Water Transport and PEFC Performance with Different Interface Structure between Micro-Porous Layer and Catalyst Layer, J. Electrochem. Soc. 163 (2016) F359. https://doi.org/10.1149/2.0451605jes.

[235] S. Jenkins, K.I. Jacob, S. Kumar, The effect of hydrogen bonding on the physical and mechanical properties of rigid-rod polymers, J. Polym. Sci. Part B Polym. Phys. 38 (2000) 3053–3061. https://doi.org/10.1002/1099-0488(20001201)38:23<3053::AID-POLB70>3.0.CO;2-H.

[236] F. Dubelley, E. Planes, C. Bas, E. Pons, B. Yrieix, L. Flandin, Water Vapor Sorption Properties of Polyethylene Terephthalate over a Wide Range of Humidity and Temperature, J. Phys. Chem. B. 121 (2017) 1953–1962. https://doi.org/10.1021/acs.jpcb.6b11700.

[237] J. Savage, Y.-L.S. Tse, G.A. Voth, Proton Transport Mechanism of Perfluorosulfonic Acid Membranes, J. Phys. Chem. C. 118 (2014) 17436–17445. https://doi.org/10.1021/jp504714d.

[238] D.H. Schwarz, N. Djilali, 3D Modeling of Catalyst Layers in PEM Fuel Cells Effects of Transport Limitations, J. Electrochem. Soc. 154 (2007) B1167–B1178. https://doi.org/10.1149/1.2777011.

[239] W. Dai, H. Wang, X.-Z. Yuan, J.J. Martin, D. Yang, J. Qiao, J. Ma, A review on water balance in the membrane electrode assembly of proton exchange membrane fuel cells, Int. J. Hydrog. Energy. 34 (2009) 9461–9478. https://doi.org/10.1016/j.ijhydene.2009.09.017.

[240] A.B.D. Cassie, S. Baxter, Wettability of porous surfaces, Trans. Faraday Soc. 40 (1944) 546–551. https://doi.org/10.1039/TF9444000546.

[241] A. Suzuki, U. Sen, T. Hattori, R. Miura, R. Nagumo, H. Tsuboi, N. Hatakeyama, A. Endou, H. Takaba, M.C. Williams, A. Miyamoto, Ionomer content in the catalyst layer of polymer electrolyte membrane fuel cell (PEMFC): Effects on diffusion and performance, Int. J. Hydrog. Energy. 36 (2011) 2221–2229. https://doi.org/10.1016/j.ijhydene.2010.11.076.

[242] C.W. Monroe, T. Romero, W. Mérida, M. Eikerling, A vaporization-exchange model

for water sorption and flux in Nafion, J. Membr. Sci. 324 (2008) 1–6. https://doi.org/10.1016/j.memsci.2008.05.080.

[243] J.N.L. Albert, T.H. Epps, Self-assembly of block copolymer thin films, Mater. Today. 13 (2010) 24–33. https://doi.org/10.1016/S1369-7021(10)70106-1.

[244] R.A. Segalman, Patterning with block copolymer thin films, Mater. Sci. Eng. R Rep. 48 (2005) 191–226. https://doi.org/10.1016/j.mser.2004.12.003.

[245] Diblock copolymers under confinement, Phys. B Condens. Matter. 213–214 (1995) 22–25. https://doi.org/10.1016/0921-4526(95)00053-C.

[246] E. Huang, T.P. Russell, C. Harrison, P.M. Chaikin, R.A. Register, C.J. Hawker, J. Mays, Using Surface Active Random Copolymers To Control the Domain Orientation in Diblock Copolymer Thin Films, Macromolecules. 31 (1998) 7641–7650. https://doi.org/10.1021/ma980705+.

[247] P. Mansky, T.P. Russell, C.J. Hawker, M. Pitsikalis, J. Mays, Ordered Diblock Copolymer Films on Random Copolymer Brushes, Macromolecules. 30 (1997) 6810–6813. https://doi.org/10.1021/ma970675v.

[248] M.A. Modestino, A. Kusoglu, A. Hexemer, A.Z. Weber, R.A. Segalman, Controlling Nafion Structure and Properties via Wetting Interactions, Macromolecules. 45 (2012) 4681–4688. https://doi.org/10.1021/ma300212f.

[249] A. Kusoglu, D. Kushner, D.K. Paul, K. Karan, M.A. Hickner, A.Z. Weber, Impact of Substrate and Processing on Confinement of Nafion Thin Films, Adv. Funct. Mater. 24 (2014) 4763–4774. https://doi.org/10.1002/adfm.201304311.

[250] D.K. Paul, A. Fraser, K. Karan, Towards the understanding of proton conduction mechanism in PEMFC catalyst layer: Conductivity of adsorbed Nafion films, Electrochem. Commun. 13 (2011) 774–777. https://doi.org/10.1016/j.elecom.2011.04.022.

[251] Z. Siroma, R. Kakitsubo, N. Fujiwara, T. Ioroi, S. Yamazaki, K. Yasuda, Depression of proton conductivity in recast Nafion® film measured on flat substrate, J. Power Sources. 189 (2009) 994–998. https://doi.org/10.1016/j.jpowsour.2008.12.141.

[252] H. Iden, A. Ohma, K. Shinohara, Analysis of Proton Transport in Pseudo Catalyst Layers, J. Electrochem. Soc. 156 (2009) B1078. https://doi.org/10.1149/1.3169514.

[253] H. Iden, K. Sato, A. Ohma, K. Shinohara, Relationship among Microstructure, Ionomer Property and Proton Transport in Pseudo Catalyst Layers, J. Electrochem. Soc. 158 (2011) B987. https://doi.org/10.1149/1.3598141.

[254] A. Ohira, S. Kuroda, H.F. M. Mohamed, B. Tavernier, Effect of interface on surface morphology and proton conduction of polymer electrolyte thin films, Phys. Chem. Chem. Phys. 15 (2013) 11494–11500. https://doi.org/10.1039/C3CP51136G.

[255] M.A. Modestino, D.K. Paul, S. Dishari, S.A. Petrina, F.I. Allen, M.A. Hickner, K. Karan, R.A. Segalman, A.Z. Weber, Self-Assembly and Transport Limitations in

Confined Nafion Films, Macromolecules. 46 (2013) 867–873. https://doi.org/10.1021/ma301999a.

[256] P. Bertoncello, I. Ciani, F. Li, P.R. Unwin, Measurement of Apparent Diffusion Coefficients within Ultrathin Nafion Langmuir−Schaefer Films: Comparison of a Novel Scanning Electrochemical Microscopy Approach with Cyclic Voltammetry, Langmuir. 22 (2006) 10380–10388. https://doi.org/10.1021/la061214i.

[257] S.K. Dishari, M.A. Hickner, Confinement and Proton Transfer in NAFION Thin Films, Macromolecules. 46 (2013) 413–421. https://doi.org/10.1021/ma3011137.

[258] S.A. Eastman, S. Kim, K.A. Page, B.W. Rowe, S. Kang, C.L. Soles, K.G. Yager, Effect of Confinement on Structure, Water Solubility, and Water Transport in Nafion Thin Films, Macromolecules. 45 (2012) 7920–7930. https://doi.org/10.1021/ma301289v.

[259] T. Masuda, F. Sonsudin, P.R. Singh, H. Naohara, K. Uosaki, Potential-Dependent Adsorption and Desorption of Perfluorosulfonated Ionomer on a Platinum Electrode Surface Probed by Electrochemical Quartz Crystal Microbalance and Atomic Force Microscopy, J. Phys. Chem. C. 117 (2013) 15704–15709. https://doi.org/10.1021/jp404376t.

[260] S. Kim, J.A. Dura, K.A. Page, B.W. Rowe, K.G. Yager, H.-J. Lee, C.L. Soles, Surface-Induced Nanostructure and Water Transport of Thin Proton-Conducting Polymer Films, Macromolecules. 46 (2013) 5630–5637. https://doi.org/10.1021/ma400750f.

Appendix A: Supporting information for chapter 3

Table A 1. Sensitivity analysis of the Park model regression for membrane SPAE by setting integer value of n from 1 to 10. The least sum of squared residuals (LSSR) is sensitive to the change in the value of n.

Set value of n	a_L	K_L	K_H	K_A	LSSR[a]	Δ(LSSR)%[b]
1	855.33	2.58E-07	1.06E-03	5.24	0.459	6.31E+03
2	749.31	4.42E-03	1.06E-03	1.72	0.129	1.71E+03
3	2.46	2.91	6.61E-04	2.49	0.0153	114.2
4	4.98	1.18	6.69E-04	2.10	0.0104	45.74
5[c]	9.14	0.58	6.72E-04	1.98	0.0072	0
6	14.60	0.35	6.70E-04	2.11	0.0109	52.12
7	36.20	0.13	6.92E-04	2.26	0.0121	69.62
8	113.86	0.041	7.85E-04	2.65	0.0140	95.58
9	404.48	1.16E-02	9.71E-04	3.33	0.0168	1.34E+02
10	895.06	5.27E-03	1.06E-03	4.35	0.0210	1.93E+02

[a] Least sum of squared residuals (LSSR) for each set value of n in the least-square analysis
[b] Percent change of the least sum of squared residuals against the best fit (n=5). Δ(LSSR)% = 100% x (LSSR-0.0072)/0.0072
[c] the best fit from the global least-square analysis (n=5)

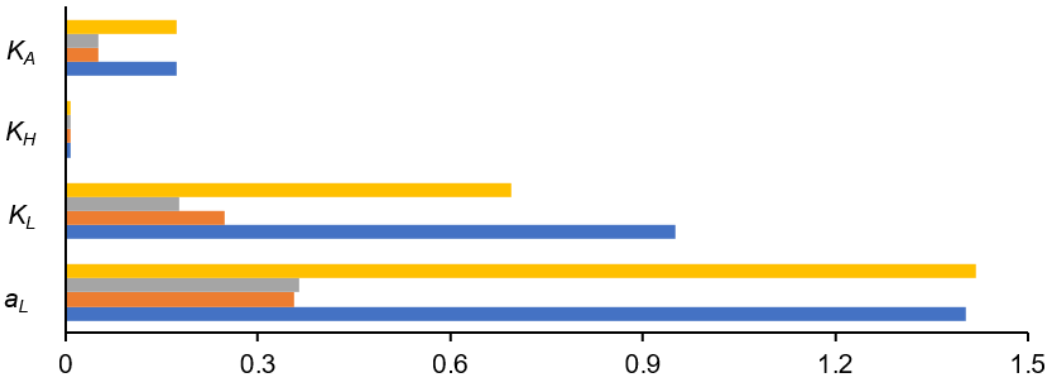

	aL	KL	KH	KA
+20%	1.4200	0.6946	0.007394	0.1721
+10%	0.3644	0.1771	0.007229	0.0502
-10%	0.3563	0.2480	0.007166	0.0508
-20%	1.4039	0.9505	0.007185	0.1732

Least sum of squared residuals

Figure A 1. Parameter sensitivity analysis of the Park model regression for membrane SPAE with the aggregate number (n) set at 5. What-if scenario was run for each parameter change ±10% and ±20% from the best fit: a_L (9.14), K_L (0.58), K_H (0.000672), K_A (1.98). The least sum of squared residuals are listed and graph against to changes in each parameter.

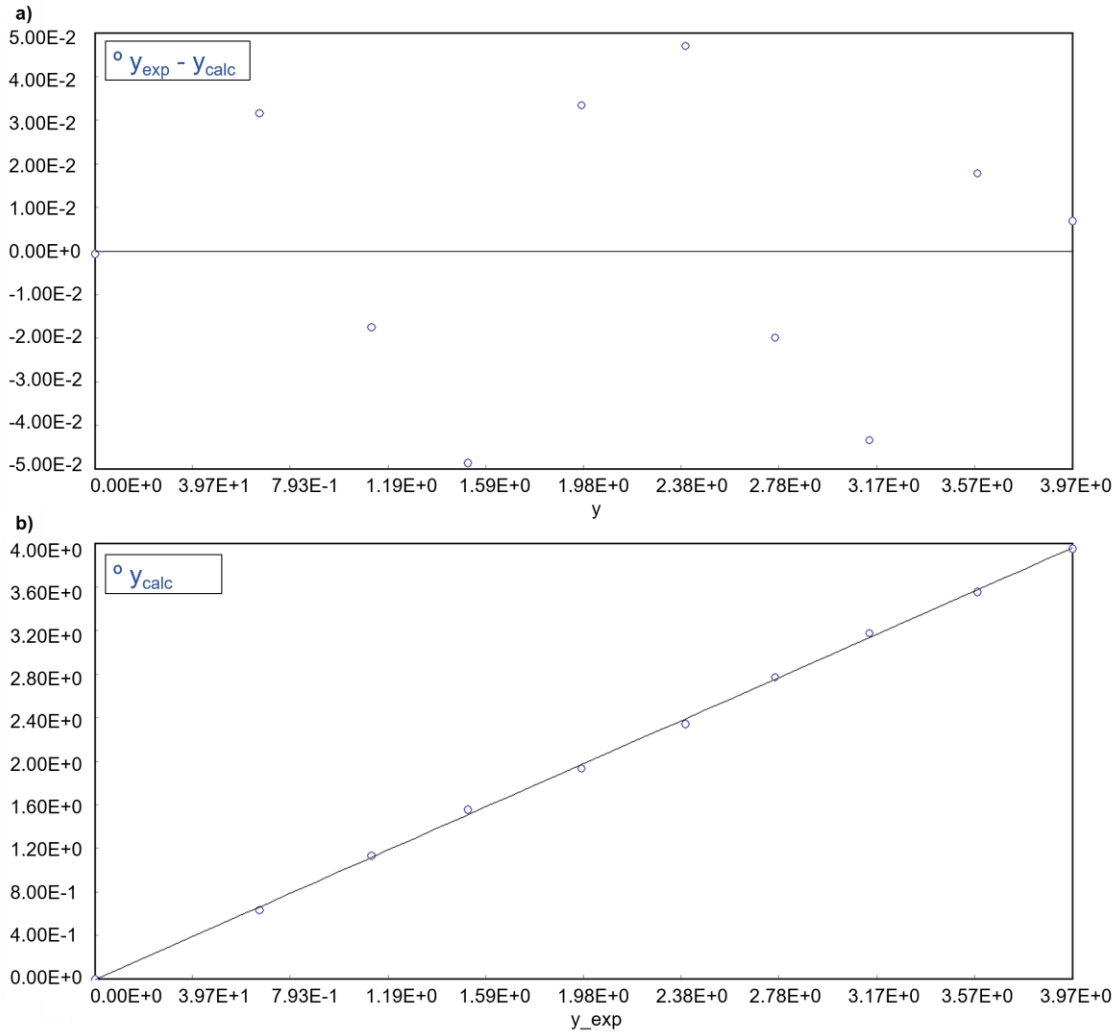

Figure A 2. a) Residual distribution and b) calculation value against experimental value in the Park model approximation for vapor sorption of membrane SPAE at 70 °C.

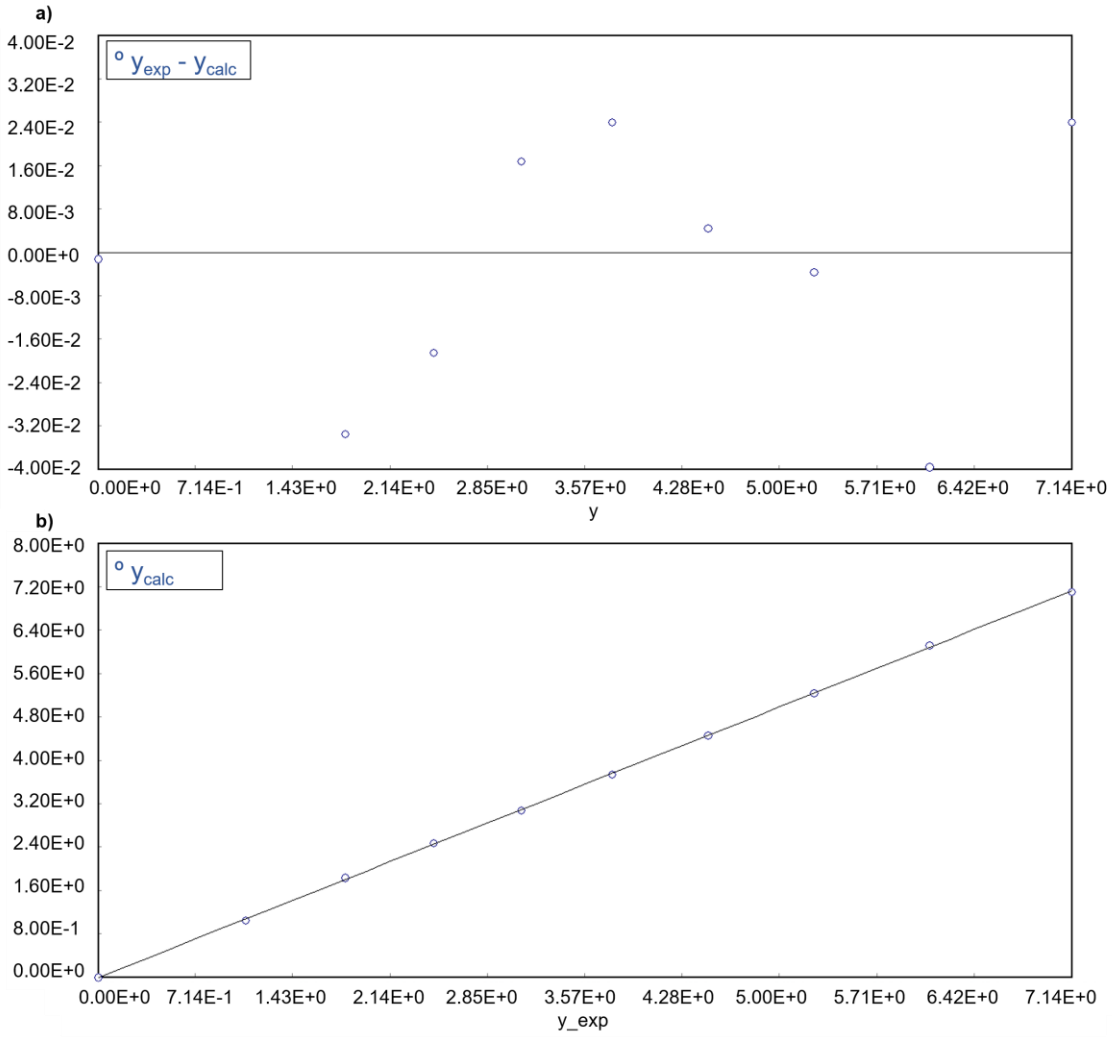

Figure A 3. a) Residual distribution and b) calculation value against experimental value in the Park model approximation for vapor sorption of membrane SPPB at 70 °C.

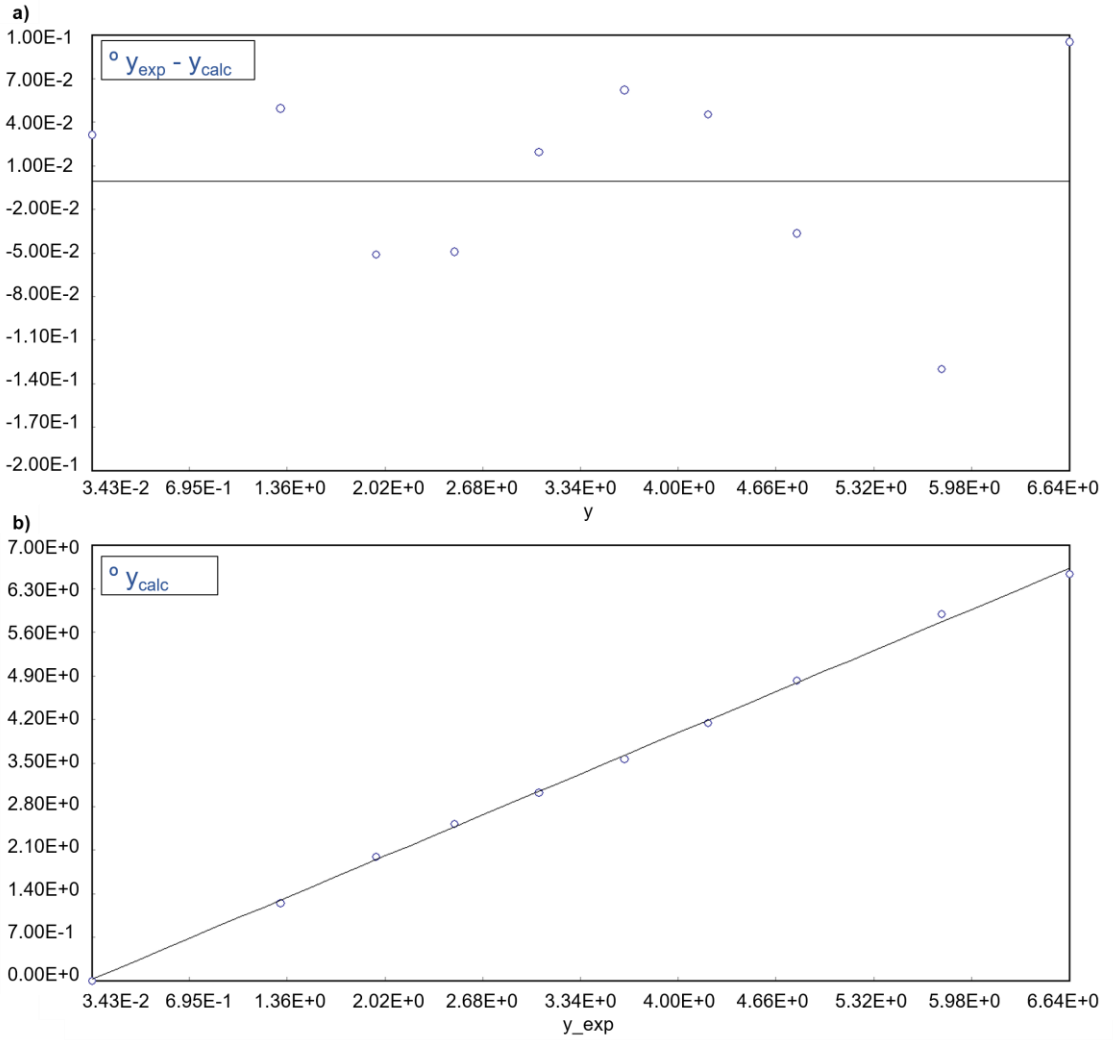

Figure A 4. a) Residual distribution and b) calculation value against experimental value in the Park model approximation for vapor sorption of membrane N211 at 70 °C.

Appendix B: Supporting information for chapter 4

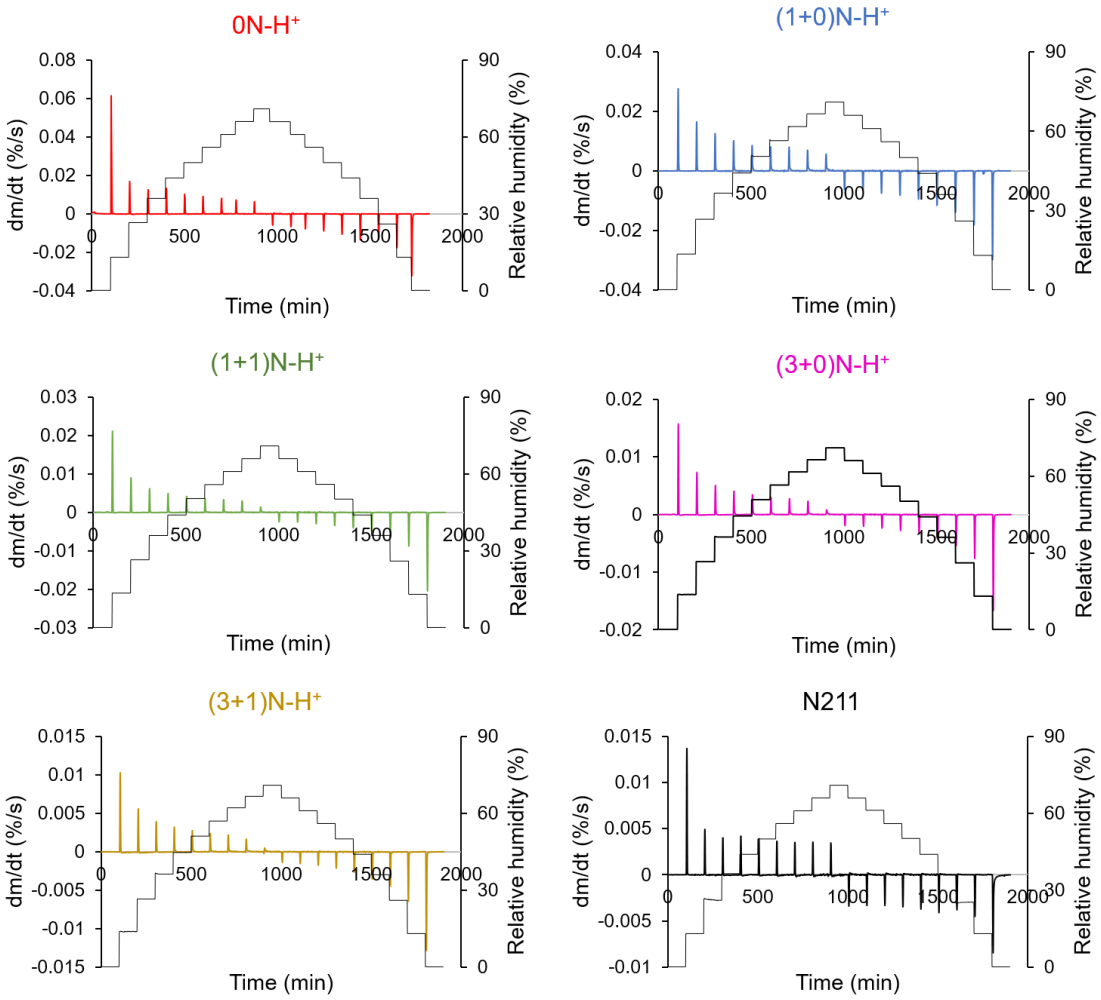

Figure B 1. Time-dependent transient water diffusion of membranes in a full isotherm cycle under 80 ℃, instantaneous mass-change rate (primary axis), dm/dt, and relative humidity steps (secondary axis) over time.

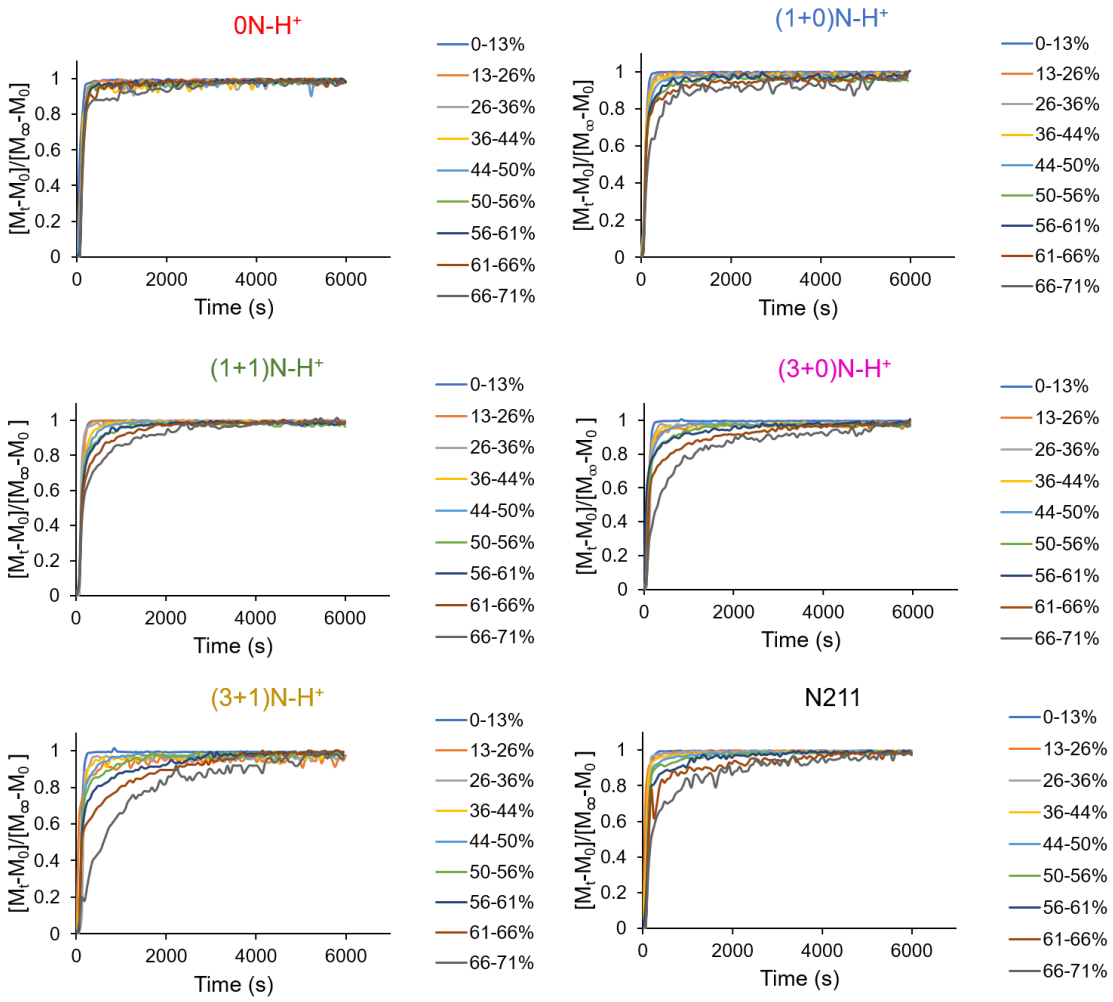

Figure B 2. Normalized water uptake, $[M_t - M_0] / [M_\infty - M_0]$, over time in sorption period under 80 °C.

Table B 2. Effective rate constant of diffusion, k_{sorp}, for membranes under 80 °C

RH range	k_{sorp} (s^{-1})					
	0N	**(1+0)N**	**(1+1)N**	**(3+0)N**	**(3+1)N**	**N211**
0-13%	0.81	0.52	1.3	0.67	0.69	0.71
13-26%	0.56	0.27	0.54	0.29	0.29	0.49
26-36%	0.39	0.12	0.30	0.16	0.17	0.28
36-44%	0.099	0.086	0.19	0.096	0.10	0.14
44-50%	0.077	0.069	0.17	0.065	0.056	0.045
50-56%	0.042	0.051	0.11	0.031	0.018	0.024
56-61%	0.033	0.045	0.061	0.016	0.0079	0.014
61-66%	0.019	0.032	0.026	0.0080	0.0050	0.0082
66-71%	0.0067	0.013	0.018	0.0050	0.0027	0.0053

Table B 3. Transient diffusivity, *D*, for membranes under 80 °C.

RH step	D (cm^2/s)					
	0N [a]	**(1+0)N** [b]	**(1+1)N** [c]	**(3+0)N** [d]	**(3+1)N** [e]	**N211** [f]
0-13%	9.9×10^{-6}	5.3×10^{-6}	5.2×10^{-6}	4.9×10^{-6}	4.7×10^{-6}	4.4×10^{-6}
13-26%	6.9×10^{-6}	2.8×10^{-6}	2.2×10^{-6}	2.1×10^{-6}	2.0×10^{-6}	3.1×10^{-6}
26-36%	4.8×10^{-6}	1.3×10^{-6}	1.2×10^{-6}	1.2×10^{-6}	1.2×10^{-6}	1.8×10^{-6}
36-44%	1.4×10^{-6}	9.4×10^{-7}	7.6×10^{-7}	7.0×10^{-7}	6.8×10^{-7}	8.8×10^{-7}
44-50%	1.0×10^{-6}	8.0×10^{-7}	6.8×10^{-7}	4.8×10^{-7}	3.8×10^{-7}	2.8×10^{-7}
50-56%	8.1×10^{-7}	5.9×10^{-7}	4.4×10^{-7}	2.3×10^{-7}	1.2×10^{-7}	1.5×10^{-7}
56-61%	6.4×10^{-7}	5.2×10^{-7}	2.4×10^{-7}	1.2×10^{-7}	5.3×10^{-8}	8.7×10^{-8}
61-66%	4.1×10^{-7}	3.9×10^{-7}	1.0×10^{-7}	5.8×10^{-8}	3.4×10^{-8}	5.1×10^{-8}
66-71%	1.6×10^{-7}	1.6×10^{-7}	7.2×10^{-8}	3.7×10^{-8}	1.8×10^{-8}	3.3×10^{-8}

[a] thickness at 0-36% RH was 35 μm, 36-50% RH was 37 μm, 50-61% RH was 44 μm, 61-66 % RH was 46 μm, and 66-71 %RH was 49 μm.

[b] thickness at 0-26% RH was 32 μm, 26-44% RH was 33 μm, 44-61% RH was 34 μm, 61-71% RH was 35 μm.

[c] thickness throughout RH range was 20 μm.

[d] thickness throughout RH range was 27 μm.

[e] thickness throughout RH range was 26 μm.

[f] thickness throughout RH range was 25 μm.

Appendix C. Supporting information for chapter 5

Table C 1. Catalyst layer with Nafion D520 ionomer.

For Nafion D520 Ionomer - Percentage mass of solid polymer in dispersion = 5% Nafion					
Percentage Ionomer (%)	Percentage Pt/C (%)	Solid weight Ionomer (g)	Solid weight Pt/C (g)	Pt loading (mg/cm^2)	CL X 2 weight(mg)
30	70	0.5131	1.197	0.4076	12.55
25	75	0.4276	1.282	0.4095	11.77
20	80	0.3421	1.368	0.4076	11.07
15	85	0.2565	1.454	0.4108	10.42
10	90	0.171	1.539	0.4065	9.734

Table C 2. Catalyst layer with SPPB ionomer.

For SPPB Ionomer - Percentage mass of solid polymer in dispersion = 3% SPPB					
Percentage Ionomer (%)	Percentage Pt/C (%)	Solid weight Ionomer (g)	Solid weight Pt/C (g)	Pt loading (mg/cm^2)	CL X 2 weight(mg)
30	70	0.5131	1.197	0.4049	12.47
25	75	0.4276	1.282	0.4077	11.72
20	80	0.3421	1.368	0.4061	10.94
15	85	0.2565	1.454	0.4112	10.42
10	90	0.171	1.539	0.4058	9.717

Table C 3. Molar water fluxes (mol m^{-2} s^{-1}) through membrane electrode assembly with catalyst layer composed of ionomer SPPB in liquid-vapor permeation at 80 °C.

	30% RH	50% RH	70% RH	90% RH
N211	0.183 ± 0.014	0.107 ± 0.015	0.077 ± 0.012	0.029 ± 0.003
$hCCM_d$	0.185 ± 0.016	0.106 ± 0.005	0.070 ± 0.010	0.026 ± 0.004
$hCCM_s$	0.182 ± 0.014	0.106 ± 0.007	0.078 ± 0.006	0.030 ± 0.009
CCM	0.184 ± 0.011	0.107 ± 0.006	0.080 ± 0.004	0.031 ± 0.004

Table C 4. t-value of comparing experimental groups to the control group (membrane N211) for membrane electrode assembly with catalyst layer composed of ionomer SPPB.

RH	N211 vs. $hCCM_d$	N211 vs. $hCCM_s$	N211 vs. CCM
30%	0.19064	0.60555	0.81053
50%	0.11729	0.052673	0.00475
70%	0.91281	0.16004	0.53649
90%	0.9384	0.25277	1.22235

Table C 5. Confidence level of comparing experimental groups to the control group (membrane N211) for membrane electrode assembly with catalyst layer composed of ionomer SPPB.

RH	N211 vs. $hCCM_d$	N211 vs. $hCCM_s$	N211 vs. CCM
30%	N/A	N/A	N/A
50%	N/A	N/A	N/A
70%	80%	N/A	N/A
90%	80%	N/A	85%

Table C 6. Molar water fluxes (mol m^{-2} s^{-1}) through membrane electrode assembly with catalyst layer composed of ionomer Nafion in liquid-vapor permeation at 80 °C

	30% RH	50% RH	70% RH	90% RH
N211	0.183 ± 0.014	0.107 ± 0.015	0.077 ± 0.012	0.029 ± 0.003
$hCCM_d$	0.180 ± 0.009	0.105 ± 0.012	0.075 ± 0.005	0.028 ± 0.006
$hCCM_s$	0.179 ± 0.012	0.106 ± 0.009	0.076 ± 0.007	0.029 ± 0.006
CCM	0.159 ± 0.004	0.095 ± 0.004	0.058 ± 0.001	0.030 ± 0.004

Table C 7. t-value of comparing experimental groups to the control group (membrane N211) for membrane electrode assembly with catalyst layer composed of ionomer Nafion.

RH	N211 vs. $hCCM_d$	N211 vs. $hCCM_s$	N211 vs. CCM
30%	0.5223	1.1103	3.5715
50%	0.3905	0.2246	2.1806
70%	0.6005	0.3667	4.1498
90%	0.2017	0.1995	0.4215

Table C 8. Confidence level of comparing experimental groups to the control group (membrane N211) for membrane electrode assembly with catalyst layer composed of ionomer Nafion

RH	N211 vs. $hCCM_d$	N211 vs. $hCCM_s$	N211 vs. CCM
30%	N/A	85%	99%
50%	N/A	N/A	95%
70%	N/A	N/A	99.9%
90%	N/A	N/A	N/A

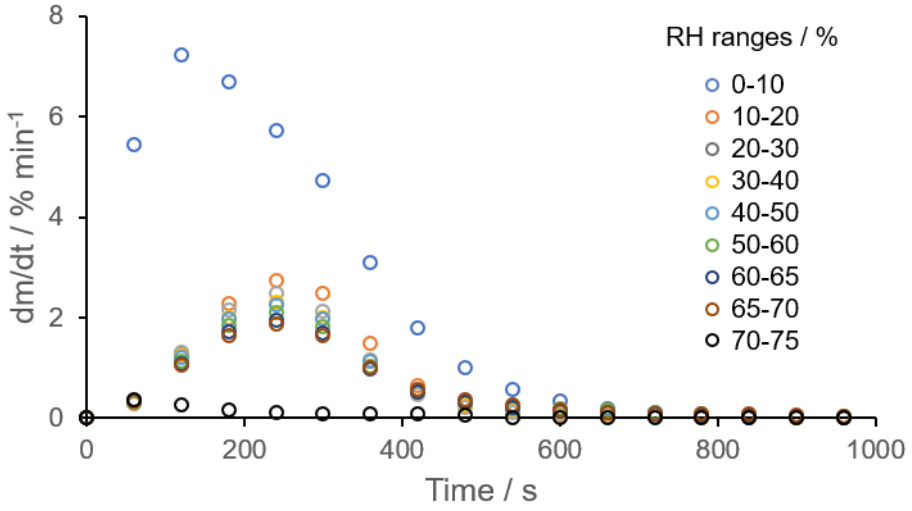

Figure C 1. Instantaneous mass-change rate, dm/dt, over time in each relative humidity intervals of CL SPPB with 10% ionomer content at 80 °C

Table C 9. Effective rate constant of transient diffusion, k_{sorp}, of CL SPPB with different ionomer contents under different RH steps at 80 °C.

RH step [%]	CL SPPB k_{sorp} [s^{-1}] 10%	20%	30%	Membrane N211
0-10	0.53 ± 0.09	0.51 ± 0.07	0.42 ± 0.07	0.51 ± 0.09
10-20	0.38 ± 0.07	0.38 ± 0.06	0.34 ± 0.07	0.39 ± 0.08
20-30	0.15 ± 0.04	0.15 ± 0.04	0.13 ± 0.03	0.18 ± 0.05
30-40	0.076 ± 0.009	0.077 ± 0.008	0.062 ± 0.008	0.082 ± 0.008
40-50	0.037 ± 0.007	0.040 ± 0.006	0.029 ± 0.005	0.038 ± 0.006
50-60	0.024 ± 0.004	0.023 ± 0.005	0.019 ± 0.004	0.024 ± 0.003
60-65	0.012 ± 0.003	0.012 ± 0.003	0.0089 ± 0.0009	0.014 ± 0.003
65-70	0.0062 ± 0.0008	0.0059 ± 0.0009	0.0060 ± 0.0008	0.0082 ± 0.0009
70-75	0.0036 ± 0.0005	0.0036 ± 0.0005	0.0032 ± 0.0005	0.0053 ± 0.0006

Table C 10. Effective rate constant of transient diffusion, k_{sorp}, of CL Nafion with different ionomer contents under different RH steps at 80 °C.

RH step [%]	CL Nafion k_{sorp} [s^{-1}] 10%	20%	30%	Membrane N211
0-10	0.41 ± 0.06	0.40 ± 0.08	0.39 ± 0.07	0.51 ± 0.09
10-20	0.32 ± 0.05	0.33 ± 0.06	0.31 ± 0.09	0.39 ± 0.08
20-30	0.12 ± 0.04	0.11 ± 0.03	0.10 ± 0.03	0.18 ± 0.05
30-40	0.053 ± 0.008	0.056 ± 0.006	0.050 ± 0.007	0.082 ± 0.008
40-50	0.026 ± 0.006	0.031 ± 0.005	0.021 ± 0.004	0.038 ± 0.006
50-60	0.020 ± 0.004	0.020 ± 0.004	0.016 ± 0.005	0.024 ± 0.003
60-65	0.0094 ± 0.0009	0.011 ± 0.005	0.0073 ± 0.0009	0.014 ± 0.003
65-70	0.0042 ± 0.0006	0.0045 ± 0.0007	0.0042 ± 0.0005	0.0082 ± 0.0009
70-75	0.0024 ± 0.0004	0.0024 ± 0.0005	0.0023 ± 0.0004	0.0053 ± 0.0006

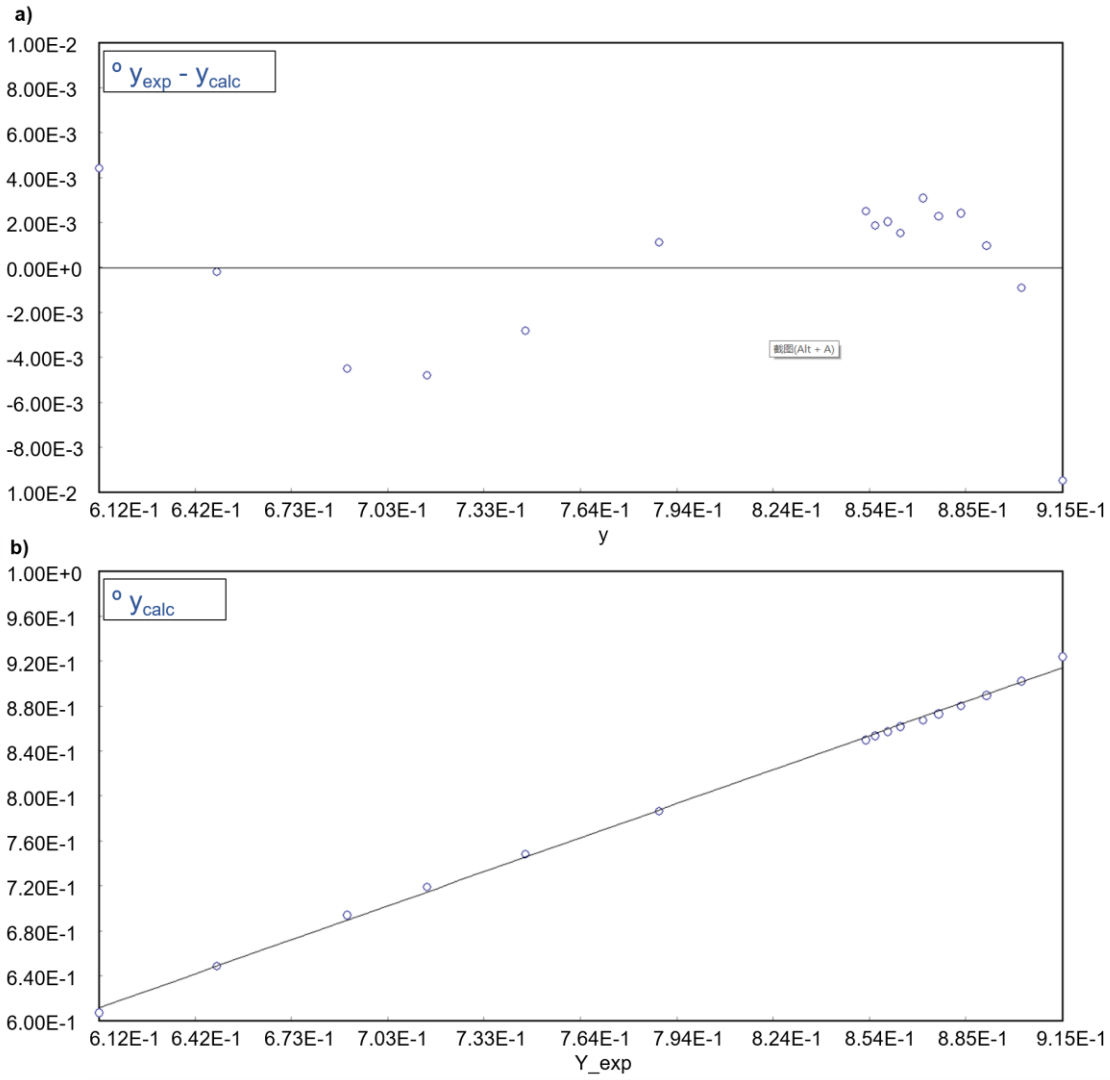

Figure C 2. a) Residual distribution and b) calculation value against experimental value in 0-D equation approximation for CL SPPB with 10 wt.% ionomer content. Heteroscedasticity is observed in residual distribution.

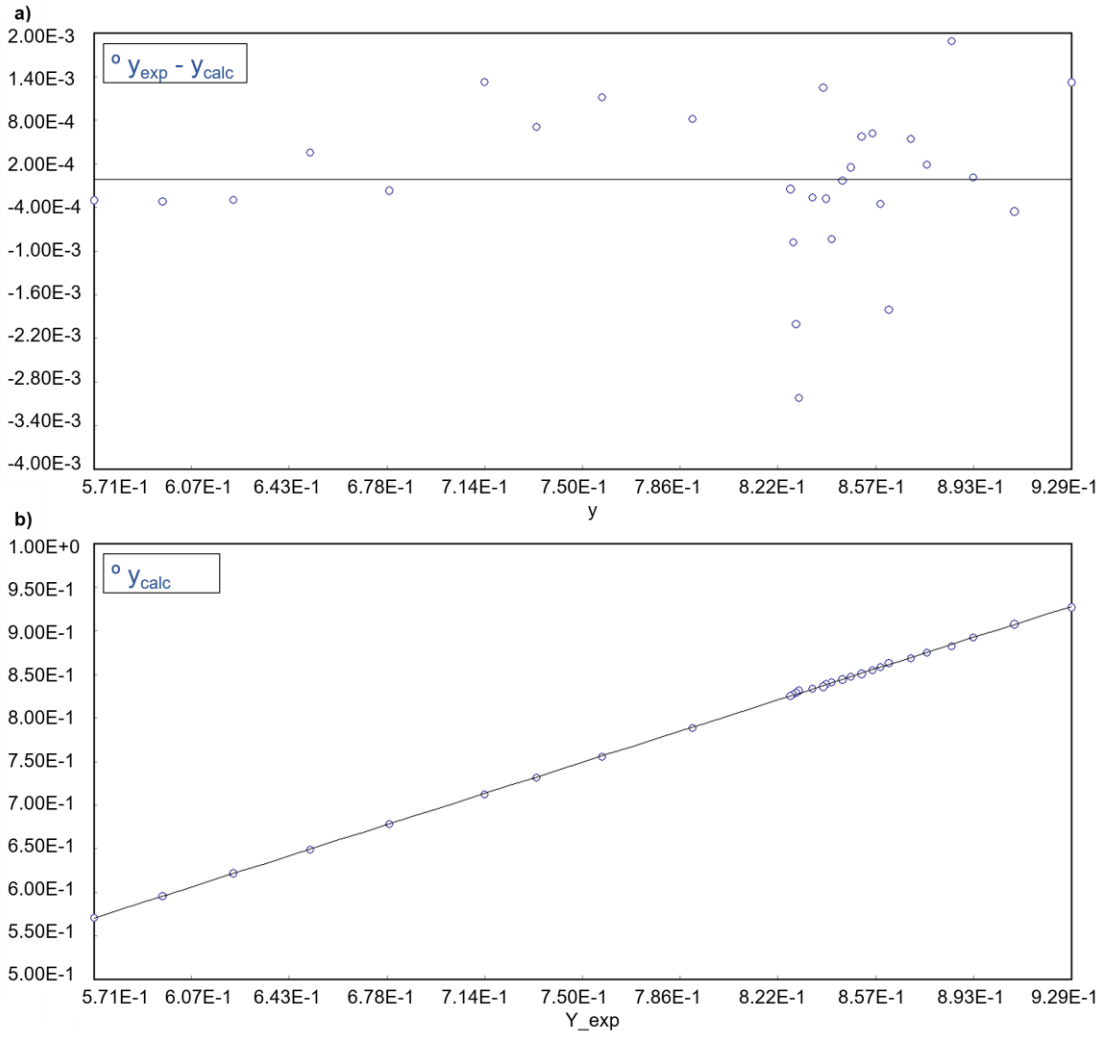

Figure C 3. a) Residual distribution and b) calculation value against experimental value in 0-D equation approximation for CL SPPB with 15 wt.% ionomer content. Heteroscedasticity is observed in residual distribution.

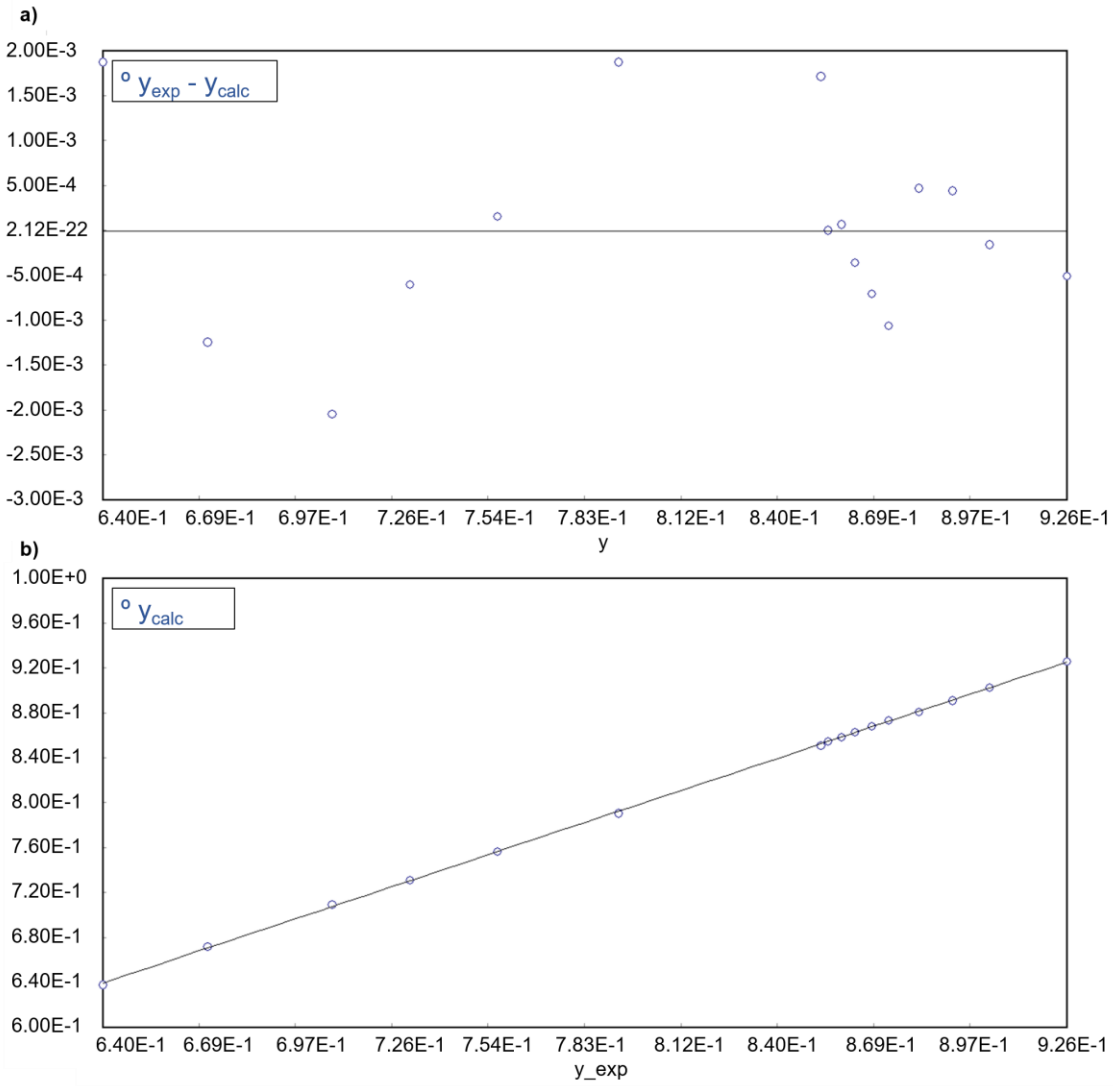

Figure C 4. a) Residual distribution and b) calculation value against experimental value in 0-D equation approximation for CL SPPB with 20 wt.% ionomer content. Heteroscedasticity is observed in residual distribution.

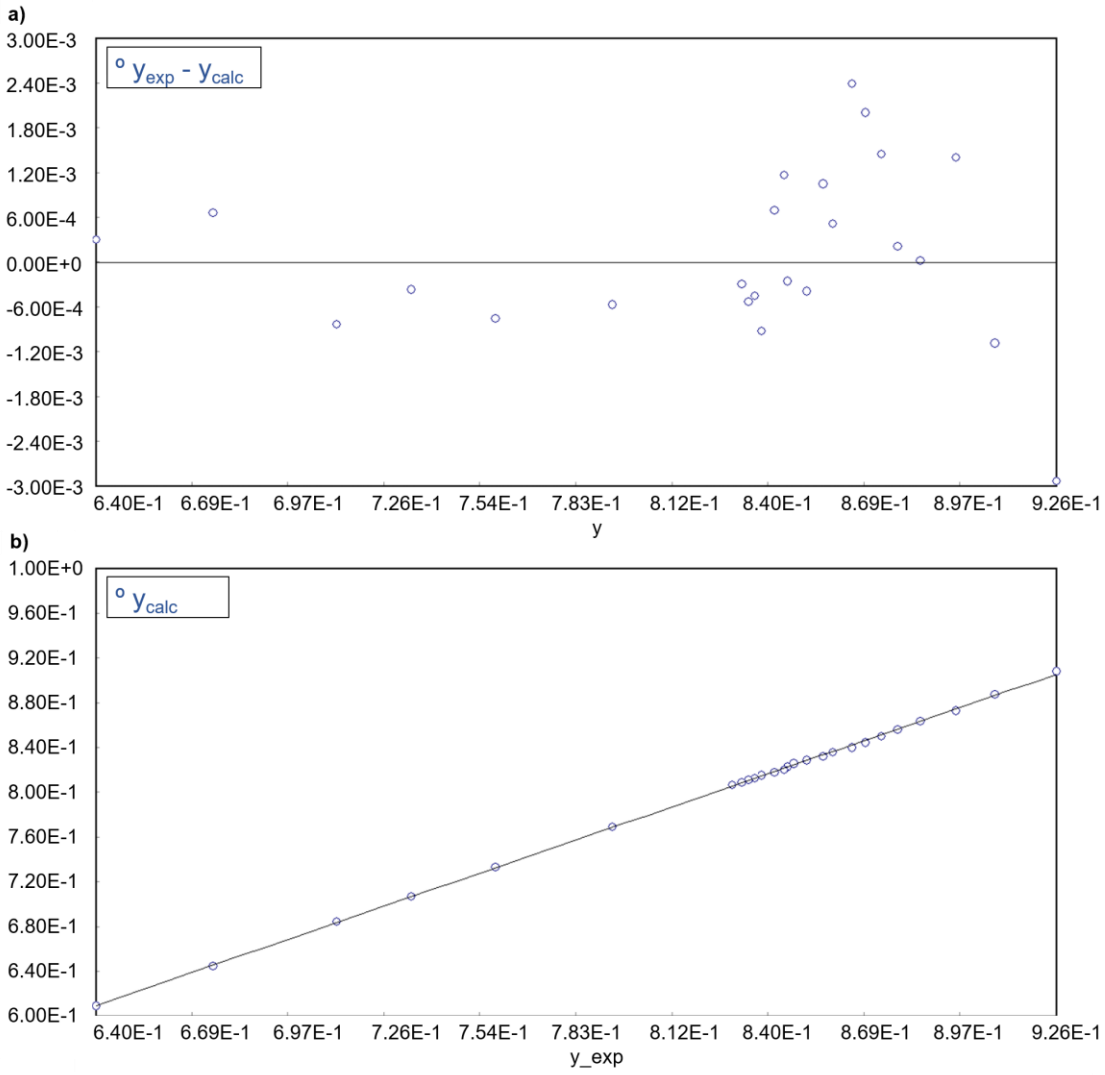

Figure C 5. a) Residual distribution and b) calculation value against experimental value in 0-D equation approximation for CL SPPB with 25 wt.% ionomer content. Heteroscedasticity is observed in residual distribution.

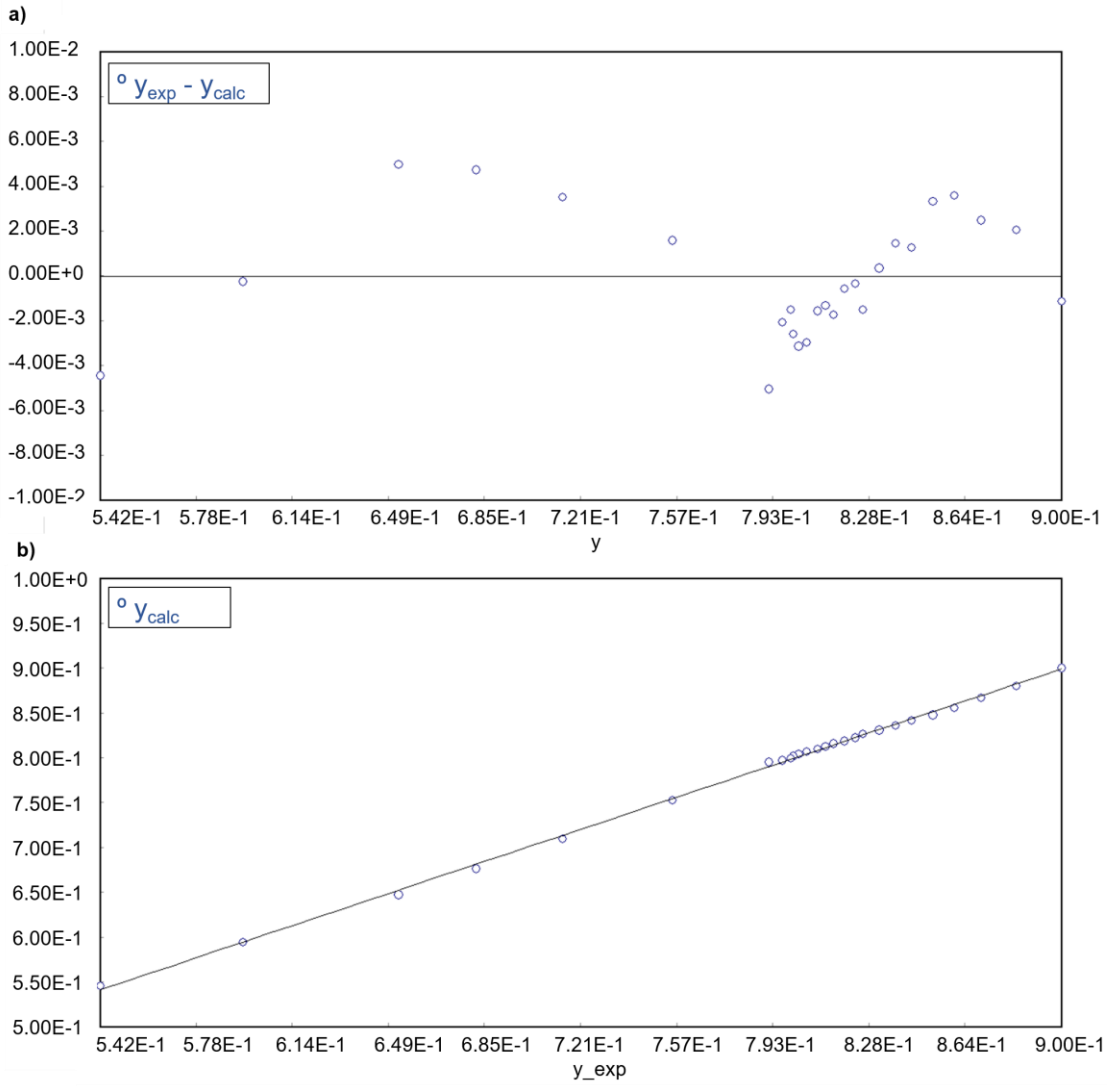

Figure C 6. a) Residual distribution and b) calculation value against experimental value in 0-D equation approximation for CL SPPB with 30 wt.% ionomer content.

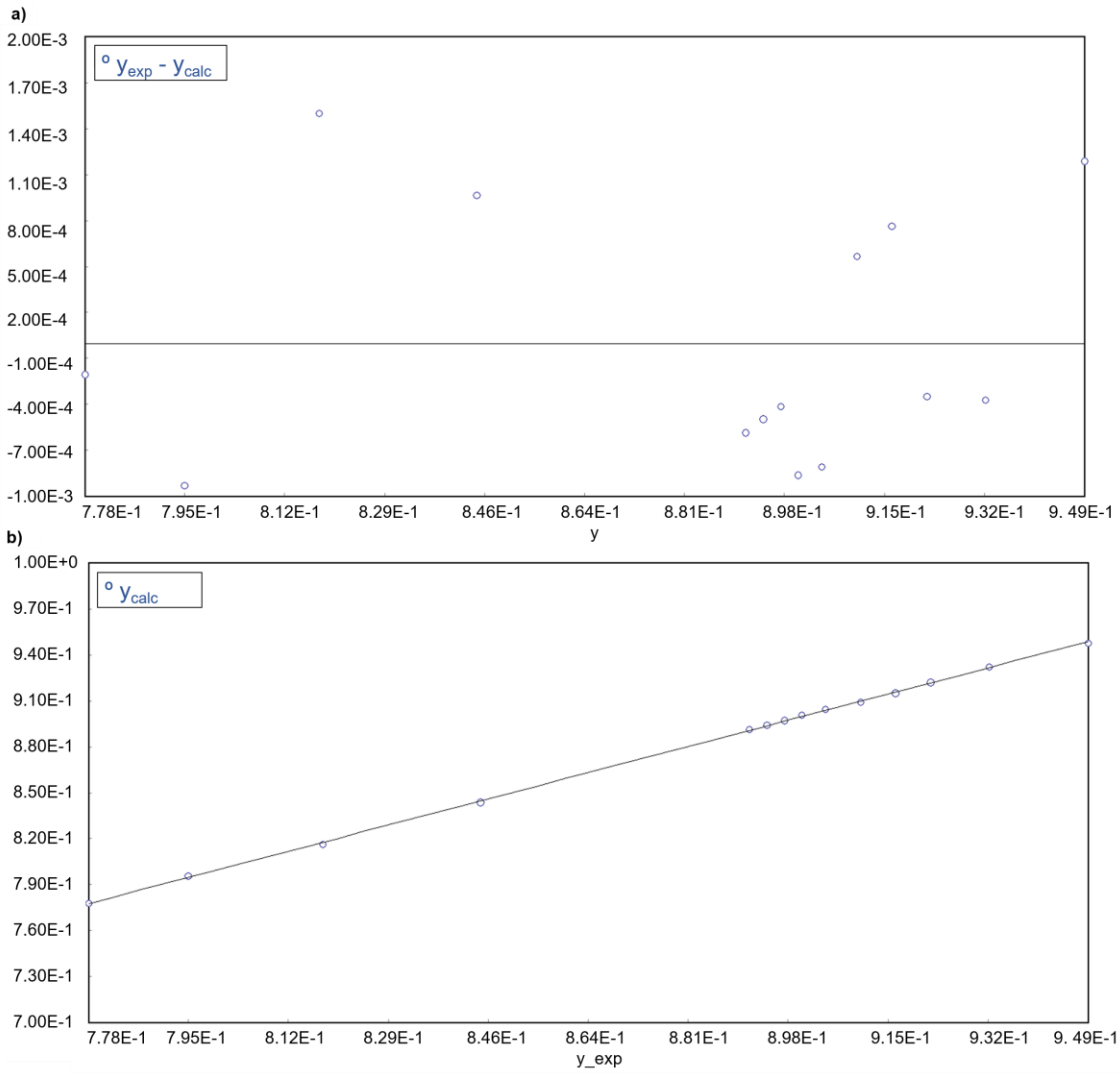

Figure C 7. a) Residual distribution and b) calculation value against experimental value in 0-D equation approximation for CL Nafion with 30 wt.% ionomer content. Heteroscedasticity is observed in residual distribution.